ETH zürich

ETH Library

New Structures and Functionalities in Multiferroic Bismuth Ferrite

First-principles–based studies

Doctoral Thesis

Author(s):
Grosso, Bastien Francesco

Publication date:
2021

Permanent link:
https://doi.org/https://doi.org/10.3929/ethz-b-000513311

Rights / license:
In Copyright - Non-Commercial Use Permitted

This page was generated automatically upon download from the ETH Zurich Research Collection.
For more information, please consult the Terms of use.

DISS. ETH NO. 27709

New Structures and Functionalities in Multiferroic Bismuth Ferrite

First-principles–based studies

A thesis submitted to attain the degree of

DOCTOR OF SCIENCES of ETH ZURICH
(Dr. sc. ETH Zurich)

presented by

Bastien Francesco Grosso

M.Sc. in Physics, École Polytechnique Fédérale de Lausanne (EPFL)

born on 20.04.1987

citizen of Vernier (GE) and Italy

accepted on the recommendation of

Prof. Dr. Nicola Spaldin, examiner
Prof. Dr. Chris Pickard, co-examiner
Prof. Dr. Manfred Fiebig, co-examiner

2021

Bastien Francesco Grosso
New Structures and Functionalities in Multiferroic Bismuth Ferrite
First-principles–based studies
Diss. ETH No. 27709
Zurich, July 2021

To Luisa and Mattia

"All variety of created objects which represent order and life in the universe could happen only by the willful reasoning of its original Creator, whom I call the 'Lord God'."

— Isaac Newton

Acknowledgements

This page is probably the most important of this thesis because without the people that were part of my PhD adventure, this work would not exist.

The first person that I would like to thank is my supervisor Prof. Nicola Spaldin. I remember that the day that I came for the interview for the PhD position, I told to myself that I could not find a better place and if I would not have been hired I am not sure if I would have looked for another position. After more than four years spent in the group and under the supervision of Nicola, I realise how accurate was my feeling. I could not dream of a better supervisor or of a better atmosphere to do research. I am infinitely thankful to Nicola for her exceptional qualities as a scientist, as a group leader, as a mentor and as an amazing role model. Dear Nicola, there are thousands of professional reasons why I feel that it was an honour to be part of your group but overall I would like to thank you for your kind-heartedness and support in every situation that I lived during my PhD.

The Materials Theory group would not be the same without Susanne Blatter that I would like to thank especially for everything that she did for me and everything that she is: Further than taking care of the administrative matters, she takes care of the people in the group.

A large part of this thesis has been a collaboration between theory and experiments. I would like to thank all my collaborators and particularly Prof. Julia Mundy with who I had the pleasure to closely collaborate. I would also like to thank specially Prof. Ramamoorthy Ramesh, Prof. Darrell Schlom, Prof. Pu Yu, Dr. Colin Heikes, Dr. Morgan Trassin and Dr. Johanna Nordlander for the "exciting scientific discoveries" that we made together. I also had the pleasure to collaborate with exceptional theoreticians and would like to thank Prof. Philippe Ghosez, Dr. Marcus Schmitt and Dr. Eric Bousquet for their time and kindness teaching me Multibinit and showing me Liège! I also take the opportunity to thank Prof. Paula Giraldo Gallo and Prof. Camilo Garcia Castro for inviting me to visit them when I was in Colombia. I would also like to thank Prof. Manfred Fiebig, Prof. Chris Pickard and Prof. Jörg Löffler for accepting to be part of my defence and taking the time to read this thesis.

I would like to thank all the present and past members of the Materials Theory group for the help, support, advice, nice time at work and outside of work. A special thanks goes to Alexander Hampel, Madhura Marathe, Aria Mansouri Tehrani, Xanthe Verbeek for sharing the office with me, and Kane Shenton for

preferring not to share office with me! I already miss the special football players: Sophie Beck and Jaime Souto Caseres and will miss all the others. A special thank you to Tara Tosic for almost making me enjoy running. I would like to thank Chiara Gattinoni for her help in the beginning of my PhD and Quintin Meier, Natalya Fedorova, Aria Mansouri Tehrani and Kane Shenton for their precious advice and help toward the end of my PhD. I also thank the present or past members of the group for the nice moments shared together: Boris Sangiorgio, Awadhesh Narayan, Claude Ederer, Andrea Scaramucci, Walter Tarantino, Maximilian Merkel, Alexander Edström, Dominik Juraschek, Ankit Izardar, Tobias Esswein, Florian Thöle, Maryam Taherinejad, Sayantika Bhowal, Alberto Carta, Marek Matas, Andrea Urru and all the others!

I would like to thank specially Jaime, Raquel, Kane, Yasmine and Aria for the precious moments spent together sharing amazing food and priceless friendship in the last years. I also feel grateful to my friends that supported me with their long-standing friendship from near: Kilian, Seb, Maud, Cédric, Chloé, Alexis, Léandre, Jimmy, Emilie, Laura, Amandine, Fabi, Steffi, Jan and Elsa or from far: Joseph, Manal, Sam, Jean, John and Val.

I want to express my gratitude to my familly in Switzerland, in Italy and in Colombia for their love and presence in my life. Finally, I want to thank from the bottom of my heart my wife Luisa for her unconditional love and support, for her encouragements, especially for her patience in the last months and for believing in me more than I do myself. I dedicate this achievement to you Luisa.

Abstract

In this work, we present a comprehensive computational and theoretical study of the structural phase space of multiferroic Bi-Fe-O and the influence of the structure on functional properties.

Complex oxides are known for their many different functionalities, including ferroelectricity, ferromagnetism or piezoelectricity, which are relevant for technological application. Multiferroicity, in which at least two different ferroic orders (ferromagnetism, ferroelectricity and ferroelasticity) coexist and couple in a single phase is of particular interest and can enable, for example, control of magnetic properties using an applied electric field. $BiFeO_3$ (BFO) is one of the most studied multiferroic materials because of the coexistence of magnetic and polar orders at room temperature promising for applications. The substantial intrinsic functionalities of complex oxides can be further enhanced by growing them as thin films in superlattices or heterostructures. In most cases identified to date, this is a result of the change in the material's lattice constants caused by epitaxial strain imposed by the substrate. This change in lattice constants can modify the functionalities, for example causing a phase change to a higher polar state in BFO. In heterostructures of polar and non-polar materials, the polar discontinuity at the interface results in an accumulation of surface charges, which in turn create an electric field, known as the depolarising field. This depolarising field can cause the formation of domains in the polar material and even change the orientation of the polarisation, in order to reduce the energy penalty of the interfacial charge.

We start our study by considering the case in which a phase transition to a non-polar phase with low relative energy is preferred over polar domains formation and present a new phase with larger unit cell size and surprising properties matching recent experimental results. We then explore the phase space of BFO using density functional theory (DFT) calculations and reveal several low-energy phases with large unit cells which could be stabilised by a polar discontinuity at the interface. Finally, we consider a heterostructure in which the polar discontinuity is partially reduced by the presence of differently charged ionic layers and show that this causes an isosymmetric phase transition from two phases with the same symmetry but different polar states in highly-strained BFO.

Next, we study a new candidate multiferroic material, bismuth hexaferrite, which exhibits net magnetic and possible ferroelectric moments at room temperature, experimentally demonstrated. We show that the net magnetic moment is likely related to the presence of Fe vacancies and compute the energy barrier between opposite orientations of the polarisation in order to evaluate the likelihood for it to be ferroelectric. This result paves the way for the exploration of new materials in the Bi-Fe-O compositional phase space with technologically relevant properties.

Finally, we conclude our work by proposing an accelerated method combining DFT, irreducible phonon modes and machine learning to explore the potential energy surface of BFO and we predict several low-energy structures, suggesting that the phase space of BFO is still far from being completely known.

This thesis highlights the richness of the phase space of Bi-Fe-O and the importance of the boundary conditions provided by the heterostructure, in particular the electrostatics at the interface in determining the properties of functional oxides. Finally, the methods that we developed provide a new accelerated approach to structure discovery. They are broadly applicable and can certainly lead to discoveries in other materials.

Résumé

Dans ce travail, nous présentons une étude computationnelle et théorique de l'espace de phase des composantes Bi-Fe-O et de l'influence de la structure sur les propriétés fonctionnelles.

Les oxydes complexes sont connus pour leurs nombreuses fonctionnalités, telles que la ferroélectricité, le ferromagnétisme ou la piézoélectricité, toutes prometteuses pour d'éventuelles applications technologiques. Le multiferroïsme, consistant en la coexistence d'au moins deux ordres ferroïques différents (ferromagnétisme, ferroélectricité et ferroélasticité) et possiblement couplés dans la même phase est particulièrement intéressant et peut permettre, par exemple, le contrôle des propriétés magnétiques par l'application d'un champ électrique. $BiFeO_3$ (BFO) est l'un des matériaux multiferroïques les plus étudiés en raison de la coexistence de l'ordre magnétique et de l'ordre polaire à température ambiante, rendant ce matériau attrayant en terme d'applications. De plus, les fonctionnalités propres des oxydes complexes peuvent être encore accentuées en faisant croître ces derniers sous forme de couches minces dans des superréseaux ou des hétérostructures. Dans la plupart des cas identifiés à ce jour, le changement des constantes de maille du matériau causé par la contrainte épitaxiale imposée par le substrat est responsable de ce changement de propriétés et peut, par exemple, induire un changement de phase vers un autre état polaire de BFO. Dans les hétérostructures composées de matériaux polaires et non polaires, la discontinuité de la polarisation à l'interface entraîne une accumulation de charges en surface, qui à leur tour créent un champ électrique, appelé champ dépolarisant. Ce champ dépolarisant peut induire la formation de domaines polaires dans le matériau et même modifier l'orientation de la polarisation, afin de réduire la pénalité énergétique due aux charges interfaciales.

Nous commençons notre étude en considérant le cas dans lequel une transition de phase vers une phase non polaire se situant à un état raisonnablement plus élevé en énergie est préférée à la formation de domaines polaires. De plus, nous présentons une nouvelle phase possédant une plus grande taille de cellule unitaire et des propriétés surprenantes, venant confirmer de récents résultats expérimentaux. Nous explorons ensuite l'espace des phases de BFO à l'aide de calculs utilisant la théorie de la fonctionnelle de la densité (DFT) et révélons plusieurs phases de basse énergie avec de grandes cellules unitaires qui pourraient être stabilisées par une discontinuité polaire à l'interface. Enfin, nous considérons une hétérostructure dans laquelle la discontinuité polaire est partiellement réduite par la présence de couches ioniques avec une charge différente et montrons que cela induit une transition de phase isosymétrique entre deux phases de même symétrie mais d'états polaires différents, lorsque BFO est soumis à une forte déformation épitaxiale.

Ensuite, nous étudions un nouveau matériau, candidat à être multiferroïque, l'hexaferrite de bismuth, qui est magnétique et possiblement ferroélectrique

à température ambiante, comme démontré expérimentalement. Nous démontrons que le moment magnétique est probablement lié à la présence de défaut (atom de Fe manquants) et calculons la barrière d'énergie pour modifier l'orientation de la polarisation afin d'évaluer la possibilité que ce nouveau matériau soit également ferroélectrique. Ce résultat ouvre la voie vers l'exploration de nouveaux matériaux composés de Bi-Fe-O et présentants des propriétés qui sont technologiquement intéressantes.

Enfin, nous concluons notre travail en proposant une méthode qui accélère l'exploration de la surface d'énergie potentielle de BFO en combinant DFT, modes irréductibles de phonons et machine learning. Cela nous permet de prédire plusieurs structures de basse énergie, et suggère que l'espace des phases de BFO est encore loin d'être complètement connu.

Cette thèse met en évidence la richesse de l'espace des phases des composantes Bi-Fe-O et l'importance des conditions aux limites pourvues par l'hétérostructure, et en particulier l'importance de l'électrostatique à l'interface, dans la détermination des propriétés des oxydes fonctionnels. Enfin, les méthodes que nous avons développées offrent une nouvelle approche accélérée pour la découverte de structures. Ces méthodes sont largement applicables à d'autres matériaux et peuvent certainement conduire à des découvertes au-delà de BFO.

Contents

Acknowledgements v
Abstract vii
Résumé ix

I BACKGROUND AND METHODS 1
1 BACKGROUND AND MOTIVATION 3
1.1 Introduction . . . 3
1.2 Ferromagnetism and magnetic ordering . . . 4
1.3 Ferroelectricity and the perovskite structure . . . 5
1.3.1 Perovskite Oxides . . . 6
1.3.2 Origin of the ferroelectricity . . . 7
1.3.3 Spontaneous polarisation . . . 9
1.4 Magnetoelectric Multiferroics . . . 12
1.4.1 The intrinsic challenge of multiferroics . . . 12
1.4.2 Different types of multiferroics . . . 13
1.5 Bismuth Ferrite: an overview . . . 15
1.5.1 Structure and properties . . . 15
1.5.2 Weak ferromagnetism . . . 16
1.6 Thin-film geometry . . . 16
1.6.1 Strained thin films . . . 16
1.6.2 Polar discontinuity and depolarising field . . . 17
1.7 Goals and structure of this thesis . . . 18
2 THEORETICAL METHODS 21
2.1 The quantum many-body problem . . . 21
2.2 Born-Oppenheimer approximation . . . 22
2.3 Density-Functional Theory . . . 23
2.3.1 On the density using functionals: Hohenberg-Kohn theorems . . . 23
2.3.2 From many-body to non-interacting: Kohn-Sham equations 24
2.4 Exchange-correlation functionals . . . 26
2.4.1 Local density approximation (LDA) . . . 26
2.4.2 Generalised-Gradient approximation (GGA) . . . 27
2.5 Correction to LDA and GGA: DFT+U . . . 27
2.6 How to solve in the Kohn-Sham equations in practice . . . 28
2.6.1 Plane-wave basis . . . 28
2.6.2 Core electrons and Pseudopotentials . . . 29

II RESULTS I: PHASES, STRAIN AND ELECTROSTATICS 31
3 ELECTROSTATIC ENGINEERING 33
3.1 Experimental evidence . . . 33
3.1.1 Previous results on BFO/LFO superlattices and Lanthanum-doped BFO . . . 34

3.1.2 New BFO structures: STEM images . . . 35
3.2 Computational details . . . 36
3.3 Identifying the distortions . . . 37
3.3.1 Phonon instabilities . . . 37
3.3.2 A new Pnma phase with larger unit cell . . . 38
3.4 How can Pnma(1) be stable experimentally? . . . 42
3.4.1 Epitaxial strain . . . 42
3.4.2 Polar discontinuity and electrostatic model . . . 43
3.5 Thickness, strain and dielectric constant . . . 46
3.6 Anti-polar or antiferroelectric? . . . 48
3.7 Magnetic ordering of Pnma(1) . . . 51
3.8 Conclusion . . . 52
4 EXPLORING THE PHASE SPACE WITH PHONONS 55
4.1 Review of previously identified phases . . . 56
4.2 Peer reviewed work . . . 56
4.3 Other previously unreported phases . . . 68
4.3.1 Starting again with Pbam . . . 68
4.3.2 Another Pc series . . . 69
4.3.3 Highly-strained polymorphs . . . 71
4.4 Conclusion . . . 73
5 ELECTROSTATICS AND ISOSYMMETRIC PHASE TRANSITION 75
5.1 BFO under compressive strain . . . 76
5.2 Experimental motivation . . . 76
5.3 Rotational and polar modes . . . 77
5.4 Electrostatics at the interface with II-IV perovskite . . . 78
5.5 Reduction of the c/a ratio and isosymmetric phase transition . . . 80
5.6 Switching path . . . 81
5.7 Conclusions . . . 83

III RESULTS II: Bi,Fe AND O - BEYOND THE 1-1-3 CHEMISTRY 85
6 BISMUTH HEXAFERRITE 87
6.1 Experimental findings . . . 88
6.2 Computational details . . . 89
6.3 Structures and Magnetic orders . . . 91
6.4 Polarisation and Switching energy barrier . . . 92
6.5 Conclusion . . . 94

IV RESULTS III: BEYOND DFT 97
7 REVISITING THE PHASE SPACE WITH MACHINE LEARNING 99
7.1 Computational details . . . 100
7.2 Distortion modes as building blocks . . . 100
7.3 Description of the procedure . . . 103
7.3.1 First round: Machine learning model . . . 105
7.3.2 Second round: Low energy phases . . . 107
7.4 Conclusion and perspective . . . 109

V CONCLUSION 111
8 SUMMARY AND OUTLOOK 113

BIBLIOGRAPHY 121

Part I

BACKGROUND AND METHODS

In the first part we introduce the subject of this thesis and present the theoretical tools that are used.

In chapter 1, we first review basic concepts related to ferromagnetism, ferroelectricity and typical perovskite structure, before introducing the multiferroic materials and the material that is the core of this thesis, bismuth ferrite. We finish the chapter by introducing a few elements of the physics related to thin films and giving a description of the structure of this thesis.

In chapter 2, we introduce the quantum many-body problem and the difficulties in its solution and continue by presenting a possible way to solve the many-body Schrödinger equation numerically using density functional theory.

Background and Motivation

1

1.1 INTRODUCTION

Modern technology strongly relies on magnetic and electronic materials. For instance, information can be stored as regions of opposite magnetic moment in ferromagnets (materials with a spontaneous magnetisation reversible by applying a magnetic field). A related class of materials, namely ferroelectrics (materials with a spontaneous polarisation reversible by applying an electric field), has been used for decades in sensors and actuators exploiting the sensitivity of the polarisation to external conditions such as temperature, electric field or mechanical deformation. Nevertheless, the ever increasing usage of information and communications technology requires dimensionally reduced and energetically more efficient devices. Multifunctional materials, such as multiferroics, that can combine magnetic and electronic orders at the same time, represent a promising route for future technology.

Originally, the term "multiferroics" designated materials in which two or three of the properties ferroelectricity, ferromagnetism or ferroelasticity (spontaneous deformation switchable by an applied stress) coexist in the same phase [1]. Nowadays, this term is used more broadly to include any type of magnetic arrangement (ferro-, antiferro-, and ferri-magnetic) and is often used to refer to materials with magnetic and electronic order (magnetoelectric multiferroic). The presence of the two order parameters (polarisation and magnetisation) could in principle increase the storage density to four states per bit, corresponding to the different combinations of up and down polarisation and magnetisation, if they are not coupled. On the other hand, if polarisation and magnetisation are coupled, one could switch the magnetisation by applying an electric field resulting in a low energy consuming memory device. Nevertheless, the development of multiferroic materials remains challenging due to the incompatible nature of ferromagnetism and ferroelectricity.

Complex oxides with the perovskite (or related) structure have been used successfully to combine ferroelectricity and ferromagnetism in the same structure. This accomplishment is mainly due to the large flexibility of those structures: about 80% of the elements in the periodic table can be stabilised with this structure type, enabling the synthesis of thousands of materials with targeted functionalities. Moreover, the perovskite structure is convenient for heterostructuring different materials, which can modify their intrinsic properties due for example to size confinement, interface effects or constraint in the lattice parameters. The possibility of designing new materials with desired properties was further enabled in the past years by experimental progress in growth tech-

niques permitting sharp interfaces between different materials, as well as by theoretical developments and increase of simulation power.

Among the know multiferroic materials to date, bismuth ferrite ($BiFeO_3$) is certainly the most studied one. At room temperature, bulk $BiFeO_3$ (BFO) is ferroelectric (with a large polarisation) and antiferromagnetic (with a small ferromagnetic canting), ranking it among the most promising materials for possible devices. Nevertheless, after years of investigations, there are still new aspects of this material to be discovered as will be presented in this thesis.

The aims of this chapter are to provide a description of the important background concepts, and to spell out the goals of this thesis. We will review a few basic concepts about ferromagnetism in section 1.2 in order to introduce in section 1.3 the concept of ferroelectricity and the typical perovskite structure, central for this thesis. We will then see how and under which conditions these two orders can coexist in multiferroic materials (section 1.4) and introduce in section 1.5 the material that is at the core of this thesis, $BiFeO_3$. Finally, we will conclude this chapter by giving an overview of the different aspects studied in this work.

1.2 FERROMAGNETISM AND MAGNETIC ORDERING

Magnetisation in a material is caused by the alignment of the magnetic dipole moments of the different atoms. If the dipoles are randomly distributed (Fig. 1a), the net magnetisation of the system is null. On the other hand, if all the dipoles are aligned in the same direction (Fig. 1b) there is a non-zero net magnetisation in the system.

A ferromagnet is a material with multiple degenerate orientations of the magnetisation, that often experiences a phase transition at low temperature, toward a magnetically ordered system with a spontaneous magnetisation, even in the absence of an external magnetic field. The transition temperature is called Curie temperature (T_C) and the origin of ferromagnetism is related to the exchange interaction that favours parallel spins between nearest neighbours, below T_C. Above T_C, the thermal energy becomes more important than the exchange interaction, resulting in a random arrangement of the magnetic moments.

The characteristic hysteresis loop of a ferromagnetic material is displayed in Fig. 1c. Initially, a ferromagnetic system can lack a net magnetisation due to the formation of domains of opposite orientations. The application of an external magnetic field orients the different domains in the same direction and induces a net magnetisation in the system that increases with the field until it reaches a saturation value (M_s). When the external field is removed, a remanent magnetisation persists (M_r) and by reversing the direction of the external field, one can reduce the net magnetic moment of the system until it switches at a critical value, called the coercive field (H_c). The value of the coercive field is important for possible applications: if the value is small, the magnet can be easily (fast) switched, interesting for transformer cores for example; if the value

is large, the two magnetic states are stable and the material can be a permanent magnet [2].

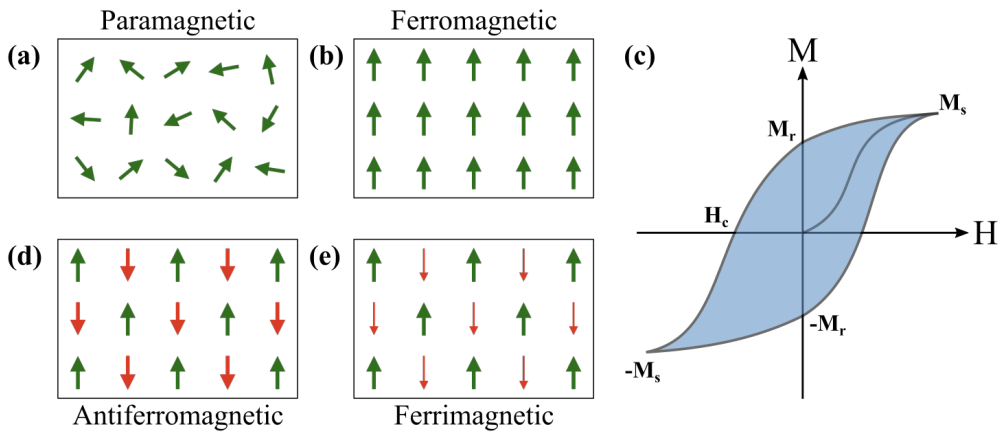

Figure 1: Magnetic arrangements and magnetic hysteresis loop. (a) Disordered magnetic configuration with no net magnetisation. (b) Ferromagnetic configuration with all spins pointing toward the same direction. (c) Hysteresis loop of a ferromagnetic material with M_s, M_r and H_c, respectively the saturation of the magnetisation, remanent magnetisation and coercive magnetic field. (d). Antiferromagnetic ordering with spins of opposite direction but same size. (e) Ferrimagnetic configuration formed of spins with opposite direction and different magnitudes.

Other magnetic configurations such as antiferromagnetic (AFM), ferrimagnetic (FiM) or weak ferromagnetic (wFM), can also exist in materials. As they will become relevant for the work presented in this thesis, we will briefly mention them. Antiferromagnetic order (AFM) consists of an antiparallel arrangement of neighbouring spins (Fig. 1d), resulting in a zero net magnetisation. If the strength of the dipoles in both sub-lattices is different, the system is called ferrimagnetic (Fig. 1e) and can display net magnetisation (usually smaller than in a FM system). Finally, an AFM system can display net magnetisation if the spins are perfectly antiparallel but slightly canted, which is called weak ferromagnetism.

1.3 FERROELECTRICITY AND THE PEROVSKITE STRUCTURE

There exists an electrical property, analogous to ferromagnetism called *ferroelectricity*. An insulating material is called ferroelectric (FE) if it possesses two or more stable (metastable) states with non-zero electric polarisation value under zero electric field (called spontaneous polarisation) and if the different states (different orientations of the polarisation) are reachable by the application of

an electric field. The energy to reach the different states is given by the energy barrier between them and the energy can be lowered by applying an electric field parallel to the polarisiation. The coupling between the polarisation and the electric field is given by the term $-\mathbf{E}\cdot\mathbf{P}$, where $\mathbf{E}$ is the external electric field applied and $\mathbf{P}$ the polarisation of the system. The behaviour of the ferroelectric material under the application and removal of an electric field is similar to that of a ferromagnet and presents a similar hysteresis loop as that presented in Fig. 1c (with $\mathbf{P}$ instead of $\mathbf{M}$ and with $\mathbf{E}$ instead of $\mathbf{H}$).

Originally, ferroelectricity was first reported in Rochelle salt [3] but the discorvery of ferroelectricity in the much simpler perovskite oxide structure of $BaTiO_3$ accelerated the physical understanding of this phenomenon [4]. While other ferroelectric materials exist (e.g. boracites [5] or tungsten bronzes [6]), the most studied and used ferroelectrics are the complex oxides with perovskite structure.

We will introduce in this section, first, the perovskite structure adopted by many complex oxides. Secondly, we will present the possible origins of ferroelectricity in a material and conclude by discussing the intrinsic property linked to ferroelectricity, that is the electric polarisation, in the context of the so called modern theory of polarisation.

1.3.1 PEROVSKITE OXIDES

The perovskite oxides are materials of composition ABO_3[1], where A is usually a rare-earth metallic element, B a $3d, 4d$ or $5d$ transition metal element and O the oxygen element. The ideal perovskite structure is a cubic unit cell with space group $Pm\bar{3}m$ and 5 atoms per unit cell, with the larger cations (A) at each corner of the cube and the smaller cation (B) at the center of the cube, surrounded by an octahedron of oxygens (O) (see Fig. 2a for an example).

The stability of the perovskite structure depends on the radial size of the different A, B and O atoms. Indeed, the perovskite structure depends on the size of the octahedra surrounding the B atom, while the A atom must occupy the space between the octahedra [4]. This criterion is captured by the Goldschmidt tolerance factor t [7], defined as:

$$t = \frac{r_A + r_O}{\sqrt{2}(r_B + r_O)} \quad , \tag{1.1}$$

where r_A, r_B and r_O are the radii of the different ions, respectively A, B and O. If the ratio is close to one, the structure adopted is the ideal perovskite structure with a cubic lattice (Fig. 2a). On the other hand, if A is too large or B too small, $t > 1$ and the structure will stabilise a polar distortion (e.g. $BaTiO_3$). In contrast, if A is too small or B too large, $t < 1$, then the atom A is underbonded with its 12 first-neighbours oxygen atoms, resulting in a rhombohedral or orthorhombic structure. If t differs too much from unity, the perovskite-like structure is not favourable.

[1]Note that to be exact, perovskite oxides can also have other compositions such as WO_3 or ReO_3.

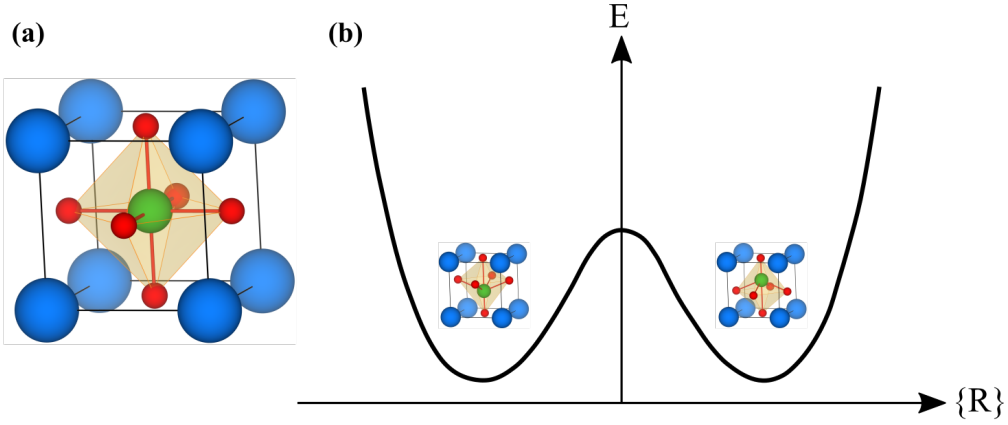

Figure 2: Ideal perovskite structure and ferroelectric double well. (a) The larger A cation (blue) is at the corner of the cubic unit cell. The smaller B cation (green) is at the center of an octahedron (orange) formed by the oxygen anions (red). Note that the O anions are shown as small circle for clarity. (b) The energy as a function of the relative vertical displacement of the B and O atoms gives rise to a double well with on the right (vertical displacement toward up of the B cation) a minimum with polarisation pointing up, and on the left (vertical displacement toward down of the B cation) another equivalent minimum with polarisation pointing down.

1.3.2 ORIGIN OF THE FERROELECTRICITY

In the case of FE perovskite oxides, the ideal perovskite can in principle be the stable paraelectric phase at high-temperature. Below Curie temperature, the symmetry of the system is lowered by structural distortions accompanied by an off-centering of the A or B atom with respect to the oxygen anions, which creates electric dipole moments in the system, responsible for the spontaneous polarisation. The direction of the off-centering can be inverted by applying an electric field of opposite direction, giving rise to the characteristic double well for a ferroelectric material with two equivalent minima corresponding to the opposite directions in the unit cell, and opposite orientation of the polarisation (Fig. 2b). Note that in principle the double well could be asymmetric.

The off-centering would be energetically unfavorable if the chemical bonding between atoms were perfectly ionic, and materials would not have a spontaneous polarisation. In practice, the equilibrium structure is determined by the balance between the short-range repulsion between the different clouds of electrons, favouring a centrosymmetric structure, and the long-range Coulomb forces promoting a ferroelectric (non centrosymmetric, distorted) state [8]. A distortion is accompanied by changes in chemical bonding and the breaking of symmetry from centrosymmetric to non-centrosymmetric is due to the so called Second Order Jahn-Teller effect (SOJT).

The chemistry that determines whether some materials are ferroelectric and others not, is described by the SOJT. We take a perturbative approach to express the energy of the electronic ground state as a function of the distortion Q [9], where Q in our case represents the polar displacement (e.g. off-centering of the B atom). We then write the Hamiltonian of the electronic ground state as a Taylor expansion:

$$H = H^{(0)} + \delta H \cdot Q + \delta^2 H \cdot Q^2 + ... \tag{1.2}$$

where $\delta^n H = \left.\frac{d^n H}{dQ^n}\right|_{Q=0}$ and the first term corresponds to the energy of the unperturbed system. We then express the energy of the perturbed system as:

$$\begin{aligned} E(Q) = E(0) &+ \langle 0| \delta H |0\rangle Q \\ &+ \frac{1}{2}\left(\langle 0| \delta^2 H |0\rangle - 2\sum_n \frac{|\langle 0| \delta H |n\rangle Q|^2}{E_n - E(0)} \right) \\ &+ ... \end{aligned} \tag{1.3}$$

The first term in the first line corresponds to the energy of the undistorted structure and the second term to the first order correction to the energy (possibly related to the first-order Jahn-Teller distortion, characteristic of the tetragonal distortion in a d^1 and d^4 perovskite for example). The state $|0\rangle$ corresponds to a centrosymmetric structure (even) and as the Hamiltonian is even, its derivative (δH) is odd. Thus, the integral of their product is zero. In the second line, the first term is positive and involves no redistribution of the electrons and consequently disfavours FE distortions. As the second term of the second line is negative (due to the minus sign in front of the sum), it lowers the energy and then favours FE distortions. Note that this time there is a redistribution of the electrons as the bra and the ket represent different states and this term represents a mixing of the ground state with the excited state through the formation of new bonds [2].

The stability of a ferroelectric distortion results then from the balance between the mixing energy provided by the negative term and the repulsion energy from the positive term. In order for the negative term to be large, two criteria should be respected. First, the term $\langle 0| \delta H |n\rangle$ should be non-zero, which is true if the last excited state $|n\rangle$ and the ground state $|0\rangle$ have opposite parity. Second, the difference of energy between the ground state and the excited state should be small. Therefore there should exist a low-lying excited state available.

The first criterion results in two different types of FE materials.

1. Ferroelectricity emerges from the B site: The Ligand-field stabilises the off-centering of the B-site transition metal cation with its surrounding oxygen with p-character. This happens for example at the Ti site (d^0) in $BaTiO_3$ that moves towards the oxygen [10] – the state at the bottom of the conduction band has even parity.

2. Ferroelectricity emerges from the A site: The ns^2 lone pairs of electrons mix with cations and anions with p-character and lose their center of symmetry. This happens for example at the Bi site in $BiFeO_3$ [11].

The above description is only local and does not take into account other geometric factors such as the rotations of the oxygen octahedra. Such rotations, often called "Glazer tilts"[2] [12] (Fig. 3a-b), might force the local polarisation to arrange in an antipolar manner, where neighbouring polar distortions have the opposite direction, resulting in no net polarisation (Fig. 3c).

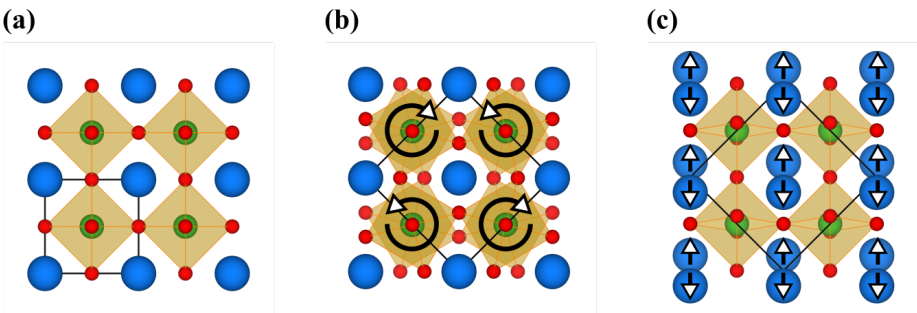

Figure 3: Possible distortions of the perovskite. (a) Ideal perovskite supercell. The octahedra are not rotated, corresponding to $a^0a^0a^0$ in Glazer notation. (b) Antiphase rotation of the octahedra. Along the direction perpendicular to the figure, the consecutive octahedra are rotated in the opposite direction, corresponding to $a^-a^-a^-$ if we assume that the rotations are identical along each of the three cartesian directions. (c) Antipolar displacements of the A site (blue atoms). In all cases, the unit cell is indicated by a black square. The unit cell in (a) is the cubic unit cell similar to Fig. 2a, whereas the lattice vectors of the unit cells in (b) and (c) correspond to the diagonals of the cubic unit cell. If the lattice vector in (a) has a length of a_0, the lattice vectors in (b) and (c) have length $\sqrt{2}a_0$. The distortions with respect to the cubic (a) case are represented by arrows in (b) and (c).

1.3.3 SPONTANEOUS POLARISATION

We presented so far the typical structure for a ferroelectric material and explained the origin of ferroelectricity in those systems. In this section, we will discuss the fundamental aspects linked to the spontaneous polarisation and present the basics of the theory developed to calculate its value in periodic solids.

[2] Glazer introduced a convenient notation for describing octahedra tilting in perovksites, which consists in using a letter (a, b or c) to indicate the amplitude of tilting along each cartesian direction and a superscript $+$, $-$ or 0 to indicate whether consecutive tiltings are equal, opposite or zero about the respective axis [12].

MODERN THEORY OF POLARISATION

The first definition of the polarisation in a solid was given by Clausius and Mossotti [13, 14]. Assuming point charges, the polarisation can be defined as the sum of individual dipole moments per unit of volume or volume of the unit cell in a crystal:

$$\mathbf{p} = \frac{1}{\Omega}\sum_i q_i \mathbf{r}_i \tag{1.4}$$

where Ω is the volume of the system, q_i the electric charge of the i-th atom and $\mathbf{r}_i$ its position. This definition cannot be applied to real periodic materials for two reasons. First, the electric charges are not discrete but continuous due to the different types of bonding. Second, even a continuous version of equation (1.4) would not be satisfactory, as the value depends on the choice of unit cell in a periodic solid. Indeed a change of choice of unit cell can change the value of $\mathbf{p}$ and a non-polar material, with compensated dipoles, can appear "polar" depending on the choice of unit cell. This apparent problem is reconciled by the multi-valuedness of bulk polarisation [2].

This collection of values form a lattice spaced by the lattice constants of the unit cell divided by its volume. In units of the electron charge we have the lattice given by the quantum of polarisation in the direction i:

$$p_{q,i} = \frac{eR_i}{\Omega} \quad , \tag{1.5}$$

where R_i is the norm of the i-th lattice vector and e the fundamental charge of the electron. This quantity is also called the quantum of polarisation.

While the macroscopic polarisation of a crystal is multi-valued, the change in polarisation is a single-valued quantity that does not depend on the choice of unit cell. This fact is at the origin of the experimental measurement of the polarisation through the so called Sawyer-Toyer setup, where a reference capacitor is used to measure the change of surface charges in the ferroelectric material under applied voltage. Resta [15, 16] , King-Smith and Vanderbilt [17] developed what is called today the *Modern Theory of Polarisation*. We will present here a more intuitive approach to the Modern Theory of Polarisation, following [18]. Let us first define properly the polarisation in a crystal before giving the correct formulation for the spontaneous polarisation.

In a real material, the polarisation originates from the movement of the ions and the distortions of the orbitals around them. While the first contribution is easily defined, we need to introduce the concept of Wannier functions for the second one in order to account for the contribution coming from the electrons. We can define a Wannier function, $w_n(\mathbf{r})$ in the unit cell $\mathbf{R}$ associated with band n as:

$$
\begin{aligned}
w_n(\mathbf{r}-\mathbf{R}) &= \frac{\Omega}{(2\pi)^3}\int_{BZ} d^3\mathbf{k}e^{-i\mathbf{k}\cdot\mathbf{R}}\Psi_{n\mathbf{k}}(\mathbf{r}) \\
&= \frac{\Omega}{(2\pi)^3}\int_{BZ} d^3\mathbf{k}e^{-i\mathbf{k}\cdot(\mathbf{r}-\mathbf{R})}u_n(\mathbf{r}) \quad ,
\end{aligned} \tag{1.6}
$$

where the integral is taken over the Brillouin zone with $\Psi_{n\mathbf{k}}(\mathbf{r}) = e^{i\mathbf{k}\cdot\mathbf{r}}u_n(\mathbf{r})$ according to Bloch theorem, with $u_n(\mathbf{r})$ the cell-periodic functions.

Since Wannier functions (WFs) are localized, we can define the average position of the electrons in the WFs (Wannier center). The Wannier center associated with band n is defined as the expectation value of the position operator $\mathbf{r}$ for the WF $w_n(\mathbf{r})$:

$$
\begin{aligned}
\bar{r}_n(\mathbf{r}) &= \int d^3 w_n^*(\mathbf{r})\mathbf{r}w_n(\mathbf{r}) \\
&= \frac{i\Omega}{(2\pi)^3}\int_{BZ} d^3\mathbf{k}e^{-i\mathbf{k}\cdot\mathbf{R}}\left\langle u_{n\mathbf{k}}\middle|\frac{\partial u_{n\mathbf{k}}}{\partial\mathbf{k}}\right\rangle \quad .
\end{aligned} \tag{1.7}
$$

With this definition of the Wannier centers, we can now define the total polarisation as the sum of the contributions of the ions i and the sum of contributions of the electronic charges centered at the Wannier centers of all occupied Wannier functions n:

$$
\mathbf{p} = \frac{1}{\Omega}\left(\sum_i (q_i\mathbf{r}_i)^{\text{ions}} + \sum_n^{\text{occ}} (q_n\bar{\mathbf{r}}_n)^{\text{WFs}}\right) \quad , \tag{1.8}
$$

where the first term takes into account the dipole moments of the ions and the second term defines the contributions from the electrons through the Wannier center of each occupied valence band.

We can now define the spontaneous polarisation as the difference in polarisation between a polar structure and a centrosymmetric (non-polar) structure along an insulating path:

$$
\begin{aligned}
\mathbf{P}_s =& \mathbf{p}^f - \mathbf{p}^0 \\
=& \frac{1}{\Omega}\sum_i \left(q_i^f\mathbf{r}_i^f - q_i^0\mathbf{r}_i^0\right) \\
&- \frac{2ie}{(2\pi)^3}\sum_n^{\text{occ}}\left(\int_{BZ} d^3\mathbf{k}e^{-i\mathbf{k}\cdot\mathbf{r}}\left\langle u_{n\mathbf{k}}^f\middle|\frac{\partial u_{n\mathbf{k}}^f}{\partial\mathbf{k}}\right\rangle - \left\langle u_{n\mathbf{k}}^0\middle|\frac{\partial u_{n\mathbf{k}}^0}{\partial\mathbf{k}}\right\rangle\right) \quad ,
\end{aligned} \tag{1.9}
$$

where f and 0 indicate the final (polar) and initial (centrosymmetric) positions/wavefunctions respectively.

Note that the integrals contain the Berry phase [19] developed by the wavefunction $u_{n\mathbf{k}}$ along the path $\mathbf{k}$. It results from equation (1.9) that the spontaneous polarisation is always single-valued in that form modulo the quantum of polarisation.

BORN EFFECTIVE CHARGES

We saw above that one can not simply multiply the displacement of the ions by their formal charges to calculate the polarisation, as it does not take into account the chemistry of the system. It is especially incorrect in cases where the Wannier centers move differently than the ions. This situation can result in a larger amount of charges contributing to the polarisation during the displacement (effective charges) than the formal charges.

This difference can be formally defined through the concept of Born effective charges which are defined as the change in polarisation along a direction α when the ion is displaced in the direction β. The Born effective charge Z^* can then be defined for each ion as a second order tensor represented by a 3×3 matrix. Formally, it can be written for a given ion as:

$$Z^*_{\alpha\beta} = \frac{\Omega}{e}\frac{\delta P_\alpha}{\delta d_\beta} \quad , \tag{1.10}$$

where Ω is the volume of the unit cell, e the elementary charge of the electron and P_α and d_β the components of the polarisation and displacement respectively along the direction α and β.

Alternatively, one can define the Born effective charge as the variation of force F in the direction α induced by an applied electric field E in the direction β:

$$Z^*_{\alpha\beta} = -e\frac{\delta F_\alpha}{\delta E_\beta} \tag{1.11}$$

For ferroelectric materials, or materials close to a ferroelectric phase transition, the Born effective charges are usually larger than the formal charges. It results that multiplying Born effective charges by the displacement is a good approximation to the associated polarisation.

1.4 MAGNETOELECTRIC MULTIFERROICS

Now that we formally introduced the origin and fundamental aspects of ferroelectricity and ferromagnetism, let us discuss how they can coexist in a special class of materials.

1.4.1 THE INTRINSIC CHALLENGE OF MULTIFERROICS

As already presented in the introduction, magnetoelectric multiferroics are materials that are simultaneously ferromagnetic and ferroelectric. In what follows, we will expand this definition to non-primary order parameters such as antiferromagnetism or ferrimagnetism and simply use the term multiferroic.

While a few materials such as nickel iodine boracite [20] were known since the 1950s to possess both ferromagnetism and ferroelectricity, their complex structure did not allow a fundamental understanding of the coexistence of both

orders. In 2000, in a seminal work, Hill (Spaldin) looked at different FE and magnetic perovskite structures, previously identified [21], to provide a list of requirements for a material to be multiferroic [2] and presented reasons why it is so rare to find both properties simultaneously, with different arguments such as symmetry, electrical properties and chemistry. Let us summarise the main points of this work here.

The first consideration is related to the crystal structure. Spontaneous electric and magnetic polarisation must be allowed by the symmetry, and only 13 point groups allow simultaneously both orders. Additionally, there are chemical and electrical criteria to fulfil. To exist, a net magnetic ordering needs partially occupied d or f orbitals, whereas common FE perovskites oxides have empty d orbitals. Moreover, partially occupied d (or f) orbitals tend to occupy centrosymmetric sites in perovksite oxides.

Fortunately, most FE materials adopt a perovskite-related structure, which can be engineered to become magnetic by a clever choice of magnetic atom to combine. The perovskite structure becomes then a convenient solution for overcoming the excluding nature of ferroelectric and magnetic orders by creating materials with a magnetic A site and ferroelectric B site (e.g. $EuTiO_3$) or vice versa (e.g. $BiFeO_3$).

1.4.2 DIFFERENT TYPES OF MULTIFERROICS

Multiferroics can be divided into two groups – type-I and type-II – depending on the independant or common origin of ferroelectricity and magnetism [22]. We present here the type-I, which is directly related to this thesis, and only briefly mention the type-II.

TYPE-I MULTIFERROICS

In type-I multiferroics (MF-I), magnetism and ferroelectricity have different sources and appear independently. Typically, ferroelectricity appears at higher temperature than magnetism. While these materials are, in general, good ferroelectrics with a large polarisation value, between 10 and 100 $\mu C/cm^2$, the coupling between ferroelectricity and magnetism is weak and represents a challenge. In addition to the d^0 case already mentioned earlier, MF-I can be further classified into subgroups depending on the origin of ferroelectricity such as :

- **Lone pairs** : Two outer ns electrons, not participating in bonds, hybridise with p orbitals in one direction and induce a FE distortion. This type of MF-I will be further presented in the next section with the specific case of $BiFeO_3$.

- **Charge ordering** : In systems containing transition-metal ions with inequivalent valence, after ordering, the sites and bonds remain inequivalent and break the centrosymmetry of the system, inducing ferroelectricity [23]. This is the case for example in Fe_3O_4.

- **Geometric** : The primary distortion is a rotational mode, either polar (e.g. $BaNiF_4$) [24] or having a polar mode coupled to it (e.g. $YMnO_3$) [25].

TYPE-II MULTIFERROICS

In type-II multiferroics (MF-II), at higher temperature the system is only magnetic and when the temperature lowers, a specific magnetic order induces ferroelectricity. The result is the exact opposite than MF-I: ferroelectricity is weak but strongly coupled to magnetism. We can distinguish two subgroups depending on wether the magnetic order forms a magnetic spiral (e.g. $TbMnO_3$) or is collinear (e.g. Ca_3CoMnO_6).

A possible mechanism to induce ferroelectricity from the magnetic order is the inverse Dzyaloshinskii-Moriya interaction (IDMI) [26]. It can be seen as a structural response to the Dzyaloshinskii-Moriya interaction (DMI) [27, 28].

While the coupling between two nearest neighbour cations through a non-magnetic anion favours an antiparallel alignment of the spins (superexchange), the interaction between a spin and its angular momentum (spin-orbit coupling) favours perpendicular arrangement of the spins. The absence of inversion center between the spins can give rise to the DMI, whose Hamiltonian can be written as:

$$H_{DM} = -\mathbf{D}_{ij} \cdot (\mathbf{S}_i \wedge \mathbf{S}_j) \quad \text{, with} \quad \mathbf{D}_{ij} \propto (\mathbf{r}_i \wedge \mathbf{r}_j) = (\mathbf{d}_{ij} \wedge \mathbf{r}_{ij}) \tag{1.12}$$

where $\mathbf{S}_i$ and $\mathbf{S}_j$ are the spins of the neareast-neighbour magnetic cations, $\mathbf{r}_i$, $\mathbf{r}_j$ are the vectors connecting the magnetic cations with the intermediate anion, $\mathbf{r}_{ij}$ is the vector connecting the magnetic cations and $\mathbf{d}_{ij}$ the vector of displacement of the anion with respect to $\mathbf{r}_{ij}$ (see Fig. 4a).

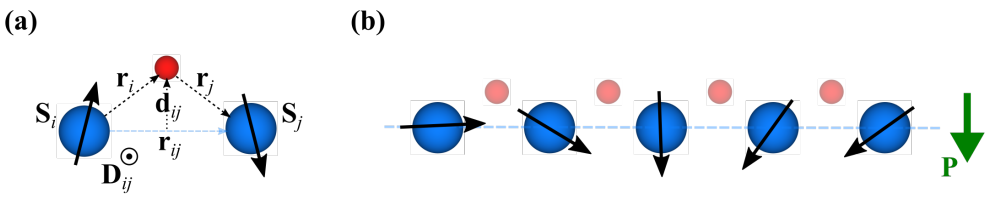

Figure 4: DMI and spin spiral. (a) Neighbouring spins $\mathbf{S}_i$ and $\mathbf{S}_j$ are canted due to the DMI. (b) The spins form a spiral that induces a net polarisation perpendicular to the propagation of the spin spiral.

While in an ideal perovskite structure, the three atoms are aligned and the DMI is zero ($\mathbf{D}_{ij} = 0$), in a distorted crystal without an inversion center between the spins, DMI results in a canting of the spins, which can induce a weak FM behaviour. The energy lowering increases when the displacement vector $\mathbf{d}_{ij}$ increases (see Fig. 4a). For special magnetic configurations such as spin spirals, as the term $(\mathbf{S}_i \wedge \mathbf{S}_j)$ between nearest-neighbour spins always has the same sign,

the DMI always displaces the anions in the same direction and thus creates a net polarisation perpendicular to the chain of spins (see Fig. 4b) [29]:

$$\mathbf{P}_{ij} \propto \sum_{(i,j)} \mathbf{r}_{ij} \cdot (\mathbf{S}_i \wedge \mathbf{S}_j) \tag{1.13}$$

As the polarisation is directly related to the spin-orbit coupling, which is relatively small, the induced polarisation is therefore relatively small also.

1.5 BISMUTH FERRITE: AN OVERVIEW

1.5.1 STRUCTURE AND PROPERTIES

Among all identified multiferroic materials, bismuth ferrite ($BiFeO_3$ – BFO) is undoubtedly the most studied one with hundreds of theoretical and experimental papers on it. This attention is largely due to the coexistence of magnetic (AFM) and ferroelectric order at room temperature. This MF-I material has a Curie temperature of around 1100K and a Néel temperature of 643K [30].

In its ground state, BFO adopts a distorted perovskite structure of rhombohedral symmetry (space group R3c) [31] with anti-ferrodistortive rotations of the oxygen octahedra around the pseudo-cubic [111] axis combined with a large spontaneous polarisation along the [111] direction [32] of about $90 - 100$ $\mu C/cm^2$ [11, 33] as presented in Fig. 5a. The perovskite-like unit cell has a pseudo-cubic lattice parameter of 3.965 Å and a rhombohedral angle of about 89.4° at room temperature [32, 34]. The ferroelectricity originates from the $6s^2$ lone pair of electrons on the Bi^{3+} ions and the antiferromagnetic G-type order (see Fig. 5b) is due to the strong superexchange between the Fe^{3+} $3d^5$ electrons.

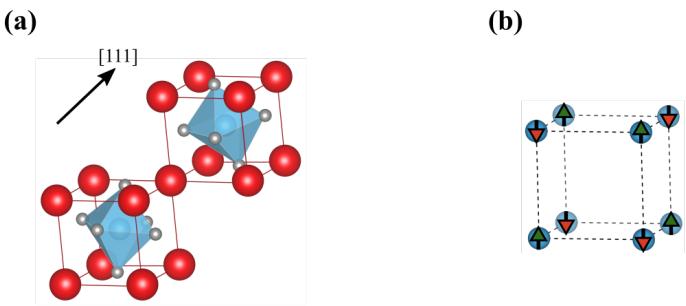

Figure 5: Crystal structure of BFO and G-type AFM. (a) R3c phase of BFO, with bismuth atoms in red, iron atoms in blue and oxygen atoms in grey. The [111] direction indicates the orientations of the polarisation. (b) G-type antiferromagnetism with AFM couplings between nearest neighbour spins (in-plane and out-of-plane). Up spins are represented by green arrows and down spins by red arrows.

1.5.2 WEAK FERROMAGNETISM

While it is clear that nearest iron sites should have opposite spin (G-type), it is less clear how they are oriented relative to the polarisation. Due to the anisotropy of the crystal structure of BFO, the spins can align either along the [111] direction (parallel to the polarisation) or within the (111) plane (perpendicular to the polarisation). It was shown using first-principles calculations that the second option is energetically more favourable [35] and it was further shown that DMI induces a small canting moment of about 1°, resulting in a weak ferromagnetism of around 0.1 μ_B per unit cell [35].

Unfortunately, the competition between the isotropic superexchange and the DMI between neareast-neighbour spins induces a spin spiral structure [36, 37]. The magnetisation is then sinusoidally modulated under the spin spiral with a longwavelength period of about 620 Å [37]. The result of this spin spiral is to cancel the net magnetisation in bulk.

1.6 THIN-FILM GEOMETRY

One of the most interesting aspects of oxide perovskites is the large flexibility of their structure, enabling the synthesis of a wide variety of materials. Furthermore, the functionalities of these materials are strongly coupled with their structure. Often many low-energy phases with distinct functionalities compete with the ground state and small external perturbations can favour one phase over the other.

The substantial intrinsic functionalities of complex oxides can be further enhanced by growing them as thin films in superlattices or heterostructures. These geometries provide further influence on the properties through a large number of possible control parameters that can modify the inherent features or even provide access to new physics. These control parameters can be of structural nature such as strain, octahedral mismatch at the interface or size effects for example, or of electronic nature such as polar discontinuity, charge transfer or magnetic interactions, among others.

Let us discuss briefly the basics of two common aspects that are particularly relevant for this work.

1.6.1 STRAINED THIN FILMS

A very common route to engineer functionalities is by straining the system. This change in energy relies on the fact that, under coherent growth, a film and its substrate have the same lattice parameters, being those of the substrate. This change in lattice constant has a strong influence on the oxygen octahedra, that can either change the metal-oxygen distance ($B-O$ bond length) (see Fig. 6a-b) or modify the tilt pattern by rotating the octahedra ($B-O-B$ angles) (see Fig. 6c). The first case will have an influence on the crystal-field splitting and the second one on the magnetic superexchange interaction [38]. In reality, any

intermediate case can happen in which bond lengths and tilt angles change. Furthermore, as strain and ferroelectricity are strongly coupled, a change in lattice constants can for example induce ferroelectricity in otherwise paraelectric $SrTiO_3$ [39] or enhance the polarisation in $BiFeO_3$ [40, 41].

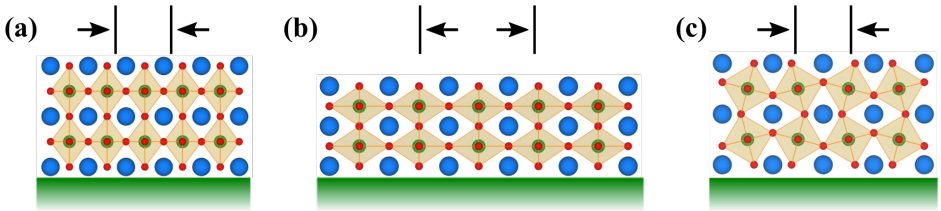

Figure 6: Effect of strain. (a) Compressive strain. The substrate (in green) has a smaller lattice constant than that of the film, which shortens the B-O bonds. (b) Tensile strain. The substrate has a larger lattice constant than that of the film, which elongates the B-O bonds. (c) Tilt. The strain induced by the substrate is accommodated by the film through tilting of the octahedra. We display one type of tilt but it could be rotated along other directions. The direction of strain is indicated by the black arrows. (Image inspired from Ref. [38])

1.6.2 POLAR DISCONTINUITY AND DEPOLARISING FIELD

Any insulating material with net dipoles in its bulk induces bound charges at the surface, with the surface charges (σ_{surf}) given by the projection of the bulk polarisation ($\mathbf{P}_{bulk}$) on the surface normal ($\hat{\mathbf{n}}$):

$$\sigma_{surf} = \mathbf{P}_{bulk} \cdot \hat{\mathbf{n}} \tag{1.14}$$

The bulk polarisation can have contributions from the spontaneous polarisation in the case of a ferroelectric material as well as from charged ionic layers in some cases [42].

Although it is a direct consequence of the bulk polarisation, a polar surface can never be thermodynamically stable due to its diverging electrostatic energy (the electrical potential diverges with the thickness [43]).

In the context of polarisable dielectric materials, we can define the electric displacement field:

$$\mathbf{D} = \varepsilon_0 \mathbf{E} + \mathbf{P} \quad , \tag{1.15}$$

where $\mathbf{D}$ is the electric displacement field, $\mathbf{E}$ the macroscopic internal field, $\mathbf{P}$ the polarisation and ε_0 the permittivity of the free space.

According to Gauss' law, in the absence of free charges, the electric displacement field must be conserved. Thus, under no applied external field, the internal field is the exact opposite of the polarisation (times ε_0). In ferroelectric materials, this field is known as the depolarising field, and tends to destabilise the polarisation perpendicular to the surface. Several different scenarios exist to suppress the depolarising field:

1. *External screening*: In the case of a FE material surrounded by metallic electrodes, the surface charges can be partially screened by the free charges of the metal. In the ideal case of a hypothetical perfect metal, the screening is total and the ferroelectric material conserves its polarisation. In reality, there are no such metals and the screening is only partial, reducing only partially the coupling energy between polarisation and depolarising field. This results in the existence of a critical thickness of the FE material under which polar distortions are unfavourable [44].

2. *Internal screening*: In the case of a FE material surrounded by a non-polar insulator, the screening mechanism can originate from the excitation of electron-hole pairs across the band gap [45], although this is usually expensive for ferroelectrics due to their large band gap or by polarising the surrounding insulator.

3. *Rotation of the polarisation vector*: Another way of canceling the surface charges is by rotating the polarisation from out-of-plane to in-plane. This consists in reorienting the structure, which has to be energetically allowed (e.g. by the strain energy).

4. *Formation of domains*: By forming polar domains of opposite directions, the bound charges can be averaged to a value close to zero. The size of the domains will be determined by a balance between the domain wall energy (energy cost of matching two neighbour domains with opposite orientation) and the remaining depolarising field.

5. *Phase transition*: Finally, a transition to a phase without out-of-plane polarisation results in no bound charges at the interface. The phase could either be non-polar or polar with in-plane polarisation.

In practice, the scenario happening will depend on the energy cost involved for each case.

1.7 GOALS AND STRUCTURE OF THIS THESIS

The general objective of this work is to identify and control new functionalities in $BiFeO_3$ going beyond ferroelectricity and antiferromagnetism. For that purpose, I use first-principles–based calculations to identify and predict new phases of $BiFeO_3$ with new properties, as well as to explore their stability in specific superlattices. By identify, I refer to projects where experimental observations preceded my theoretical work and by predict, I refer to projects with no prior experimental knowledge and whose aim is to anticipate possible aspects of BFO. This thesis is separated in five parts and is structured as follows.

The first part provides the general (chapter 1) and theoretical (chapter 2) background important for understanding the rest of this work.

The second part, containing chapter 3, chapter 4 and chapter 5 is dedicated to the investigation of new structures of BFO, stable in thin film superlattices.

The common denominator of these chapters is the use of heterostructures to engineer boundary conditions and in turn stabilise new structures.
Chapter 3 is motivated by the experimental observations of two new distortions of BFO in superlattices of $BiFeO_3$/(La,Bi)FeO_3 and consists of identifying these distortions and discussing the reasons for their stability. In particular, I discuss the effect of strain and how the control of the electrostatic boundary conditions through the choice of surrounding material in the heterostructure, can allow the control of new functionalities in BFO and possibly in other materials.
In chapter 4, I show that more phases with large unit cells exist in the phase space of BFO and discuss their characteristics and possibility to be stabilised in heterostructures.
Chapter 5 is motivated by experimental results studying highly-strained $BiFeO_3$/$CaCeMnO_3$ heterostructures grown on $LaAlO_3$. The experiments report that BFO does not have a critical thickness for the ferroelectricity, but reduces the out-of-plane lattice parameter when an electrode is place on the top surface. In this chapter I discuss the absence of critical thickness as well as the origin of the reduction of tetragonality.

In the third part (Chapter 6), I investigate a new multiferroic candidate material, $Bi_6Fe_{32}O_{57}$ and study its magnetic and ferroelectric properties.

In the fourth part (Chapter 7), I present an approach combining density functional theory calculations and machine learning methods in order to explore the energy surface of BFO and identify new phases.

Finally, I conclude this work in the fifth part (Chapter 8) and give possible outlooks to this thesis.

Theoretical Methods

2

Materials consist in an arrangement of atoms, ions and electrons interacting with each others through electric forces and their stability can in principle be explained by Schrödinger equation. While this differential equation is easily solved analytically for the hydrogen atom (see any undergraduate text book), even a numerical solution becomes impossible to find when it comes to real materials.

First-principles modelling of materials at the atomistic level became over the years a fundamental aspect of research. By *first-principles*, we refer to the use of fundamental laws of Physics only without requiring inputs from experiments. In the context of materials science and condensed matter physics, this type of modelling requires one to overcome the unsolvability of the many-body Schrödinger equation. One route to this, through reasonable and physical approximations, is the so called *density functional theory* (DFT).

In this chapter we will first present the many-body Schrödinger equation before introducing the different approximations leading to the formulation of DFT. We will then introduce certain extensions to standard DFT which allow us to describe ferroelectric materials and especially BFO accurately.

2.1 THE QUANTUM MANY-BODY PROBLEM

Materials can form due to the complex balance between kinetic energy of particules, repulsive Coulomb interaction between pairs of electrons and pairs of nuclei on one side, and on the other side the attractive Coulomb interaction between electrons and nuclei. These interactions are summarised in the non-relativistic many-body Hamiltonian for N electrons and M nuclei:

$$\begin{aligned}\hat{H} = &-\sum_{\alpha}\frac{\hbar^2}{2M_\alpha}\nabla_\alpha^2 - \sum_{i}\frac{\hbar^2}{2m_e}\nabla_i^2 \\ &+\frac{e^2}{2}\sum_{\alpha\neq\beta}\frac{Z_\alpha Z_\beta}{\|\mathbf{R}_\alpha-\mathbf{R}_\beta\|} + \frac{e^2}{2}\sum_{i\neq j}\frac{1}{\|\mathbf{r}_i-\mathbf{r}_j\|} - e^2\sum_{i,\alpha}\frac{Z_\alpha}{\|\mathbf{r}_i-\mathbf{R}_\alpha\|} \quad ,\end{aligned} \tag{2.1}$$

where the electrons are characterised by their coordinates $\mathbf{r} \equiv \{\mathbf{r}_i; i = 1, ..., N\}$, their masses m_e and their electronic charges e, while the nuclei are expressed in terms of their coordinates $\mathbf{R} \equiv \{\mathbf{R}_\alpha; \alpha = 1, ..., M\}$, their charges Z_α and their masses M_α.

We can now rewrite the Hamiltonian in a condensed version (keeping the order):

$$\hat{H} = \hat{T}_n(\mathbf{R}) + \hat{T}_e(\mathbf{r}) + \hat{U}_{nn}(\mathbf{R}) + \hat{U}_{ee}(\mathbf{r}) + \hat{U}_{ne}(\mathbf{r}, \mathbf{R}) \quad , \tag{2.2}$$

where the first and second terms describe the kinetic energy of the nuclei (subscript n) and of the electrons (subscript e) respectively. The third and fourth terms describe the Coulomb repulsion between the nuclei and between the electrons respectively, and the last term describes the Coulomb attraction between electrons and nuclei. Note that this expression does not account for time dependence, interactions with external electromagnetic fields and relativistic corrections.

One needs then to solve the time-independent Schrödinger equation to obtain the stationary many-body wavefunction $\Psi(\mathbf{R}, \mathbf{r})$:

$$\hat{H}\Psi(\mathbf{R}, \mathbf{r}) = E\Psi(\mathbf{R}, \mathbf{r}) \tag{2.3}$$

While $\Psi(\mathbf{R}, \mathbf{r})$ contains all the information about the system, it contains $3(M + N)$ degrees of freedom, which makes equation (2.3) impossible to solve in practice without simplifications.

2.2 BORN-OPPENHEIMER APPROXIMATION

A first step towards solving equation (2.3) can be made by realising that the mass of the nuclei is much heavier than the mass of the electrons, which means that the nuclei can be regarded as static and their kinetic energy ($\hat{T}_n(\mathbf{R})$) neglected [1]. This choice also implies that the Coulomb repulsion between the nuclei ($\hat{U}_{nn}(\mathbf{R})$) becomes simply a constant that can be added to the energy on the righthand side of equation (2.3), and becomes important only when comparing energies between different structural configurations. Moreover the Coulomb attraction between the nuclei and the electrons ($\hat{U}_{ne}(\mathbf{r}, \mathbf{R})$) can now be regarded as the external Coulomb potential of the nuclei experienced by the electrons:

$$\hat{V}_{\text{ext}}(\mathbf{r}) = -e^2 \sum_{\alpha} \frac{Z_\alpha}{\|\mathbf{r} - \mathbf{R}_\alpha\|} \tag{2.4}$$

and we can consider the wavefunction as a function of the electron coordinates only: $\Psi = \Psi(\mathbf{r}_1, ..., \mathbf{r}_N)$.

We can then rewrite the many-body Schrödinger equation as:

$$\left(\hat{T} + \hat{U} + \sum_{i}^{N} \hat{V}_{\text{ext}}(\mathbf{r}_i) \right) \Psi(\mathbf{r}_1, ..., \mathbf{r}_N)) = E\Psi(\mathbf{r}_1, ..., \mathbf{r}_N)) \quad , \tag{2.5}$$

[1] This approximation is known as the Born-Oppenheimer approximation [46]

where the first term is the kinetic energy of the electrons, the second term the Coulomb repulsion between pairs of electrons, and the third term of the Hamiltonian the external potential experienced by the electrons from the presence of the nuclei.

While the problem has been substantially simplified, it remains a very complicated interacting many-body problem to solve with 3N variables coming from the Coulomb interaction between electrons. Thus, under this formulation the problem remains analytically unsolvable and computationally very expensive, even unaffordable for most materials of interest.

2.3 DENSITY-FUNCTIONAL THEORY

The usual way to proceed to solve the Schrödinger equation is to define the potential and solve the eigenvalue problem to determine the wavefunction containting all the information about the system. One can then compute observables by calculating the expectation value of the operator corresponding to the property of interest. For instance one can access the particle density:

$$\begin{aligned} n(\mathbf{r}) &= \langle \Psi | \, \hat{n}(\mathbf{r}) \, | \Psi \rangle \\ &= N \int d\mathbf{r}_2 \int d\mathbf{r}_3 ... \int d\mathbf{r}_N \Psi^*(\mathbf{r}, \mathbf{r}_2, ..., \mathbf{r}_N) \Psi(\mathbf{r}, \mathbf{r}_2, ..., \mathbf{r}_N) \end{aligned} \tag{2.6}$$

As we saw in the previous section, the eigenvalue problem cannot be successfully solved for the many-body Schrödinger equation. We will present here, the theorems from Hohenberg and Kohn that are the starting point of DFT and show how the problem can be simplified with a clever mapping, leading to the so called Kohn and Sham equations.

2.3.1 ON THE DENSITY USING FUNCTIONALS: HOHENBERG-KOHN THEOREMS

Assuming that we can solve Schrödinger equation and determine the ground state wavefunction, we can, according to equation (2.6), compute the ground state density. Moreover, the ground state density is unique and it is also a functional[2] of the external potential.

Hohenberg and Kohn proved in a first theorem that the inverse relation holds, that is that the density is the true ground state if it minimises the total energy of the system [47].

THEOREM 1: For any system of interacting particles in an external potential, the potential is a functional of the ground state density as the wavefunction is

[2] A very unformal way of defining a functional is to consider it as a mapping from a function to a scalar. Note that a functional depends on its function and not on its function's variables.

a functional of the external potential, and it is also a function of the density. In other words, the external potential is uniquely defined by the ground state particle density $n_0(\mathbf{r})$. Thus if two potentials give rise to the same ground state density, they cannot differ more than by a constant.

THEOREM 2: There exists an energy functional $E[n]$, such that the ground state energy is given by the global minimum of $E[n]$ and a given density is the ground state density if and only if it minimises $E[n]$. This theorem can be formalised by:

$$E[n_0] \leqslant E[n] = \min_{\Psi \to n} \langle \Psi | \hat{T} + \hat{U} + \hat{V}_{\text{ext}} | \Psi \rangle \tag{2.7}$$

We can then rewrite the total energy as a function of the density explicitly:

$$\begin{aligned} E[n] &= \min_{\Psi \to n} \langle \Psi | \hat{T} + \hat{U} | \Psi \rangle + \int d^3\mathbf{r} n(\mathbf{r}) V_{\text{ext}}(\mathbf{r}) \\ &\stackrel{!}{=} F[n] + V_{ext}[n] \quad , \end{aligned} \tag{2.8}$$

where $F[n] = T[n] + U[n]$ depends only on the types of particles, and so is universal, and $V_{ext}[n]$ is system dependent and contains the information of the considered material.

In theory, once we know $n_0(\mathbf{r})$, we can calculate all properties of the system. In practice, we do not know $F[n]$ and its form is extremely complicated.

2.3.2 FROM MANY-BODY TO NON-INTERACTING: KOHN-SHAM EQUATIONS

To overcome the difficulty contained in writing down the form of $F[n]$, Kohn and Sham introduced a mapping between the many-body system and a fictional non-interacting system in an effective potential having the same density as the original system. They showed that the ground-state density can be obtained by solving the Schrödinger equation for the auxiliary system [48].

Formally, they introduced a set of non-interacting orbitals linked to the density by:

$$n(\mathbf{r}) = \sum_{\nu}^{\text{occ.}} |\phi_\nu(\mathbf{r})|^2 \quad , \tag{2.9}$$

where the sum is taken over the occupied orbitals.

The kinetic energy of the non-interacting Kohn-Sham system can then be expressed as:

$$T_{KS}[n] = \frac{\hbar^2}{2m} \sum_{\nu}^{\text{occ.}} \int d^3\mathbf{r} \Psi_\nu^*(\mathbf{r}) \nabla^2 \Psi_\nu(\mathbf{r}) \tag{2.10}$$

Similarly, the Coulomb interaction (Hartree energy) can be written as:

$$U_H[n] = e^2 \int d^3\mathbf{r} \int d^3\mathbf{r}' \frac{n(\mathbf{r})n(\mathbf{r}')}{\|\mathbf{r}-\mathbf{r}'\|} \tag{2.11}$$

And we can now rewrite the universal function as:

$$F[n] = T_{KS}[n] + U_H[n] + E_{xc}[n] \quad , \tag{2.12}$$

where $E_{xc}[n]$ is the exchange-correlation (xc) energy functional which expresses the difference of energy between the fully interacting system and the KS system. It can then be defined as:

$$E_{xc}[n] = T[n] - T_{KS}[n] + U[n] - U_H[n] \quad , \tag{2.13}$$

where $T[n]$ and $U[n]$ are the kinetic and potential functionals that we do not know for the fully interacting system.

We can finally solve the many-body problem by solving the Schrödinger equation for single particles (Kohn-Sham equations):

$$\left[\frac{-\hbar^2}{2m}\nabla^2 + V_{KS}(\mathbf{r})\right]\phi_\nu(\mathbf{r}) = \epsilon_\nu \phi_\nu(\mathbf{r}) \quad , \tag{2.14}$$

with $V_{KS}(\mathbf{r}) = V_{ext}(\mathbf{r}) + U_H(\mathbf{r}) + V_{xc}(\mathbf{r})$, the effective potential that the independent orbitals experience.

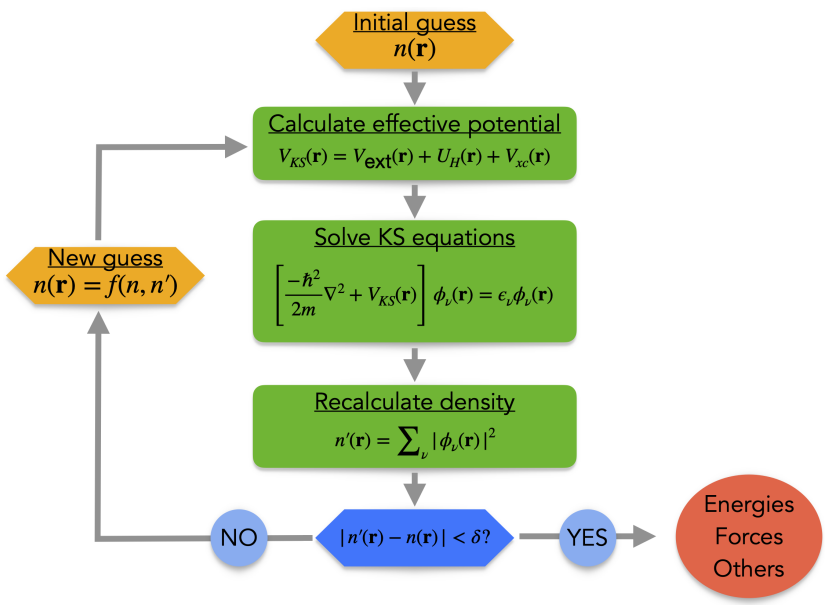

Figure 7: Flowchart of a typical self-consistent field (SCF) DFT calculation

As the solution yelding to $n_0(\mathbf{r})$ depends on $V_{KS}(\mathbf{r})$, which depends itself on the ground state density, this equation needs to be solved self-consistently. In practice we can start from a guess of $n(\mathbf{r})$, calculate $V_{KS}(\mathbf{r})$ and solve equation (2.14) to obtain the orbitals and calculate $n'(\mathbf{r})$ with equation (2.9), to compare it with $n(\mathbf{r})$. If both densities are equal (within a tolerance), the density is converged. If not, $n'(\mathbf{r})$ becomes the new starting density (with some kind of mixing with the previous steps in order to help convergence) and the process starts again (see Fig. 7).

Finally, if $E_{xc}[n]$ were known, the KS equations would be exact. Nevertheless, $E_{xc}[n]$ is usually small compared to the kinetic and the Hartree energies. It is then possible to obtain accurate results for many systems, with a good approximation of $E_{xc}[n]$. We will present in the next section different exchange-correlation functionals and corrections relevant for the results that will be presented in this thesis.

2.4 EXCHANGE-CORRELATION FUNCTIONALS

2.4.1 LOCAL DENSITY APPROXIMATION (LDA)

The simplest functional to calculate $E_{xc}[n]$ was proposed by Kohn and Sham themselves in their initial work [48], where they proposed to approximate the inhomogeneous system under study by a locally homogeneous system. For a given infinitesimal portion of space $d\mathbf{r}$, the contribution of the exchange-correlation is taken to be that of a homogeneous electron gas (HEG) with the same density $n(\mathbf{r})$. The exchange-correlation energy can then be written as:

$$E_{xc}^{LDA}[n(\mathbf{r}] = \int d\mathbf{r} \epsilon_{xc}[n(\mathbf{r})] n(\mathbf{r}) \quad , \tag{2.15}$$

where $\epsilon_{xc}[n(\mathbf{r})]$ is the exchange-correlation energy per particle of a HEG of density $n(\mathbf{r})$ at position $\mathbf{r}$. We can further decompose $\epsilon_{xc}[n(\mathbf{r})]$:

$$\epsilon_{xc}[n(\mathbf{r}] = \epsilon_x[n(\mathbf{r})] + \epsilon_c[n(\mathbf{r})] \quad , \tag{2.16}$$

where $\epsilon_x[n(\mathbf{r})]$ and $\epsilon_c[n(\mathbf{r})]$ represent the exchange and correlation contributions to $\epsilon_{xc}[n(\mathbf{r})]$. While the former is known exactly and can be derived analytically for the HEG [49], there is no exact expression for the correlation part. However, it can be accurately computed numerically [50] using Quantum Monte Carlo calculations [51]. Typically LDA underestimates $\epsilon_c[n(\mathbf{r})]$ and overestimates $\epsilon_x[n(\mathbf{r})]$, which results in good estimation of $\epsilon_{xc}[n(\mathbf{r})]$ (errors canceling each other). Due to its simplicity and good results, LDA remains widely used for electronic calculations of solids.

2.4.2 GENERALISED-GRADIENT APPROXIMATION (GGA)

In order to account for inhomogeneity, one can use a more sophisticated approach, in which the local variation in density is also taken into account through a gradient term $\nabla n(\mathbf{r})$. This approximation is known as the generalised-gradient approximation (GGA) and the functionals have the general form:

$$E_{xc}^{GGA}[n(\mathbf{r}] = \int d\mathbf{r}\, f\left(n(\mathbf{r}), \nabla n(\mathbf{r})\right) \tag{2.17}$$

There exist several GGAs, which differ in the choice of definition for the function $f\left(n(\mathbf{r}), \nabla n(\mathbf{r})\right)$ and can have very distinct results. One of the most used and reliable GGA functionals was proposed by Perdew, Burke and Ernzerhof, and is known as PBE [52].

While there is no true generality, LDA tends to underestimate the lattice parameters in crystals, and PBE tends to overestimate them. To solve this issue and have a better description of structural properties of materials, an improved PBE functional revised for solids was proposed. It is known as PBEsol [53] and is parametrised such that the lattice parameters and bond lengths are improved for solids.

2.5 CORRECTION TO LDA AND GGA: DFT+U

An important problem common to LDA and GGA is their tendency to over-delocalise valence electrons (d and f orbitals for example) and over-stabilise metallic ground states. This problem becomes particularly important in strongly correlated materials, where for example an insulator can become artificially metallic. This delocalisation problem is at the core of the wrong description of Mott insulators (which are usually metallic in DFT) and is relevant for 3d transition metals in general, thus particularly important for Fe^{3+} in BFO.

The delocalisation problem can be resolved by the so called DFT+U formalism, first introduced by Anisimov *et al.* [54] based on the Hubbard model. We will briefly introduce here the Hubbard model before presenting the DFT+U correction.

The one-band Hubbard Hamiltonian for a system of electrons can be decomposed into a kinetic term characterised by a hopping parameter t proportional to the bandwidth (dispersion) of the valence electrons, and an on-site interaction term characterised by the Coulomb repulsion between electrons on the same site with strength U:

$$H_{Hub} = -t \sum_{<i,j>,\sigma} (c_{i,\sigma}^{\dagger} c_{j,\sigma} + h.c.) + U \sum_{i} n_{i,\uparrow} n_{i,\downarrow} \quad , \tag{2.18}$$

where $< i, j >$ stands for pairs of first nearest neighbour sites, $c_{i,\sigma}^{\dagger}$, $c_{j,\sigma}$ and $n_{i,\sigma}$ are respectively the electronic creation, annihilation and number operators for an electron with spin σ on site i.

The ratio between U and t, which can be modified for example by changin U or by changing the inter-atomic spacing (changing t but not U), determines the transition from conductor to insulator:

- If $U >> t$: the energy gained by hopping is much smaller than the energy cost for having two electrons at the same site. It favour localised electrons (one electron per site).
- If $U << t$: the kinetic energy dominates as the hopping becomes favourable. It favours a delocalised system (Bloch states).

The correction proposed by Anisimov *et al.* distinguishes delocalised (s, p) and localised (d, f) electrons by adding an on-site repulsion term (similar to that in the Hubbard model) to the latter. The energy becomes then:

$$E_{DFT+U} = E^{DFT}[n] + \frac{U}{2}\sum_{i\neq j}^{(d,f)} n_i n_j - U \cdot \frac{N(N-1)}{2} \quad , \tag{2.19}$$

where the first term is the usual DFT energy, the second term is the energy penalty representing the on-site Coulomb repulsion for the localised electrons and the third term is subtracted in order to remove the double counting coming from the Coulomb interaction of N d or f electrons with (N-1) others, as LDA already has some Coulomb interaction.

This correction is particularly important for bismuth ferrite where the Fe d^5 electrons need to be correctly localised in order to obtain better accuracy (e.g. band gap).

2.6 HOW TO SOLVE IN THE KOHN-SHAM EQUATIONS IN PRACTICE

So far we formulated the many-body problem that has to be solved for materials and presented reasonable approximations to solve the Schrödinger equation in term of Kohn-Sham orbitals. We need now to provide a basis for the KS orbitals and will restrict the discussion to the formalism that will be used later in this work, noting that this represents only a small portion of the different existing methods.

2.6.1 PLANE-WAVE BASIS

According to Bloch's theorem, in a periodic potential (such as found in a crystalline solid), each wave function can be decomposed into the product of a lattice-periodic part $u(\mathbf{k}, \mathbf{r}+\mathbf{R}) = u(\mathbf{k}, \mathbf{r})$ and a plane wave $e^{i\mathbf{k}\cdot\mathbf{r}}$:

$$\varphi(\mathbf{k}, \mathbf{r}) = e^{i\mathbf{k}\cdot\mathbf{r}} \cdot u(\mathbf{k}, \mathbf{r}) \quad , \tag{2.20}$$

where $\mathbf{k}$ is the wave vector.

The lattice-periodic part can also be expanded in plane waves, whose wave vectors $\mathbf{G}$ are the reciprocal lattice vectors:

$$u(\mathbf{k},\mathbf{r}) = \sum_{\mathbf{G}} c_{\mathbf{k}}(\mathbf{G}) \cdot e^{i\mathbf{G}\cdot\mathbf{r}} \quad . \tag{2.21}$$

It becomes then natural to expand the KS orbitals in plane waves similarly:

$$\phi_\nu(\mathbf{k},\mathbf{r}) = \sum_{\mathbf{G}} C_{\nu,\mathbf{k}}(\mathbf{G}) \cdot e^{i(\mathbf{k}+\mathbf{G})\cdot\mathbf{r}} \quad . \tag{2.22}$$

In this way each orbital can be decomposed into an infinite Fourier series, whose coefficients $C_{\nu,\mathbf{k}}(\mathbf{G})$ have to be determined by solving the KS equations. In theory, one needs to find an infinite number of coefficients to find the solution, but in practice, as the values of the coefficients tend to decrease with increasing values of $|\mathbf{k}+\mathbf{G}|^2$, one can define a cut off on the kineteic energy given by:

$$E_{cut} \leqslant E_{kin} = \frac{\hbar^2}{2m}|\mathbf{k}+\mathbf{G}|^2 \quad , \tag{2.23}$$

where all plane waves with a kinetic energy smaller than the energy cut off are included.

The precision of the calculation depends on the cut off chosen, and the energy converges to the ground state energy when the cut off is increased.

2.6.2 CORE ELECTRONS AND PSEUDOPOTENTIALS

While the plane wave basis set is convenient to expand the KS orbitals, it becomes expensive to describe the core electrons (near the nuclei). Indeed, due to the diverging nature of the Coulomb interaction at small distance, the wave functions oscillate strongly near the nucleus. A very large number of plane waves is then required to describe those oscillations, which becomes practically impossible to compute. Fortunately, core states play a minimal role in determining the properties of materials and can be simplified.

The pseudopotential method is an approximation in which the core and valence electrons are treated differently. The former are considered as part of the ions and are not described in term of plane waves, while the latter are treated explicitly. The contributions from the valence electrons are then space-dependent. The oscillating part of the wave function near the nucleus is replaced by a smooth and nodeless function up to a given cut off radius, r_c, from the nucleus. The potential that yields this wavefunction as its eigenvector matches perfectly the true potential outside the cut off radius, where the plane waves are used.

The number of electrons treated explicitly is then significantly reduced and by reducing the number of radial nodes, the energy cut off can also be reduced for the valence electrons, resulting in more efficient calculations.

Part II

RESULTS I: PHASES, STRAIN AND ELECTROSTATICS

In the second part, we discuss how heterostructures can be used to engineer boundary conditions and in turn stabilise new structures.

In chapter 3, we show how, by an appropriate choice of strain and electrostatic boundary conditions, one can induce a phase transition from the polar ground state to a non-polar phase.

In chapter 4, we present a thorough study where we explore the phase space of BFO using phonon modes and identify several phases with low-energy and large unit cells. We further discuss the possibility of stabilising them experimentally in heterostructures. We include in this chapter our published work in *Physical Review Materials*.

In chapter 5, we study the case of highly-strained BFO surrounded by a metallic electrode that has ionic charged layers with a different charge than the layers in BFO. We discuss how the bound charges induced by the spontaneous polarisation and those resulting from the charged ionic layers combine, and the consequences for the electrostatic energy.

Electrostatic Engineering

3

One of the biggest challenges in integrating thin film ferroelectrics into microelectronic devices is to deal with the presence of the depolarising field. It is responsible for the loss of the net electrical polarisation at low thicknesses. As presented in section 1.6.2, there are different ways to cancel the depolarising field, such as forming domains, rotating the polarisation vector in-plane or in theory inducing a phase transition to a non-polar phase.

We show in this chapter that the latter option can happen in bismuth ferrite when appropriate electrostatic boundary conditions are chosen. This study is motivated by the experimental observations made by our collaborators Mundy et al. [55] of a new structural phase of bismuth ferrite in superlattices with lanthanum-doped bismuth ferrite ($La_xBi_{1-x}FeO_3$).

The remainder of this chapter is organised as follows. First, we will review previous relevant work on $BiFeO_3/LaFeO_3$ (BFO/LFO) superlattices and present the experimental evidence of a new phase of BFO in $BiFeO_3/La_xBi_{1-x}FeO_3$ superlattices. We will start our study by identifying the new phase by matching our DFT calculations with the experimental structures and by analysing its structure. We will then show the conditions under which this phase can be stabilised experimentally by considering the influence of strain using DFT and electrostatics through a simple phenomenological model. Finally, we will conclude the chapter by discussing the possible interesting functionalities of the new non-polar phase and the possibility of using electrostatic engineering as a general route to stabilising new phases in other materials.

This chapter is the result of an experimental and theoretical collaboration whose outcome is currently under review [56]. I present the theoretical aspects of the project that are my work. I collaborated with Quintin N. Meier to derive the electrostatic model and carried out the rest of the work alone under the supervision of Nicola A. Spaldin.

3.1 Experimental evidence

In superlattices of ferroelectric and dielectric materials, the energy of the system is determined by many factors such as for example, mismatch between octahedral rotations at the interface, strain boundary conditions imposed by the superlattice (chemical pressure) and by the substrate, and electrostatics at the interface. This interplay makes these systems complex to study but provides a large number of possibilities to control their functionalities.

In the past years, BFO/LFO superlattices have attracted attention because of the similar ionic radii of La^{3+} and Bi^{3+}[57]. While both atoms occupy an identical volume in the structure, resulting in no chemical pressure when one

substitutes the other, their influence is quite different. Indeed, BFO is FE due to the lone pair of electrons and displays $a^-a^-a^-$ Glazer rotations in its R3c ground state (see section 1.5), while the structure of LFO is centro-symmetric with Pnma symmetry and $a^-a^-c^+$ rotations (see Fig. 8). Both materials are antiferromagnetic with G-type ordering of the magnetic moments.

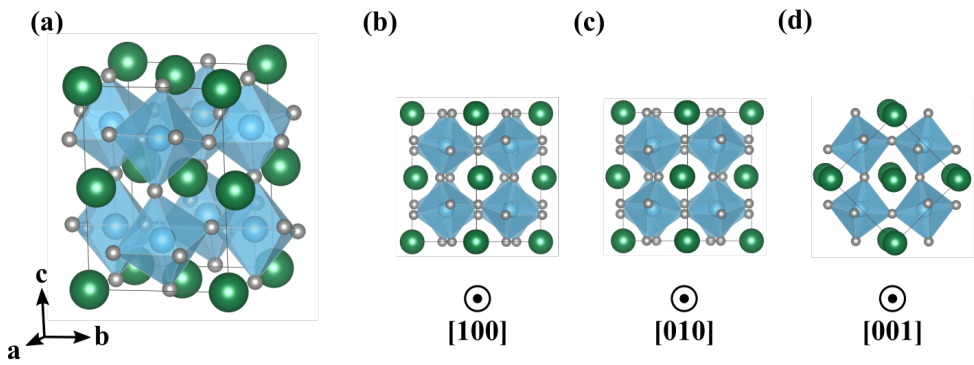

Figure 8: Ground state structure of $LaFeO_3$ with Pnma symmetry. (a) Full unit cell with La, Fe and O represented respectively by green , blue and grey atoms. (b-d) Projections with anti-phase tilts along [100] and [010] and in-phase tilts along [001]. We orientate pseudo-cubic [001] along the **c** vector and [010] along the $\mathbf{a}+\mathbf{b}$ direction. The rotation patterns correspond to $a^-a^-c^+$ in Glazer notation.

As the Pnma structure is a metastable phase of BFO with very low energy [58], the superlattice can structurally be seen as BFO with polar and non-polar layers, or similarly as the competition between R3c and Pnma (making abstraction of the chemistry). This competition can be studied by varying the composition of BFO and LFO within a superlattice. It is intuitive that for very large BFO-composition the superlattice will adopt the R3c symmetry and for opposite composition, the Pnma symmetry of LFO. In between these extreme cases, things are more complicated and different studies provided good insights as we will see next.

3.1.1 PREVIOUS RESULTS ON BFO/LFO SUPERLATTICES AND LANTHANUM-DOPED BFO

BFO/LFO superlattices grown on different substrates have been investigated by various groups. Rispens et al. carried out X-ray diffraction experiments and reported that the superlattice changes symmetry depending on the BFO fraction when grown on (110) orthorhombic $DyScO_3$ substrates. Below a BFO fraction of 0.4 the superlattice adopts the Pnma symmetry and beyond a BFO fraction of 0.8 the R3c symmetry is preferred. Between those fractions, a mixed zone has been reported but no symmetry is identified [59]. Zanolli et al. carried out DFT calculations on 1/1 superlattices and predicted that the intermediate fraction

could have the $Pmc2_1$ symmetry [60]. Note that unit cells of 40 atoms were considered for each material in the calculations.

A few years later, Carcan et al. studied the same superlattices grown on cubic $SrTiO_3$ (100) and MgO (100) focusing on the mixed region with BFO fraction ranging from 0.25 to 0.8. They complemented their investigations with Raman spectroscopy and TEM (transmision electron microscopy) and reported that the mixed region has a $PbZrO_3$-like symmetry ($Pbam$ phase) for intermediate fractions of BFO. Additionally, they reported a mixture of $Pnma$ and $Pbam$ and attributed the competition and stability of the newly reported phase to the strain imposed by the substrate and the octahedral rotation/tilt (in)compatibility at the interfaces [61].

Other studies considering site-sharing instead of superlattices, revealed similar results. González-Vázquez et al. used first-principles calculations to study the structural phases of $La_xBi_{1-x}FeO_3$ (LBFO) as a function of the La concentration. In particular, they constructed supercells of 40 atoms with different concentrations of La and considered all possible distortions compatible with the unit cell. Based on their DFT results, they concluded that a ferroelectric $Pna2_1$ phase and paralectric $Pnma$ phases are equally stable for concentrations between 0.3 and 0.65 [62]. Unsurprisingly, at lower concentrations the superlattice adopts the BFO-like structure and at higher ones the LFO-like structure is stable. Similar conclusions were made in another theoretical study by Lee et al. [63], where La concentrations of beyond 0.3 $Pnma$ were found to be stable.

To summarise, we see from the various studies presented above, that at intermediate fractions of BFO in BFO/LFO superlattices, BFO adopts a structure that likely has $Pbam$ symmetry. It was previously believed [61] that strain and octahedral mismatch are the main ingredients for stabilising this phase in the whole structure. On the other hand, theoretical studies focusing on the effect of La alloying in BFO concluded that $La_xBi_{1-x}FeO_3$ adopts the centrosymmetric $Pnma$ symmetry when $x > 0.3$.

3.1.2 NEW BFO STRUCTURES: STEM IMAGES

In order to better understand these systems, Mundy et al. investiage experimentally superlattices of $(La_xBi_{1-x}FeO_3)_n/(BiFeO_3)_n$, with $n = 2-20$ unit cells and $x = 0.3$ or 0.4, grown on $(001)_{pc}$ (pseudo-cubic) $TbScO_3$ using reactive molecular-beam epitaxy [55]. Scanning transmission electron microscopy (STEM) images reveal two different distortion patterns in the BFO layers, while the LBFO layers display the usual distortions present in LFO ($Pnma$), in agreement with theoretical predictions for these concentrations [62, 63].

The distortions observed correspond to displacements of the Bi atoms in two different manners. The first type of distortions consists of a "2up-2down" displacement along the $[001]_{pc}$ direction (vertical) in which the pairs of Bi atoms are displaced positively (up) or negatively (down) along the vertical direction (see Fig. 9a), similar to the distortions present in $PbZrO_3$ as already reported [61]. The second type of distortions is displayed in Fig. 9b, where horizontal and diagonal dumbbells are visible and similarly capture along another direc-

tion in Fig. 9c, where the Bi atoms are alternatively displaced in a "2up-2down / flat / 2down-2up" pattern along the vertical direction. While the former type of distortions is consistent with previous reports, the latter was not reported previously.

Finally, lowering the La-concentration from 0.4 to 0.3 does not affect the structure of the LBFO layers but results in coexistence between regions with the distortions presented in Fig. 9 and regions displaying 109° or 180° domain walls (DW) of the R3c phase [55].

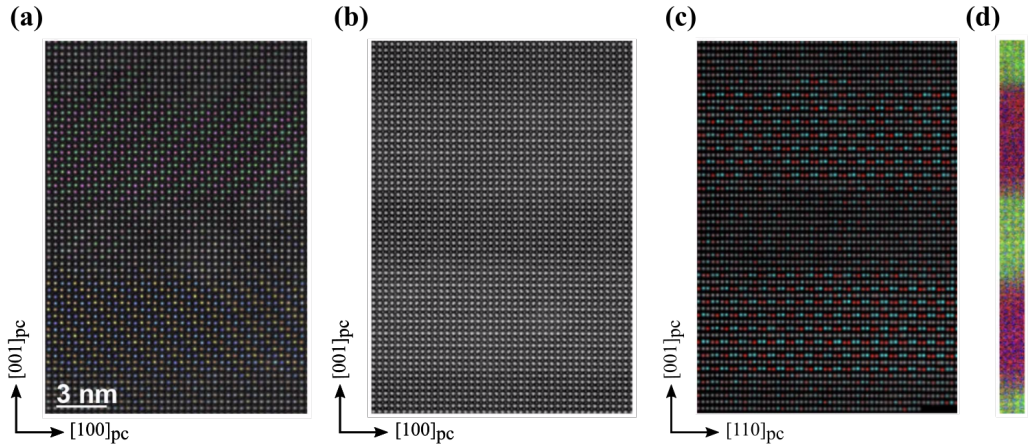

Figure 9: STEM images of the $(La_{0.4}Bi_{0.6}FeO_3)_{15}/(BiFeO_3)_{15}$ superlattices. Two different distortions are observed in the BFO layer. (a) Pairs of Bi atoms moving up or down along the $[001]_{pc}$ direction. (b) Alternating horizontal and diagonal dumbbells imaged for the Bi atoms. (c) The same region as (b) is imaged with a 45° axis to the $[100]_{pc}$ direction. Accross the $[001]_{pc}$ direction, pairs of Bi are displaced up (respectively down) in a row of atoms, not displaced in the next row, and displaced down (respectively up) in the third row. (d) Electron energy loss spectroscopy (EELS) showing the atomic concentration of lanthanum (green) and bismuth (red) across the superlattices. The images are adapted from Ref. [55]. Courtesy of Julia Mundy.

3.2 COMPUTATIONAL DETAILS

The results that are presented below are based on DFT calculations using the Vienna *ab initio* package (VASP) [64–67]. The projector augmented wave (PAW) method is used [68, 69] with explicit treatment of the following valence electron configuration: $6s^2 6p^3$ for Bi, $3d^7 4s^1$ for Fe and $2s^2 2p^4$ for O. An $8 \times 8 \times 8$ k-point Γ-centered Monkhorst-Pack mesh [70] is used to sample the Brillouin zone corresponding to a 10-atom cell and an energy cutoff of 800 eV for the plane wave basis is chosen. For the xc functional we use PBEsol [53] with an effective Hubbard-like correction, $U_{eff} = 4$ eV, for the Fe d orbitals according to Dudarev's approach [71]. G-type antiferromagnetism is adopted for all the calculations.

3.3 IDENTIFYING THE DISTORTIONS

Our first step is to identify the phases observed experimentally. From Fig. 9 we can infer that all phases display anti-polar displacements and we mentioned so far two antipolar phases: $Pnma$ and $Pbam$. The former has a unit cell dimensions of $\sqrt{2}a_0 \times \sqrt{2}a_0 \times 2a_0$[1] (20 atoms per unit cell) and the latter has dimensions $\sqrt{2}a_0 \times 2\sqrt{2}a_0 \times 2a_0$ (40 atoms per unit cell).

The periodicity of the distortions can provide a first guess for the unit-cell size required. On one hand, it appears from Fig. 9a that a unit cell including two pairs of Bi atoms over two rows could reproduce the periodicity if a pair of atoms is moving upward and the other pair is displaced downward; this unit cell size corresponds to that of $Pbam$. On the other hand, Fig. 9c displays a larger unit cell in which the unit cell should include four rows of atoms with four atoms per row to reproduce the displacement pattern. We are then looking for phases similar to $Pbam$ but with possibly 16 Bi atoms per unit cell in order to capture all the patterns of displacements along the different orientations. We proceed with our search by analysing the phonon dispersion.

3.3.1 PHONON INSTABILITIES

In general, a crystal is stable (i.e. at equilibrium) if its potential energy increases under any combination of atomic displacements. It is possible to compute the forces between each pair of atoms and construct the force matrix constant of the crystal in order to construct the normal modes at any particular wave vector. One way to construct the force matrix constant is the so called Frozen-Phonon method that consists of displacing all atoms individually and computing the forces generated on all the other atoms. In the harmonic approximation, a normal mode with imaginary frequency represents a set of distortions in the crystal that lower the energy of the unstable configuration. We will then use this method in order to look for new (meta)stable phases and we use the Phonopy package [72] to compute the phonon dispersion.

We consider as a starting point the $Pbam$ phase (Fig. 10a-b) and compute the phonon frequencies at the Γ and Z points of the corresponding Brillouin zone (see Fig. 10c). The former symmetry point reveals an unstable mode lowering the symmetry from $Pbam$ to $P2_1/c$ (with the same number of atoms per unit cell). The latter reveals an unstable mode that lowers the symmetry to $Pnma$ with a larger unit cell (doubled along the c-axis with respect to the $Pbam$ phase). Compared to the $Pnma$ ground-state structure of LFO, the new phase with the same symmetry contains four times the number of atoms, since its unit cell is doubled along **b** and **c** with respect to LFO-like $Pnma$. To distinguish between the two $Pnma$ structures we will label the new phase $Pnma(1)$.

[1] a_0 is the lattice parameter of a reference cubic lattice

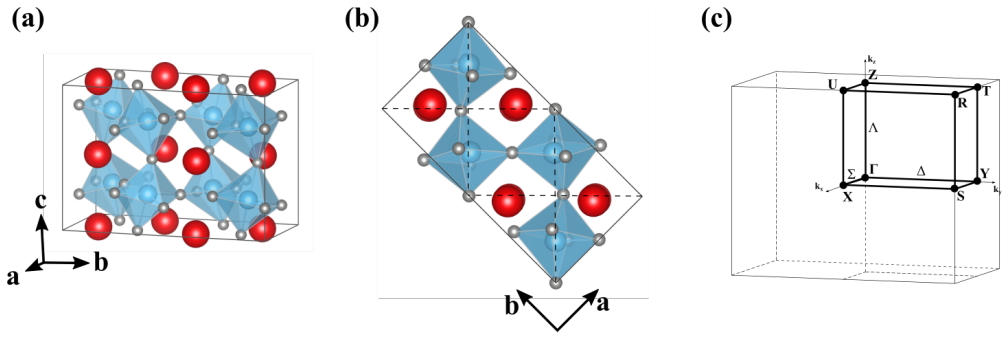

Figure 10: BFO with Pbam symmetry and its Brillouin zone. (a) Full unit cell of the Pbam phase with Bi, Fe and O represented respectively by red, blue and grey spheres. (b) Projection along the c-axis, which is perpendicular to the structure. The 2up-2down displacement of the Bi atoms is highlighted by the dashed lines corresponding to the symmetric position in the absence of distortions. (c) Brillouin zone of the $Pbam$ unit cell.

In Fig. 11 we compare the structures of both newly identified phases ($P2_1/c$ in Fig. 11a-c and $Pnma(1)$ in 11d-f) with the experimental structures (Fig. 11g-i). While both phases display the "2up-2down" displacement (Fig. 11a,d,g) matching the first type of structures in the experiment, the structure of $P2_1/c$ only contains 8 Bi atoms. Another orientation of the $Pnma(1)$ phase reveals the same patterns of displacements present in the experiment (Fig. 11f and i) where pairs of bismuth atoms are alternatively displaced "2up-2down / flat / 2down-2up". These out-of-plane antipolar displacements combined with the in-plane "2up-2down" displacement result in the diagonal and horizontal dumbbells observed (Fig. 11e and h).

Therefore, we conclude that the different structures present in the experiment correspond to the $Pnma(1)$ phase differently oriented.

3.3.2 A NEW $Pnma$ PHASE WITH LARGER UNIT CELL

The unit cell of the new metastable phase with $Pnma$ symmetry has the lattice vectors: $a = 5.53$ Å, $b = 11.15$ Å and $c = 15.64$ Å. As mentioned earlier, the unit cell is doubled along **c** with respect to $Pbam$, due to the presence of the extra "2up-2down / flat / 2down-2up" displacements. We test different magnetic orderings and find that G-type AFM stays energetically the most favourable. Let us present in more detail the $Pnma(1)$ structure before exploring the reasons for its stability in the LBFO/BFO superlattices.

A convenient way to understand a crystal structure is by decomposing it into irreducible normal distortion modes that can be seen as pattern of displacements that break the symmetry of a parent structure. These symmetry modes form an orthogonal and complete basis, and so can represent the order parameters in structural phase transitions. We can for instance take as parent structure the ideal perovskite structure ($Pm\bar{3}m$) and describe any phase in terms of the set of distortion modes that lower the symmetry from the parent structure.

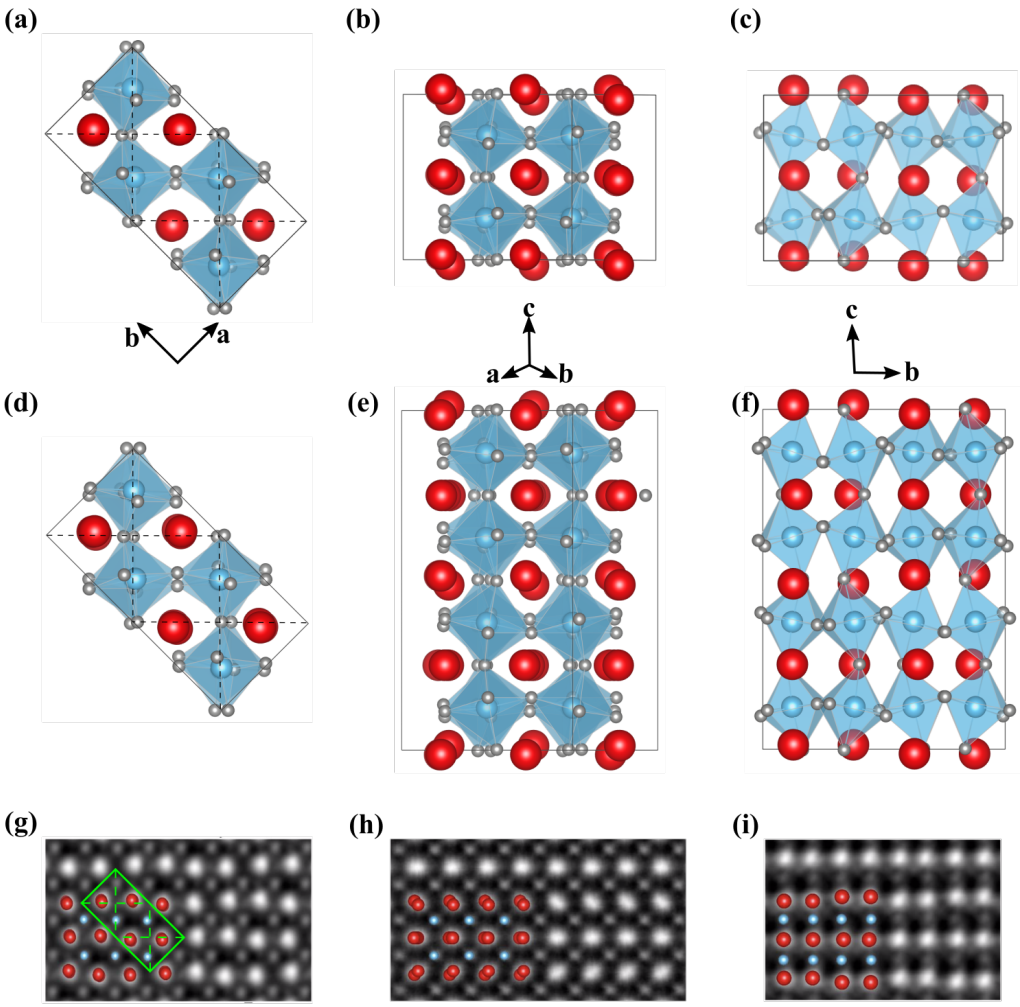

Figure 11: Comparison of the structures of $P2_1/c$ (a-c), $Pnma(1)$ (d-f) and the experimental STEM images (g-i). (a-c) The unit cell of $P2_1/c$ contains 40 atoms and presents a "2up-2down" displacement pattern in-plane (a) as well as out-of-plane (c) resulting in diagonal dumbbells (b). (d-f) The unit cell of $Pnma(1)$ contains 80 atoms and presents a "2up-2down" displacement pattern similar to $P2_1/c$ (d). Along the perpendicular direction, the Bi atoms are displaced in a "2up-2down / flat / 2down-2up" displacement pattern (f) resulting in alternating horizontal and diagonal dumbbells when rotated by 45° (e). (g-i) Close-up on a region of the BFO layer presented in Fig. 9a-c respectively. The images presented in (g-i) are adapted from Ref. [55].

We use the online software ISODISTORT [73, 74] to decompose the $Pnma(1)$ structure in five main distortion modes by including the modes that participate to at least 5% of the total distortion from the high-symmetry cubic phase. The structures that result from freezing in these modes ($R_5^-, T_2, S_2, \Lambda_3$ and Σ_2) are presented in Fig. 12. Of particular interest are the Λ_3 mode responsible for the "2up-2down / flat / 2down-2up" displacement pattern and the Σ_2 mode responsible for the "2up-2down" displacement pattern. The three other modes act mainly on the oxygen atoms inducing rotations and tilts that together with

minor contributions from the Λ_3 and Σ_2 modes result in tilt patterns not captured by the traditional Glazer notation and will be discussed later (See Chapter 4).

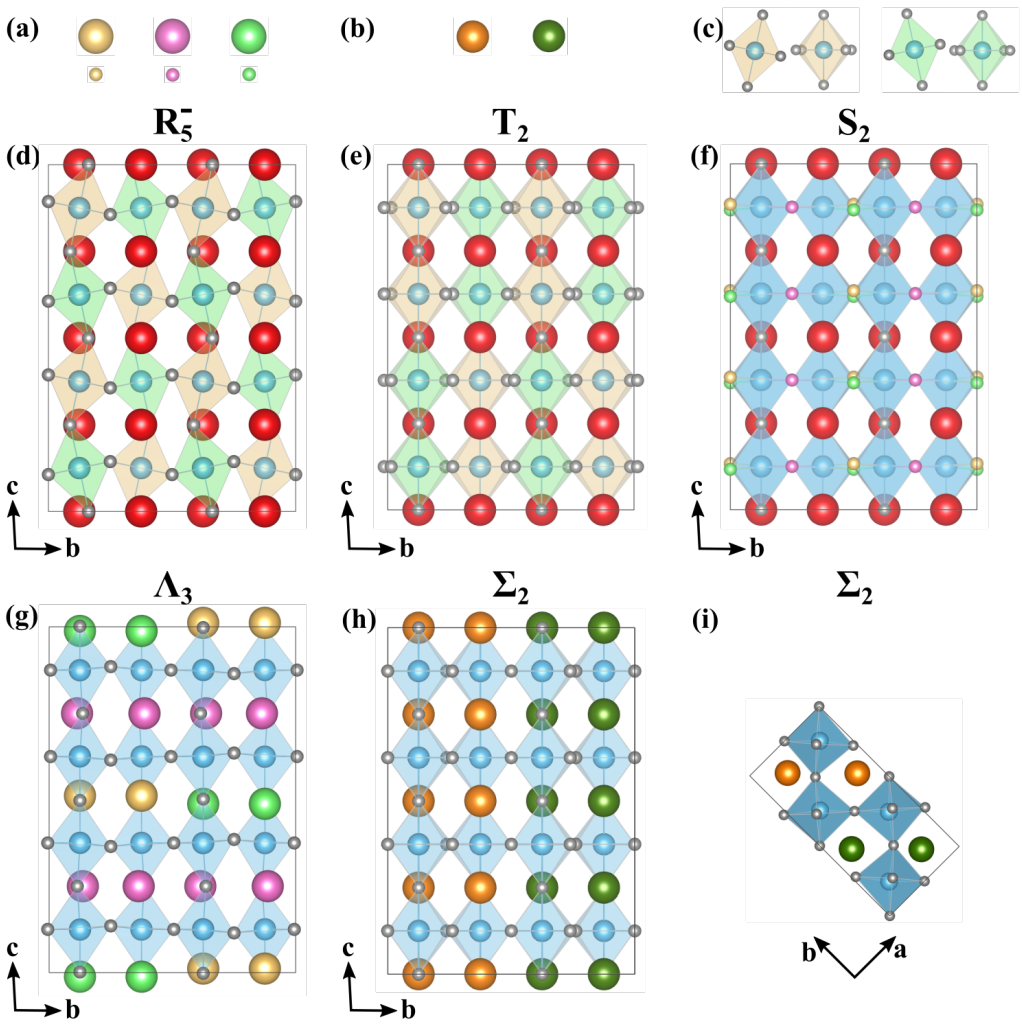

Figure 12: Main distortion modes present in Pnma(1). (a-c) Legend of the colour scheme. Additionally to the previously used colour scheme we assign new colours according to the direction of displacement of the atoms with respect to the symmetric positions and we change the previously defined colours only to display the main distortions induced by each mode. (a) From left to right, Bi (top row) or O (bottom row) atoms moving along **c**, not moving and moving along $-$**c** respectively. (b) From left to right, Bi atoms moving along $(\mathbf{a}+\mathbf{b})$ or $-(\mathbf{a}+\mathbf{b})$. (c) Octahedra rotating clockwise (first pair) or anti-clockwise (second pair) around the **a** axis (first element of each pair) or around the **c** axis (second element of each pair). (d-i) Structures resulting when the R_5^-, T_2, S_2, Λ_3 and Σ_2 modes are frozen in from the ideal cubic structure. The Λ_3 mode (g) is responsible of the "2up-2down / flat / 2down-2up" displacement pattern. (h-i) We show the structure resulting of the Σ_2 mode under two different projections, where in (i) the "2up-2down" displacements pattern is visible.

While the R_5^- mode is present in other phases such as R3c, Pnma and Pbam and Σ_2 and S_2 are found in Pbam too, the T_2 and Λ_3 modes were not previously reported for BFO phases to the best of our knowledge [2]. In order to gauge the energetic contribution from the latter modes, we can add to the cubic perovskite each mode with different amplitudes and compute the resulting energy change. The results of these calculations are presented in Fig. 13. One can see that the energy lowering resulting from the distortions produced by Λ_3 and T_2 is of the same order as that for Σ_2 and more important than S_2. Experimentally, we have access to Λ_3 through the displacements of the bismuth atoms that are visible in the STEM images but not to T_2, as one cannot capture easily the rotations of the octahedra. While we didn't consider couplings, we can argue based on intuition that Λ_3 and T_2 might be coupled since the movement of the Bi cation is likely accompanied by octahedral rotations as the Bi cation moves out the way not to increase the energy due to Coulomb repulsion between the clouds of electrons surrounding the ions.

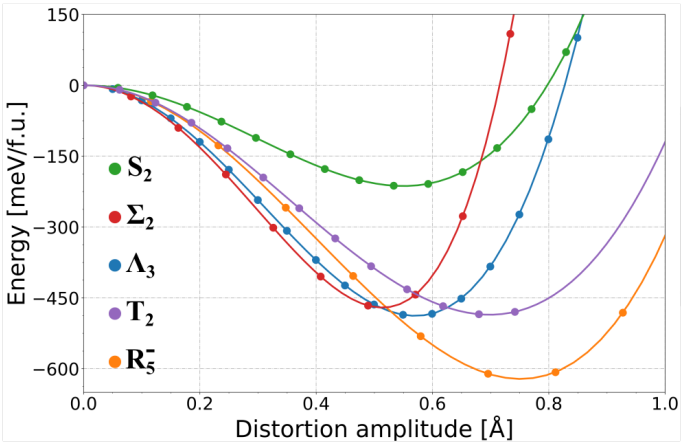

Figure 13: Calculated energy as a function of mode amplitude for each mode individually. The amplitude is normalised by a factor provided by the ratio between the volume of the parent structure ($Pm\bar{3}m$) and the structure containing the mode, allowing quantitative comparison between the modes. Note that the volume is kept fixed to that of the parent phase resulting in an underestimation of the energy lowering due to the presence of resulting stress in the structures.

[2] After finding this phase we discovered that the same structure was reported for $BiFe_{0.5}Sc_{0.5}O_3$ [75]

3.4 HOW CAN Pnma(1) BE STABLE EXPERIMENTALLY?

Now that we have identified the phase matching the distortions observed experimentally, we will address the reasons for its stability in the LBFO/BFO superlattices. As we cannot reproduce the whole superlattice on the substrate in a DFT calculation, we will decompose the different possible contributions starting with strain effects.

3.4.1 EPITAXIAL STRAIN

Experimentally, the superlattice is grown on $TbScO_3$, whose experimental lattice parameters are: $a = 5.45$ Å, $b = 5.72$ Å and $c = 7.91$ Å [76]. As a result, the substrate imposes a compressive strain of the order of 0.3% on BFO. We relax $TbScO_3$ in its Pnma ground state and obtain lattice parameters in good agreement with the experimental values: $a = 5.41$ Å, $b = 5.70$ Å and $c = 7.88$ Å. Considering that the lattice parameter of BFO in the R3c phase is 3.945 Å in our calculations, we find a similar mismatch between the lattices of both materials as reported experimentally.

To account for the strain effects from the substrate, we constrain the lattice vectors contained in one plane to match those of the substrate and keep the initial angles fixed. If a_0 is the lattice parameter of the bulk ground state (R3c), the strain imposed by the substrate with lattice a_{sub} is given by:

$$s = \frac{a_{sub} - a_0}{a_0} \tag{3.1}$$

In practice we compute the energy as a function of s by taking the average of the two in-plane lattice parameters and multiply them by s. Following this procedure we compute the strain energy for the different non-polar phases considered above for a range of strain values[3] (see Fig. 14a). We see that for small values of compressive strain, no phase becomes more stable than the ground state and the Pnma(1) phase is the lowest energy non-polar phase. Since the strain imposed by $TbScO_3$ is small, we compare the different phases at $s = 0$ (lattice parameters from unstrained R3c) and see that the Pnma(1) phase is 10 meV/f.u. below the regular Pnma and 30 meV/f.u. above the R3c phase (Fig. 14b). Note that Pbam remains the highest energy structure considered with 75 meV/f.u. above R3c.

We conclude that the small strain imposed by the substrate can contribute to lowering the energy difference between Pnma(1) and R3c but alone it is not enough to stabilise the non-polar phase.

In order to motivate the next section, let us recall that LBFO is non-polar (Pnma phase). While both phases' energies are modified by the strain, the electrostatic boundary conditions only modify the energy of the polar phase due

[3] The **a** and **b** lattice vectors are strained and **c** is relaxed

to the polar discontinuity at the interface. We will show in the next section how this extra energy cost overtakes the strain energy and makes the R3c phase unfavourable for a range of thicknesses.

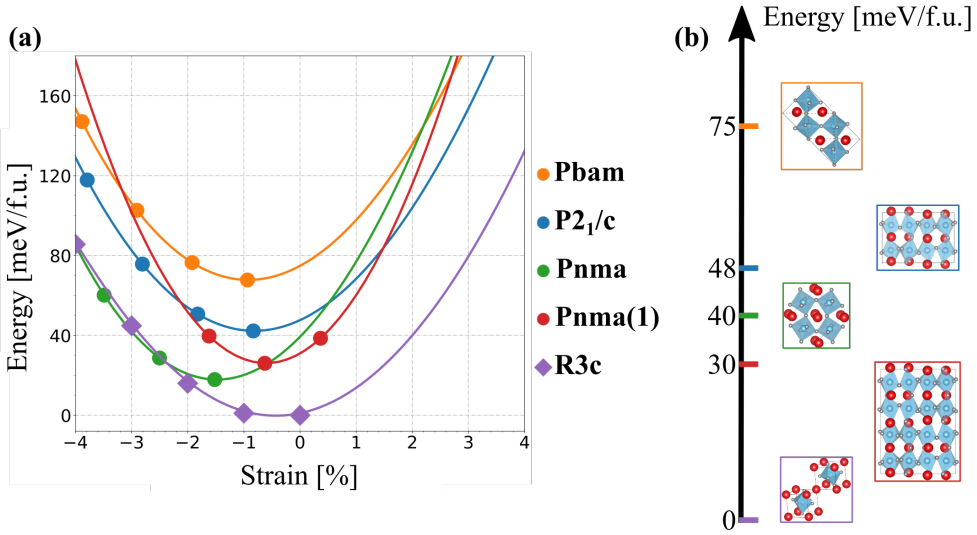

Figure 14: Strain energy. (a) Internal energy of different phases as a function of the strain. We constrain the in-plane lattice vectors of different non-polar phases (coloured dots) and the polar ground state (coloured diamonds) and compute the energy by fully relaxing the coordinates as well as the out-of-plane lattice vector. (b) Energies and structures of the phases in (a) at 0% of strain. Note that we fix the rhombohedral angle of the R3c phase to 60°.

3.4.2 POLAR DISCONTINUITY AND ELECTROSTATIC MODEL

After considering the strain energy alone, we want to consider additionally the electrostatic energy and compare the stability of the R3c phase with that of the Pnma(1) phase in the LBFO/BFO superlattices in order to see if the electrostatic energy cost can disfavor the polar ground state and explain why Pnma(1) is observed experimentally. We will first derive an expression for the electrostatic energy, before studying the stability of both phases.

As presented in section 1.6.2, bound charges form at the surfaces (or interfaces) of a ferroelectric material. In order to evaluate the contribution of those charges to the energy of the system, we consider an idealised model in which BFO is surrounded by a dielectric material under closed-circuit boundary conditions and only consider single domain structures. Note that computationally these boundary conditions are easily implemented as they come naturally with periodic boundary conditions.

The bound charges give rise to the depolarising field ϵ_d perpendicular to the interface that can be expressed as:

$$\epsilon_d = -\frac{P}{\varepsilon_r \varepsilon_0} \quad , \tag{3.2}$$

where P is the component of the polarisation perpendicular to the interface, ε_r the relative permittivity of the material in which the field is created and ε_0 the permittivity of the free space and we define $\varepsilon = \varepsilon_r \varepsilon_0$. The short-circuit boundary conditions impose that there is no potential drop along the whole superlattice and consequently, a field will appear in the insulating layer and induce a polarisation P_I [77].

The continuity of the electric displacement field at the interface imposes that

$$D_{FE} = D_I \quad \Leftrightarrow \quad \varepsilon_{FE} \epsilon_{d_{FE}} + P_{FE} = \varepsilon_I \epsilon_{d_I} + P_I \quad , \tag{3.3}$$

where we denote with subscripts the different quantities of the BFO layer (FE subscript) or dielectric layer (I subscript). In total generality, the density of surface charges at the interface is proportional to the mismatch of polarisation between both layers and so is the depolarising field induced in each material. For a film of thickness t, the electrostatic energy cost per unit area can then be expressed as

$$E_{es} = \int_0^t dz \frac{\varepsilon}{2} \epsilon_d^2 = \frac{\varepsilon}{2} \epsilon_d^2 \cdot t \quad . \tag{3.4}$$

This electrostatic energy is unfavourable and forces the system to find mechanisms to lower its energy. While different options were discussed in section 1.6.2, we assume here that the screening is provided by the creation of electron-hole pairs excited across the band gap E_g. For simplicity, we assume also that these pairs are created within the BFO layer (we will release this constraint later on). Note that this screening mechanism is likely an upper bound estimation as other sources such as defects could in principle provide carriers at lower energy cost.

For a given areal density of charges σ, the screening field is opposed to the depolarising field and can be expressed as

$$\epsilon_{scr} = \frac{\sigma}{\varepsilon} \quad . \tag{3.5}$$

The screening energy cost per unit area for creating simultaneously areal charges of density $\pm\sigma$ at both interfaces can be expressed as:

$$E_{scr} = \frac{|\sigma|}{e^-} E_g \quad , \tag{3.6}$$

where e^- is the elementary charge of an electron. We can now express the electrostatic energy as the sum of the depolarising field energy cost and the screening energy contribution:

$$
\begin{aligned}
E_{es} &= \frac{1}{2}\varepsilon\left(\epsilon_d + \epsilon_{scr}\right)^2 \cdot t + E_{scr} \\
&= \frac{1}{2}\varepsilon\left(-\frac{P}{\varepsilon} + \frac{\sigma}{\varepsilon}\right)^2 \cdot t + \frac{|\sigma|}{e^-}E_g \\
&= \frac{P^2}{2\varepsilon}t + \frac{\sigma^2}{2\varepsilon}t - \frac{P\sigma}{\varepsilon}t + \frac{|\sigma|}{e^-}E_g \quad .
\end{aligned}
\tag{3.7}
$$

From equation 3.7 we can see a competition between maintaining the polarisation in presence of the depolarising field and the energy cost associated with the generation of the screening charges in order to decrease the depolarising field. We can then minimise this equation with respect to the areal density of charges. We assume without loss of generality that $P > 0$ and $\sigma > 0$, then by solving $\frac{\partial E_{es}}{\partial \sigma} = 0$ we obtain the expression for σ that minimises the electrostatic energy:

$$
\sigma = \begin{cases} P - \frac{\varepsilon}{t}\frac{E_g}{e^-} & \text{if } t \geqslant \frac{\varepsilon}{P}\frac{E_g}{e^-} \\ 0 & \text{if } t < \frac{\varepsilon}{P}\frac{E_g}{e^-} \quad . \end{cases}
\tag{3.8}
$$

Note that the condition on the thickness guarantees that the density of screening charges does not exceed the bound charge density. We can now substitute equation 3.7 into equation 3.8 to calculate the total electrostatic energy per area unit (as a function of the film thickness):

$$
E_{es} = \begin{cases} P\frac{E_g}{e^-} - \frac{\varepsilon}{2t}\left(\frac{E_g}{e^-}\right)^2 & \text{if } t \geqslant \frac{\varepsilon}{P}\frac{E_g}{e^-} \\ \frac{1}{2}\frac{P^2}{\varepsilon} & \text{if } t < \frac{\varepsilon}{P}\frac{E_g}{e^-} \quad . \end{cases}
\tag{3.9}
$$

As expected, we obtain an electrostatic energy cost that decreases with increasing thickness of the ferroelectric film.

Now we compare the total energy of both phases as a function of the thickness of the BFO film.

Considering strain and electrostatic, the energy of the R3c phase as a function of the thickness can be written:

$$
E_{R3c}(d_{BFO}) = u_{R3c} \cdot t_{BFO} + E_{es} \quad , \tag{3.10}
$$

where u_{R3c} is the strain energy density.

Note that the total energy of Pnma(1) only contains the strain term as no polar discontinuity is involved and can be expressed as:

$$
E_{Pnma(1)}(d_{BFO}) = u_{Pnma(1)} \cdot t_{BFO} \quad . \tag{3.11}
$$

Finally we assume that the polarisation remains uniform and constant throughout the whole BFO film. In Fig. 15 we plot the energies of both phases as a function of t_{BFO}. We see that due to the electrostatic energy the R3c is unfavourable relative to the $Pnma$ for low thicknesses. This can easily be understood by remembering that the internal energy scales with the volume of the film while the electrostatic energy cost is related to the surface charges. It becomes then clear that at larger thicknesses (larger volume) the strain energy becomes more important and we find that at around 14 nm, there is a crossover between R3c and $Pnma(1)$.

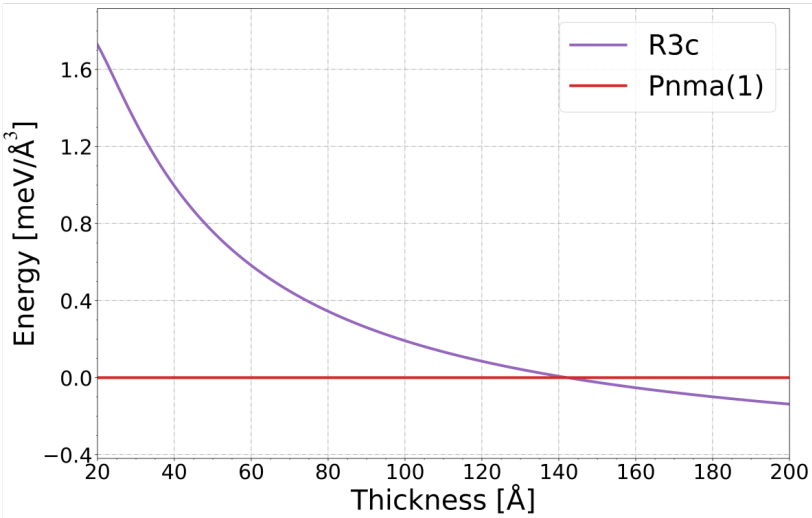

Figure 15: Internal and electrostatic energy. We plot the total energy density per volume for the R3c and $Pnma(1)$ phases according to equations 3.8 and 3.11 with $\epsilon_r = 55$ [78], $E_g = 2$ eV, $P = 60$ μC/cm^2 and the values for the internal energy of both phases are taken from Fig. 14b.

3.5 THICKNESS, STRAIN AND DIELECTRIC CONSTANT

While it is well established that strain can be used to stabilise new phases, we showed that electrostatics can also play a major role and stabilise a non-polar phase in BFO. In the case of a material such as BFO with a polar ground state, we showed that one can use the two control parameters that are thickness and strain in order to stabilise another phase that is centrosymmetric (non-polar).

In the derivation above we assume that the electron-hole pairs are created within the BFO layer and we saw that the screening cost is directly related to the permittivity and band gap energy. Let us be more general now and assume that the same screening mechanism can happen either in the ferroelectric film, or in the dielectric material. The latter option is likely to happen if the dielectric constant of the surrounding material is higher than that of the ferroelectric material. This provides a third control parameter given by the dielectric constant of the surrounding material. Note that for simplicity we consider in what follows that the band gap energy is fixed and equal to 2 eV.

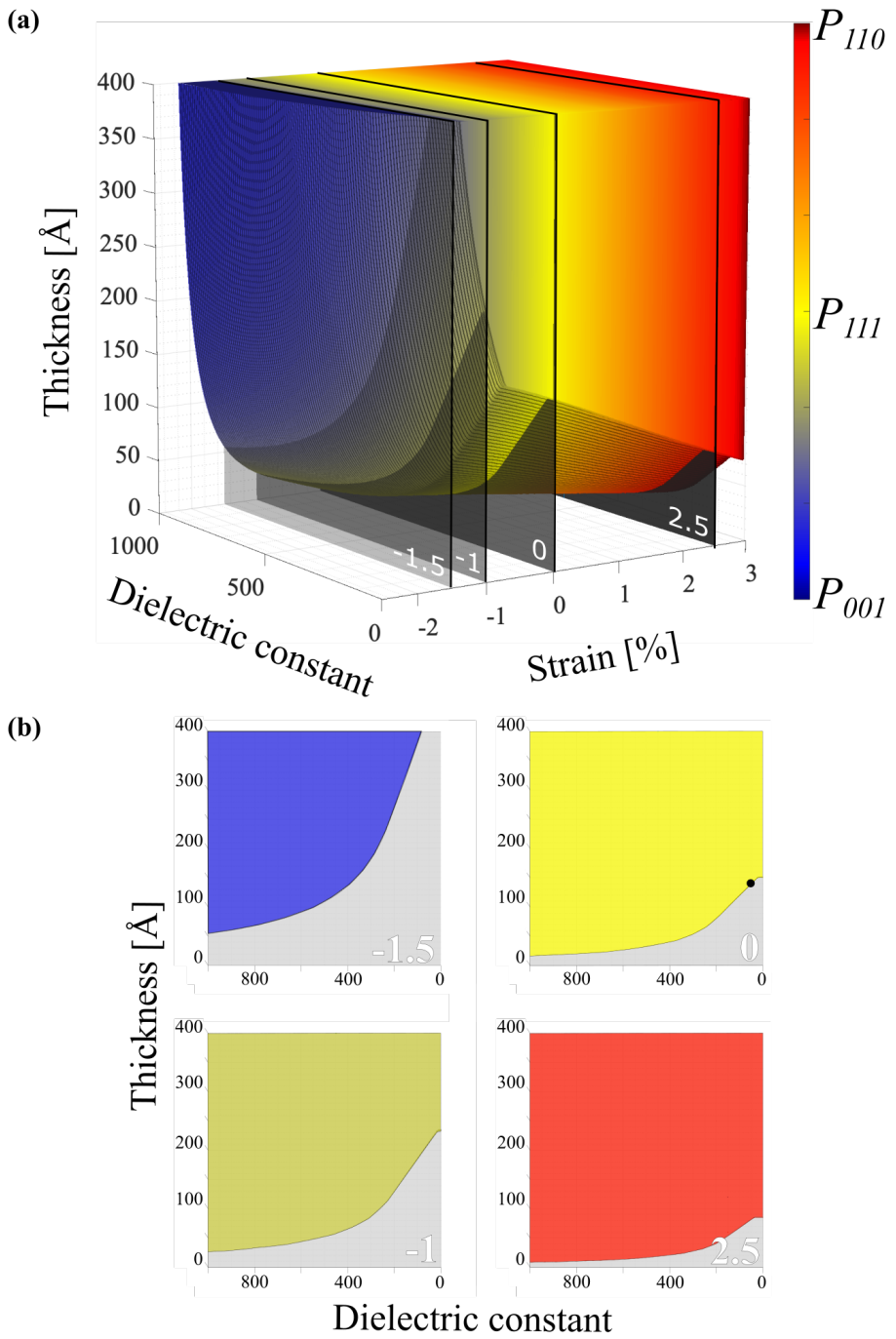

Figure 16: (a) Three-dimensional phase diagram of the polar versus non polar regions as a function of strain, dielectric constant of the surrounding material and thickness of BFO. The polar region is represented by the coloured volume and the non-polar one by void space regions. The polar volume is coloured according to the orientation of the polarisation vector. We intersect the volume with perpendicular planes at different fixed strains further displayed in (b). (b) Thickness versus dielectric constant for different strain values, in which the grey zones represent the non-polar region and the coloured zones the polar one (colours are consistent with the orientation of the polar vector). The black dot in the top right panel represents the critical thickness at which there is a crossover between R3c and $Pnma(1)$ in Fig. 15.

In order to understand the stability of a non-polar phase over the R3c ground state, we construct a three-dimensional phase diagram in which the axes are given by the strain imposed by the substrate, the dielectric constant of the surrounding material and the thickness of the BFO film. For each coordinate we compare the energy of the lowest energy polar phase and the lowest energy non-polar phase and mark the corresponding position in the phase space as polar or non-polar according to which has the lowest energy.

We consider the effect of strain by fitting the strain energy on the curve displayed in Fig. 14, and taking the lowest energy value for the non-polar case. We also account for the strain-polarisation coupling by assuming that the out-of-plane component of the polarisation varies linearly between 45 $\mu C/cm^2$ (at 4% of tensile strain) to 75 $\mu C/cm^2$ (at 4% of compressive strain) based on previous studies [41, 79]. The electrostatic energy as a function of ε and t is computed according to equation 3.9. For generality we evaluate the electrostatic energy cost within the BFO layer as well as within the dielectric layer and consider the lowest value.

In Fig. 16a we present the three-dimensional phase diagram, with the polar region represented by the coloured volume and the non-polar region by the void. In Fig. 16b, we present the projections on the intersecting planes of Fig. 16a, with the polar and non-polar regions displayed on the thickness-dielectric constant subspace for different strain values.

We observe that the polar regions are favoured by tensile strain, as the out-of-plane component of the polarisation decreases and so does the electrostatic energy cost. The thickness also plays a crucial role as for all strains considered, the polar phase becomes stable at large thicknesses. Intuitively it makes sense as for very large thickness, one expects to recover the bulk behaviour. Finally, we can see that increasing dielectric constant is accompanied by decreasing critical thickness and the former is particularly crucial at small thicknesses where one can stabilise a non-polar phase by decreasing the dielectric constant of the surrounding material (choosing an appropriate material).

3.6 ANTI-POLAR OR ANTIFERROELECTRIC?

We showed that the phase observed experimentally has $Pnma$ symmetry with anti-polar distortions described by the Λ_3 and Σ_2 modes (Fig. 12) in absence of the ground state polar mode (Γ_4^-). Consequently, BFO in this phase is not ferroelectric. The question that we address here is: does ferroelectricity disappear at the benefit of another interesting property arising from the new structure: antiferroelectricity.

Antiferroelectricity was first predicted by Kittel in 1951 [80] and observed in $PbZrO_3$ a few months later [81, 82]. According to the first definition given by Kittel, "an antiferroelectric state is defined as one in which lines of ions in the crystal are spontaneously polarized, but with neighboring lines polarized in antiparallel directions" [80]. This definition places ferroelectric and antifer-

roelectric materials on a similar ground, in that ferroelectricity correlates with polar distortions and antiferroelectricity with anti-polar distortions. It is, nevertheless, not the case that all non-polar materials with anti-polar distortions are antiferroelectric. Additionally, there should be a relatively low-energy ferroelectric phase obtained through polar distortion of a common high-symmetry reference structure. Furthermore, there should exist a first-order phase transition from the antiferroelectric phase to the ferroelectric one under applied electric field (smaller than the breakdown field) [83] which results in the characteristic hysteresis loop presented in Fig. 17.

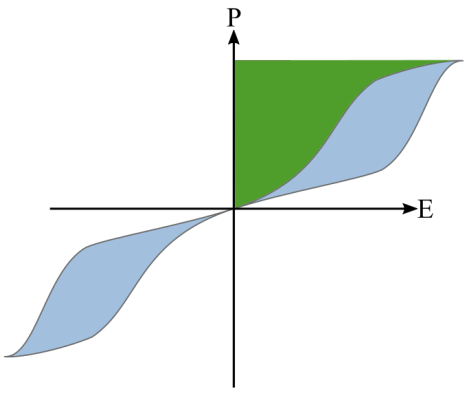

Figure 17: Characteristic hysteresis loop of an antiferroelectric material. At low applied electric field, there is a linear response of P to E, followed by a transition to a ferroelectric state at larger fields. The green area represents the recoverable energy density, equivalent to the energy stored in the system.

The energy stored per unit volume (J) in a dielectric material (see Fig. 17) can be calculated by [84]:

$$J = \int_0^{E_{max}} \epsilon E dE \quad , \tag{3.12}$$

where E_{max} is the highest possible field that can be applied before breakdown, ϵ the permittivity and E the electric field. Compared to ferroelectric materials, antiferroelectrics have a higher energy storage density, which makes them particularly interesting for energy-efficient technologies.

While $Pnma(1)$ is not the true ground state of BFO, we showed that under specific electrostatic boundary conditions it can become the lowest energy phase. The question that remains now to be answered is whether or not one can go from $Pnma(1)$ to a polar phase by applying an electric field smaller than the breakdown field.

When an electric field ($\mathbf{E}$) is applied to the sample, it couples with the polarisation and creates an energy given by $-\mathbf{P} \cdot \mathbf{E}$. If this energy term is larger than the energy barrier necessary to transition from the anti-polar to polar state, the

structure experiences a phase transition toward the polar phase. Let us assume that the polar phase is R3c and let us compute the energy barrier in order to estimate the required electric field corresponding.

In order to estimate the energy barrier, we want to determine the minimum energy path between Pnma(1) and R3c. To do so we use the so-called nudged elastic band (NEB) method [85–87]. This method consists in finding the minimum energy path between given initial and final states. The images created along the path are bonded together with fictional springs and relaxed under the constraint imposed by the springs. We generate a set of intermediate states by linear interpolation between Pnma(1) and R3c and we run the NEB algorithm until forces are below 0.05 eV/Å. We obtain an energy barrier of 26 meV/f.u. (see Fig. 18a) and deduce that to overcome this activation energy one needs to apply an electric field of 1.16 MV/cm which is lower than the electrical breakdown voltage of 2.7 MV/cm reported experimentally [55]. It seems then reasonable to expect that there exists an experimentally-accessible transition path from Pnma(1) to R3c. The transition between antipolar to polar is also illustrated by the evolution of the Λ_3 and Σ_2 modes and of the Γ_4^- mode (polar mode in R3c), where the former decrease while the latter increases along the transition path (see Fig. 18b). Note that the fluctuations in the curves are related to the precision of our calculations. We would probably obtain smoother curves by increasing the precision.

From a theoretical point of view, we can then conclude that BFO in the Pnma(1) is likely to be an antiferroelectric material with interesting energy-storage related properties.

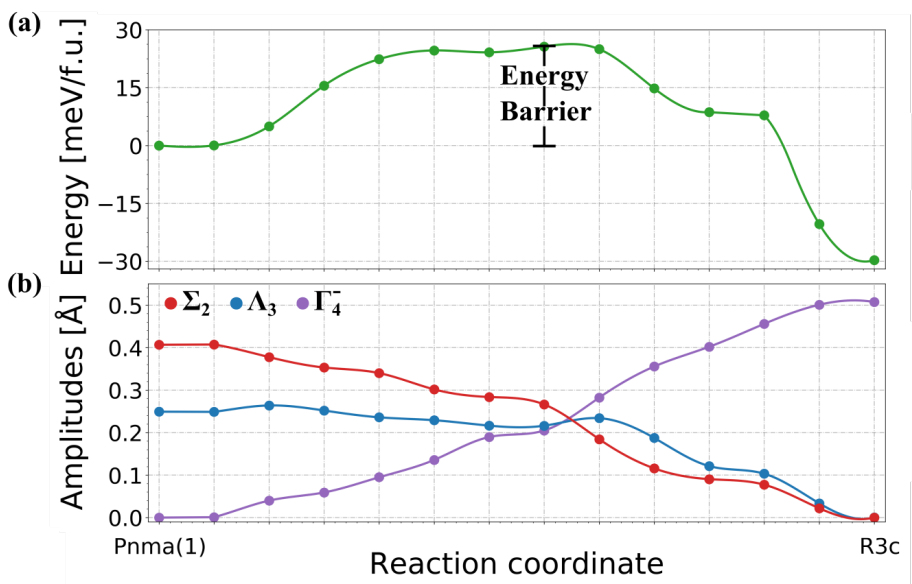

Figure 18: (a) Computed energy along the minimum energy path (MEP) between Pnma(1) and R3c. (b) Evolution of amplitudes of the polar and antipolar modes along the MEP.

Magnetic ordering	I	2_z	2_y	2_x	$-I$	m_z	m_y	m_x	
G_x	+1	+1	+1	+1	+1	+1	+1	+1	A_g
G_y, F_z	+1	+1	-1	-1	+1	+1	-1	-1	B_{1g}
F_y, G_z	+1	-1	+1	-1	+1	-1	+1	-1	B_{2g}
F_x	+1	-1	-1	+1	+1	-1	-1	+1	B_{3g}
A_x, C_z	+1	+1	-1	-1	-1	-1	+1	+1	B_{1u}
A_y	+1	+1	+1	+1	-1	-1	-1	-1	A_u
C_y	+1	-1	+1	-1	-1	+1	-1	+1	B_{2u}
C_x, A_z	+1	-1	-1	+1	-1	+1	+1	-1	B_{3u}

Table 1: Character table for point group D_{2h}. We gather together the magnetic orderings that transform in the same way under all symmetry operations of the group. The result of each symmetry operation is labeled $+1$ if it leaves the magnetic ordering unchanged or -1 if it reverses it. Note that we orientate z along $[001]_{pc}$.

3.7 MAGNETIC ORDERING OF $Pnma(1)$

We saw in section 1.5.2 that while BFO is AFM G-type in its ground state, there is a small spin canting perpendicular to the antiferromagnetic direction resulting in a weak ferromagnetism. This canting happens because the coupling between G-type AFM and the FM ordering in a perpendicular direction is invariant by symmetry. $Pnma(1)$ is also G-type, and here we address the possibility of weak ferromagnetism in this phase. Before considering non-collinear DFT calculations, let us first tackle the problem using group theory in order to identify the possible magnetic orderings allowed to coexist by symmetry.

We consider the point group D_{2h} (point group of $Pnma(1)$) and account for four possible magnetic orderings: F for ferromagnetic ordering, A-type AFM ordering (FM in the (001) plane and AFM perpendicular to it), C-type AFM ordering (FM in the (111) plane and AFM perpendicular to it) and finally G-type. Because of the non-collinearity we also need to consider the three cartesian directions x, y and z for each magnetic moment. We then have 12 possible states for the spins: $F_x, F_y, F_z, A_x, A_y, A_z$, C_x, C_y, C_z, G_x, G_y and G_z. In order to determine the symmetry invariant couplings, one needs to apply the symmetry operations from the D_{2h} point group to each non-collinear magnetic order and evaluate the way that they transform[4]. The results of these operations are presented in Table 1.

We see from Table 1 that different magnetic orderings share the same character table, which means that if one is stable the other one can also be stable without changing the symmetry. In particular we are interested in the cases where G appears and we see that if G_y or G_z are stable, F_z or respectively F_y can appear also. This means that weak ferromagnetism is allowed by symmetry

[4]Note that the magnetic moments are axial vectors.

in these cases. We can also see that G_x does not share its character table with another order meaning that if the moments in the G-type order are orientated along x, no canting is allowed.

While we saw that in two cases, symmetry allows weak ferromagnetism, the amplitude of the canted moment depends on the coupling of $G_y \cdot F_z$ and $G_z \cdot F_y$. On the other hand if G_x is the lowest energy configuration, no canting will happen. To verify this and to determine the stable magnetic orderings, we need to rely on non-collinear DFT calculations including spin-orbit coupling. We find that the lowest-energy ordering is G_y and the highest is G_x. Non-collinear calculations also confirm the results of Table 1 as we find no canting when spins are initialised along x and we find small canting along y or z resulting in a total magnetisation of around 0.3 μ_B when spins are initialised along z or y respectively.

3.8 CONCLUSION

In this chapter, we identified a new phase with $Pnma$ symmetry that matches recent experimental observations of new structures in the BFO layers of LBFO/BFO superlattices. This phase has a larger unit cell (80 atoms) and contains antipolar distortions along two perpendicular directions caused by the presence of antipolar distortion modes (Σ_2 and Λ_3). We studied the stability of this phase and showed that while strain is not sufficient to explain its presence in the LBFO/BFO superlattices, the electrostatic energy is a key factor. We showed by simple electrostatic considerations that the new antipolar phase of BFO is more favourable at small thicknesses and the ground state can be recovered by increasing the thickness of the film. We also studied the electric and magnetic properties emerging from this phase and concluded that BFO in the $Pnma(1)$ phase is likely antiferroelectric and displays weak ferromagnetism.

To generalise our results on electrostatic engineering of non-polar phases we constructed a three-dimensional phase space based on our calculations. We found that by appropriate choices of strain through the choice of substrate, electrostatic boundary conditions through the choice of surrounding material (according to its permittivity) and thickness of the film grown, one can stabilise the $Pnma(1)$ phase in BFO in superlattices with other materials. In principle, we believe that this route for stabilising non-polar phases could be applied to other materials than BFO under the following requirements:

- The material chosen should be polar in its ground state and a relatively low energy non-polar phase should exist
- There should be a large polar discontinuity in the superlattice
- The material surrounding the polar material should have a relatively low dielectric constant in order to disfavour the screening of the bound charges

To conclude, let us briefly discuss different elements that were not considered in our modelling. Regarding the electrostatic model, we constrained the system

to be single domain. We found that below a critical thickness, $Pnma(1)$ is stable and above it R3c is recovered. While multi-domains are beyond the scope of our work, we anticipate that domains could likely form at lower critical thickness and be energetically more favourable than the screening mechanism that we described.

Another aspect that we did not consider is the influence of the octahedral mismatch at the interface. If different polymorphs have very different tilt or rotation angles, this contribution is likely to favour one over the other and could be considered as a fourth control parameter in a more general model. An approach to model this influence could be to constrain the octahedra of the different polymorphs in competition with those of the surrounding material and account for the energy penalty.

Exploring the Phase Space with Phonons

4

Motivated by the discovery of a structure with large unit cell and interesting properties in the previous chapter, we explore systematically here the phase space of BFO in search of other phases. Having a good understanding of the phase space of BFO can provide insights for future experimental work.

A convenient way to stabilise metastable phases is by growing materials as thin films in superlattices or heterostructures, where the interactions with other materials as well as the limitation in size can contribute to destabilising the bulk ground state. We saw for instance in the previous chapter that BFO, which is normally ferroelectric in its ground state, can become antiferroelectric under suitable conditions provided by the strain and the electrostatic boundary conditions.

While previous studies restricted their search for metastable phases to 40-atom unit cells, we see in the light of chapter 3 that it might be necessary to consider larger unit cells in order to identify other metastable phases. In order to look for new phases, we adopt a systematic approach in which we start from existing structures and look for unstable (non-)zone-center phonon modes that indicate structural instabilities. Once an instability is found we identify the corresponding metastable phase by fully relaxing the structure in which the unstable distortion mode was added. Additionally to the $Pnma(1)$ phase, we identify other centrosymmetric phases with similar unit-cell size, as well as series of non-centrosymmetric phases displaying polar and antipolar distortions along perpendicular directions. We also discuss their experimental stability with respect to strain and electrostatics using the model developed in the previous chapter (see section 3.4.2). This work is published as *"Prediction of low-energy phases of $BiFeO_3$ with large unit cells and complex tilts beyond Glazer notation"* in Phys. Rev. Materials, see Ref. [88] (Copyright 2021 by the American Physical Society).

The remainder of this chapter is organised as follows. First, we review different polymorphs of BFO that have been previously predicted or observed to be stable under strain. Second, we present a previous systematic study of the phase space of BFO [58] and underline the differences with our current work. We then present our thorough exploration of phases with larger unit cell through the publication mentioned above. Finally, we complete the study by presenting other structures not included in Ref. [88] and conclude the chapter.

4.1 REVIEW OF PREVIOUSLY IDENTIFIED PHASES

While this section only presents a small portion of the published works, we show here a selection of tetragonal, monoclinic and orthorhombic structures reported for BFO. We start by reviewing metastable phases predicted to be stable under strain and finish by an extensive work searching for metastable phases.

Compressive strain is of particular interest as it is known to enhance the out-of-plane spontaneous polarisation of ferroelectric thin films. Starting at very large strain values and going towards zero strain, different phases have been reported, from a tetragonal structure with $P4mm$ symmetry accompanied by a very large c/a ratio, to monoclinic versions with Pm and Cc symmetries respectively [40, 41, 89–91].

Tensile strain has also been investigated. Dupé et al. reported, in theoretical study, that between 0% and 8% of strain, the polarisation, tilt axis and magnetisation axis rotate with increasing strain. They predicted a phase transition between Cc and $Ima2$ at around 8% [92]. Yang et al. predicted the stability of another orthorhombic phase with $Pmc2_1$ symmetry, for tensile strains above 5% [93], lower in energy than the Cc and $Ima2$ phases previously reported. The existence of an orthorhombic phase was confirmed experimentally by Yang[1] et al., for a strain magnitude higher than 2.2% [94].

From these examples, one can see that strain alone can already stabilise several phases over the ground state, suggesting that many low energy metastable phases exist for BFO. To address this question, Diéguez et al. performed a systematic search of metastable phases using first-principles methods [58]. Their approach consisted of considering several starting structures containing 40 atoms ($2 \times 2 \times 2$ cubic unit cells) and relaxing them with DFT, after breaking the symmetries by running a short molecular dynamics simulation beforehand. The starting structures were created by considering the usual crystal systems combined with distortions found in perovskites such as in-phase and antiphase Glazer rotations, polar and antipolar distortions of the Bi cations as well as changes of the crystal system from cubic to tetragonal or orthorhombic. With this procedure, they identified different phases whose theoretical stability was further tested using different functionals (LDA, PBE and PBEsol).

While this approach provides an important understanding of the phase space of BFO, it only accounts for phases with at most 40 atoms per unit cell in the cubic setting ($2 \times 2 \times 2$ cubic system). It fails to capture the $Pbam$ or $Pnma(1)$ phases presented in the previous chapter for example. In the next section we propose an extension of the study by Diéguez et al., where we look for metastable phases with larger unit cells using phonon instabilities and add to the strain considerations, the effect of electrostatics boundary conditions.

4.2 PEER REVIEWED WORK

[1] Note that the first authors in Ref. [93] and [94] are not the same person.

PHYSICAL REVIEW MATERIALS **5**, 054403 (2021)

Prediction of low-energy phases of $BiFeO_3$ with large unit cells and complex tilts beyond Glazer notation

Bastien F. Grosso* and Nicola A. Spaldin
Materials Theory, ETH Zürich, Wolfgang-Pauli-Strasse 27, 8093 Zürich, Switzerland

(Received 3 March 2021; accepted 21 April 2021; published 7 May 2021)

We use density functional theory to identify several previously unknown polar and nonpolar structures within the low-energy phase space of perovskite-structure bismuth ferrite, $BiFeO_3$. Bismuth ferrite is one of the most widely studied multiferroic materials because of its large ferroelectric polarization coexisting with magnetic order at room temperature. Of particular interest is a series of noncentrosymmetric structures with polarization along one lattice vector, combined with antipolar distortions, reminiscent of ferroelectric domains, along a perpendicular direction. We discuss possible routes to stabilising the new phases using biaxial heteroepitaxial strain or interfacial electrostatic control in heterostructures.

DOI: 10.1103/PhysRevMaterials.5.054403

I. INTRODUCTION

Bismuth ferrite, $BiFeO_3$, is one of the few materials that combines magnetic order and ferroelectricity in the same phase at room temperature, making it one of the most well-studied multiferroics. The structural ground state of $BiFeO_3$ is a distorted $R3c$-symmetry perovskite, with antiferrodistortive rotations of the oxygen octahedra around the pseudocubic [111] axis, combined with a large polarization ($\sim$90 μC/cm^2) along the [111] direction caused by the $6s^2$ lone pairs of electrons on the Bi^{3+} ions [1]. The strong superexchange between the Fe^{3+} $3d^5$ electrons gives robust antiferromagnetism.

While the $R3c$ structural ground state is both theoretically [1] and experimentally [2] well established, the low-energy structural phase space of $BiFeO_3$ is known to be very rich. Under compressive strain imposed by coherent heteroepitaxy, polar monoclinic, tetragonal-like, and tetragonal structures can be stabilized [3–6], whereas under tensile strain or hydrostatic pressure it adopts a polar orthorhombic structure [7–9]. More recently, heteroepitaxy has been exploited to form antipolar phases of $BiFeO_3$ in superlattices with $La_{0.7}Sr_{0.3}MnO_3$ [10] and $La_{0.4}Bi_{0.6}FeO_3$ [11], where the stability of the antipolar phase was attributed to magnetic coupling and control of the electrostatic boundary conditions, respectively. Furthermore, a systematic density functional theory (DFT) study revealed a large number of low-energy metastable structures within unit cells up to a size of 40 atoms [12].

Motivated in particular by the recent observation of ultralarge unit cell phases in thin film heterostructures [11], we present a detailed computational study of the low-energy structural phase space of $BiFeO_3$, with a focus on large unit cell structures. Our approach is to start from the previously identified phases of Ref. [12] and search for unstable non-zone-center phonon modes that indicate structural instabilities. We then increase the unit cell size to accommodate the corresponding energy lowering structural distortion. With this approach, we find that the apparent metastability of many of the previously identified structures, for example, *Pbam* and $Pmc2_1$, was an artifact of the 40-atom unit cell size, and in fact their energy is lowered by large period structural distortions. Finally, we demonstrate how these new phases can be stabilized relative to the bulk $R3c$ ground state through careful engineering of the electrostatic and strain boundary conditions, facilitating the rational design of $BiFeO_3$-based heterostructures with new functionalities.

The remainder of this paper is organized as follows. In Sec. II, we present the technical details of the simulations and introduce a generalization to the standard Glazer notation [13], that allows the description of more complex oxygen octahedral tilt patterns. In Sec. III A, we present the new phases that we identify in this work and describe their structures in terms of their main distortion modes. In Sec. III B, we consider a series of structures obtained by increasing the unit cell length along one direction and compare this series of structures with the formation of domains. In Sec. IV, we study the possible stabilization of the new phases using strain or control of the electrostatic boundary conditions. Finally, in Sec. V, we summarize our study.

II. METHODS

A. Computational details

The calculations were performed using DFT [14] with the projector augmented wave (PAW) method [15] as implemented in the Vienna *ab initio* simulation package (VASP 5.4.4) [16]. We used a 12x12x12 k-point Γ-centered mesh to sample the Brillouin zone corresponding to a five-atom unit cell, and chose an energy cutoff of 850 eV for the plane-wave basis. The following valence electron configurations were used[1]: $5d^{10}6s^26p^3$ for bismuth, $3p^63d^74s^1$ for

*Corresponding author: bastien.grosso@mat.ethz.ch

[1]The Bi, Fe, and O PAWs are dated respectively from April 8 2002, September 6 2000, and April 8 2002.

 ©2021 American Physical Society

iron, and $2s^2 2p^4$ for oxygen. We used the PBEsol + U functional form of the generalized gradient approximation [17], with a commonly used value of $U_{\text{eff}} = 4$ eV for the Fe $3d$ orbitals [18,19], according to Dudarev's approach [20]. Note that the results presented here are not sensitive to the choice of U within a reasonable range [19], and that our choice of exchange-correlation functional has been shown to give good results for $BiFeO_3$ compared with more computationally expensive hybrid functionals, which are prohibitive for the large unit cells studied here [21].

B. Phonons and symmetry

In order to identify new metastable phases, we start from the following experimentally stabilized, or computationally predicted polymorphs of $BiFeO_3$: $Pmc2_1$ (20 atoms/unit cell (u.c.)), *Pbam* (40 atoms/u.c.), and *Pnma* (20 atoms/u.c.) [7,9,22] and explore the phonon instabilities along various reciprocal directions. We use the frozen-phonon method, as implemented in the PHONOPY package [23] to look for imaginary phonon frequencies at selected symmetry points corresponding to supercells up to 160 atoms per unit cell. In practice, for a given starting phase, we construct supercells within our limit on the number of atoms and compute the zone-center phonon frequencies to look for instabilities. Once an instability is found, we freeze the distortions given by the eigenvector corresponding to that imaginary frequency and fully relax the structure; if this procedure identifies a new (meta)stable phase, we repeat the procedure on that phase iteratively. We restrict our subsequent analysis to metastable phases with an energy up to 100 meV/f.u. above the $R3c$ ground state. For the large structures (80 atoms per unit cell or larger) we assess metastability by computing only the zone-center phonons and specify below the cases where a zone-center instability remains. We analyze each fully relaxed structure to determine the combination of phonon modes that contribute to its structural distortion from the reference cubic perovskite structure, using the ISODISTORT [24,25], AMPLIMODES [26,27], and PYMATGEN [28] packages.

C. Born effective charges and polarization

Since Berry phase calculations of the polarization are prohibitively expensive for very large unit cells, we compute polarizations by summing the displacements of the ions from a high-symmetry nonpolar parent structure multiplied by their Born effective charges. We use an averaged Born effective charge per atom type obtained from averaging over the tensor components for 15 structures, including all phases presented in this work with 80-atom unit cells or less and other higher energy phases, computed in this work but not reported, to obtain one isotropic value per atom species. This procedure results in the following values: 4.86 [e] for Bi, 3.99 [e] for Fe, and −2.95 [e] for O in units of the electronic charge magnitude, consistent with the values reported in the literature [18].

D. Extended Glazer notation for complex tilting

Glazer introduced a convenient and widely used method for describing octahedral tilting in perovskites [13], which consists of a letter (a, b, or c) indicating whether the tilting along each of the cartesian directions is the same or different and a superscript +, − or 0, to indicate whether the relative tilts between consecutive octahedra are the same, opposite or zero about the respective axis. This notation is restricted to tilt patterns with wave vectors $k = 0$ or $\frac{\pi}{a}$, where a is the lattice vector along the considered direction. More complicated tiltings, not captured by the current Glazer notation have been reported [29,30] and are prevalent in this work. We propose the following extension to Glazer notation suitable for generic tilting: we retain the a, b and c notation referring to each lattice vector, but we replace the +, − or 0 superscripts by a series of Greek letters ($\alpha, \beta, \gamma, \dots$) indicating the magnitude of rotation of each octahedron around the pseudocubic direction considered. An overline then indicates clockwise rotations, no overline indicates anticlockwise and a $\emptyset$ no rotation. The number of superscripts indicates the number of octahedra in the periodic repeat unit and letters are repeated in the series if the rotation amplitudes of different octahedra are equal. If the exact same sequence of amplitudes of the tilts is observed along different directions, the a or b are repeated along with the series of superscripts. Due to the periodicity of these series in a crystal, there are multiple ways to write the same sequence; we make the choice to always start the sequence by a clockwise rotation, if there is one.

For simple tilt patterns, the connection between the traditional Glazer notation and the extended Glazer notation can be easily made, for example,

$$\begin{aligned} Pnma \quad & a^-a^-c^+ \Longleftrightarrow a^{\bar{\alpha}\alpha}\, a^{\bar{\alpha}\alpha}\, c^{\bar{\alpha}\bar{\alpha}}, \\ R3c \quad & a^-a^-a^- \Longleftrightarrow a^{\bar{\alpha}\alpha}\, a^{\bar{\alpha}\alpha}\, a^{\bar{\alpha}\alpha}, \\ Immm \quad & a^0b^+c^+ \Longleftrightarrow a^{\emptyset}\, b^{\bar{\alpha}\bar{\alpha}}\, c^{\bar{\alpha}\bar{\alpha}}, \\ Pm\bar{3}m \quad & a^0a^0a^0 \Longleftrightarrow a^{\emptyset}\, a^{\emptyset}\, a^{\emptyset}. \end{aligned}$$

In this case, the extended notation offers no advantage over the traditional one. For more complicated tilts, with different amplitudes or complex sequences, it provides a convenient notation. For example, a tilting characterized along two directions by a wave vector of $\frac{\pi}{4a}$, with two octahedra tilted in one direction (with the same amplitude), the next pair tilted in the opposite direction with a different tilting angle from the first pair (and with different amplitudes within the pair) and a simple opposite tilting (with the same amplitude) along the third direction is written $a^{\bar{\alpha}\bar{\alpha}\beta\gamma}a^{\bar{\alpha}\bar{\alpha}\beta\gamma}c^{\bar{\alpha}\alpha}$ in this notation. Notice that one could use different Greek letters along different directions to signal different (or similar) rotational amplitudes if this extra information were of interest, but we make the choice not to distinguish the amplitudes along different directions.

We report the tilt patterns for the phases that were identified in this study, using this extended notation in Table II.

III. RESULTS

A. Phases and distortions

We now follow the procedure described in Sec. II to identify various new polymorphs of $BiFeO_3$. We extend previous studies [31], by exploring unit cells up to 160 atoms in size, and of variable shape; this allows us to incorporate phonon

TABLE I. Computed lattice parameters, energy compared to the ground state, band gap energy and polarization for newly identified structures within 100 meV of the $R3c$ ground state (upper part of the table) and previously reported phases with 40 atoms or less [12], which we recomputed here with our simulation parameters (bottom part of the table). In all new cases the calculated angles between the lattice vectors are equal or very close to 90°. The lattice parameter value in italics indicates the axis along the cartesian z axis; we refer to this as the out-of-plane axis in the context of our later discussion of thin film heterostructures. The polarization is computed by summing over an average value of the Born effective charge for each ion multiplied by its displacement from its position in the high-symmetry reference structure. We show the values for the ground-state $R3c$ (in the hexagonal setting, in which the c axis corresponds to the $[111]_{pc}$ direction) and for the high-temperature *Pnma* structures as well as for the phases from Ref. [12] for reference. Note that the previously reported structures are stable with C-type antiferromagnetism (along the stretched lattice vector) and that we don't report the previously reported $Pna2_1$ phase since it always relaxed to the *Pnma* in our simulations. The structures and energies are in good agreement with the original results from Ref. [12] but we find higher values for the polarization along the long axis and lower values along the short axes. We attribute this difference to our isotropic approximation for the Born effective charges.

	Lattice parameters			Energies		Polarization		
Phase	a (Å)	b (Å)	c (Å)	Energy (meV/f.u.)	Band gap (eV)	P_a (μC/cm^2)	P_b (μC/cm^2)	P_c (μC/cm^2)
$Pmc2_1$ (2)	*7.79*	11.11	5.56	76	2.119	0	0	76.1
Pnma (2)	5.57	*15.43*	11.22	70	2.296	-	-	-
$P2_1/c$	*7.75*	11.19	5.57	46	2.205	-	-	-
$Cmc2_1$	*15.67*	11.01	5.54	36	1.993	0	0	31.7
Pnma (1)	5.53	*15.65*	11.16	35	2.108	-	-	-
$Pmc2_1$ (1)	*15.60*	10.93	5.58	32	1.959	0	0	16.0
Pc (1)	*15.74*	5.48	5.58	23	2.055	54.4	0	39.8
$R3c$ (hexag.)	5.54	5.54	*13.72*	0	2.141	0	0	*100.4*
Pnma	5.63	*7.73*	5.40	21	1.825	-	-	-
Cc-C	7.50	7.50	*9.41*	102	1.944	25.2	25.2	166.2
Cm-C	7.36	7.57	*9.51*	108	1.921	0	41	171.4
Pc-C	7.47	7.47	*9.47*	114	2.048	27	27	167

instabilities at lower symmetry q points in the Brillouin zone for larger primitive unit cells than were previously studied.

In Table I, we show the list of newly identified phases (along with the lowest energy phases reported in [12]) that have an energy difference of less than 100 meV/f.u. from the $R3c$ ground state, and report the lattice parameters, energy relative to the ground state, band gap and polarization along each lattice vector for each case. In Table II, we decompose each phase into its main irreducible distortion modes and report its tilting pattern in terms of the traditional Glazer notation when possible and in terms of the extended notation introduced earlier (all cases). For reference, we include the ground state ($R3c$) and the lowest energy nonpolar (*Pnma*) phase in both tables. In Fig. 1, we present the unit cells of the five lowest energy new phases, and in Fig. 2, the dominant distortion modes that make up the structures, with the main contributions to the distortions highlighted by arrows.

TABLE II. Dominant structural distortions and octahedral tilt patterns for the newly identified low-energy phases. The distortion modes are reported with respect to the ideal cubic perovskite structure ($Pm\bar{3}m$) in all cases. We separate the modes into three categories: polar, antipolar, or rotational/tilting, and we only report the modes contributing to at least 4% of the total distortion for each structure. An exception is made for the Polar modes, which are always reported to distinguish between polar and nonpolar phases. The octahedral tilt patterns are given in terms of the traditional Glazer notation where possible, and the extended notation for all cases. We align the out-of-plane axis reported in Table I with the third axis in the Glazer notation.

	Main structural distortions			Octahedral tilts			
Phase	Polar modes	Antipolar modes	Rotational/Tilting modes	Glazer	Extended Glazer notation		
$Pmc2_1$ (2)	Γ_4^-	Σ_2, S_1	R_5^-, M_2^+	-	$a^{\tilde{\alpha}\beta\tilde{\gamma}\delta}$	$a^{\tilde{\alpha}\beta\tilde{\gamma}\delta}$	$c^{\tilde{\alpha}\tilde{\alpha}}$
Pnma (2)	-	Σ_2, S_2	R_5^-, T_2	-	$a^{\tilde{\alpha}\beta\tilde{\gamma}\delta}$	$a^{\tilde{\alpha}\beta\tilde{\gamma}\delta}$	$c^{\tilde{\alpha}\tilde{\alpha}\beta\beta}$
$P2_1/c$	-	Σ_2, Σ_3, S_2	R_5^-	-	$a^{\tilde{\alpha}\beta\tilde{\gamma}\delta}$	$a^{\tilde{\alpha}\beta\tilde{\gamma}\delta}$	$c^{\tilde{\alpha}\beta}$
$Cmc2_1$	Γ_4^-	Λ_3, X_5^-	R_5^-, M_2^+	-	$a^{\tilde{\alpha}\beta\tilde{\gamma}\delta}$	$a^{\tilde{\alpha}\beta\tilde{\gamma}\delta}$	$c^{\tilde{\alpha}\tilde{\beta}\tilde{\beta}\tilde{\alpha}}$
Pnma (1)	-	Σ_2, Λ_3, S_2	R_5^-, T_2	-	$a^{\tilde{\alpha}\beta\tilde{\gamma}\delta}$	$a^{\tilde{\alpha}\beta\tilde{\gamma}\delta}$	$c^{\tilde{\alpha}\tilde{\alpha}\beta\beta}$
$Pmc2_1$ (1)	Γ_4^-	$\Lambda_3, \Delta_5, X_5^-, \Sigma_2$	R_5^-, M_2^+	-	$a^{\tilde{\alpha}\beta\tilde{\gamma}\delta}$	$a^{\tilde{\alpha}\beta\tilde{\gamma}\delta}$	$c^{\tilde{\alpha}\tilde{\beta}\tilde{\beta}\tilde{\alpha}}$
Pc (1)	Γ_4^-	Δ_5, X_5^-	R_5^-, M_2^+, T_2	-	$a^{\tilde{\alpha}\beta}$	$a^{\tilde{\alpha}\beta}$	$c^{\tilde{\alpha}\beta\tilde{\gamma}\tilde{\delta}}$
Pnma	-	X_5^-	R_5^-, M_2^+	$a^-a^-c^+$	$a^{\tilde{\alpha}\alpha}$	$a^{\tilde{\alpha}\alpha}$	$c^{\tilde{\alpha}\tilde{\alpha}}$
$R3c$	Γ_4^-	-	R_5^-	$a^-a^-a^-$	$a^{\tilde{\alpha}\alpha}$	$a^{\tilde{\alpha}\alpha}$	$a^{\tilde{\alpha}\alpha}$

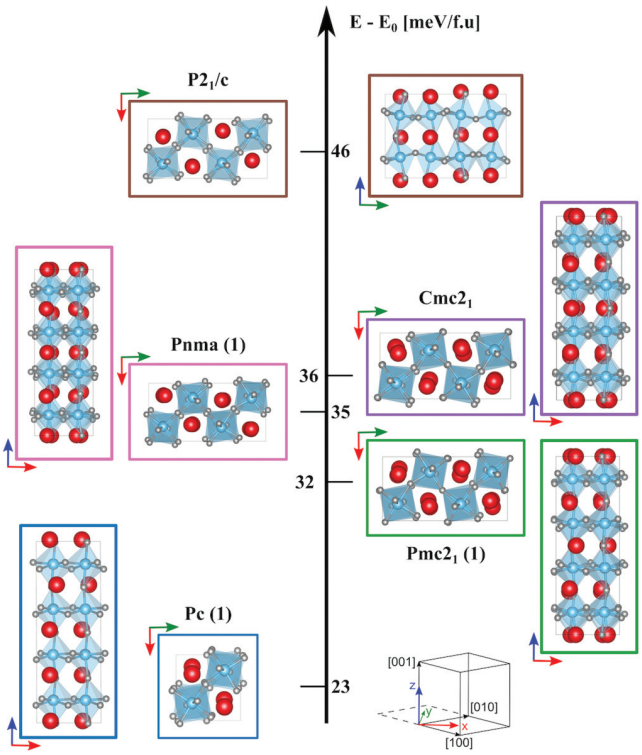

FIG. 1. Crystal structures of new low-energy phases identified by full relaxation using DFT. The vertical axis indicates the energy relative to the $R3c$ ground state. We orient the structures such that the z axis (blue arrow) stands along the usual [001] growth orientation, the x axis (red arrow) is along the $[110]_{pc}$ direction, and the y axis (green arrow) is along the $[\bar{1}10]_{pc}$ direction. The Bi atoms are represented in red, the Fe atoms in blue, and the O atoms in grey.

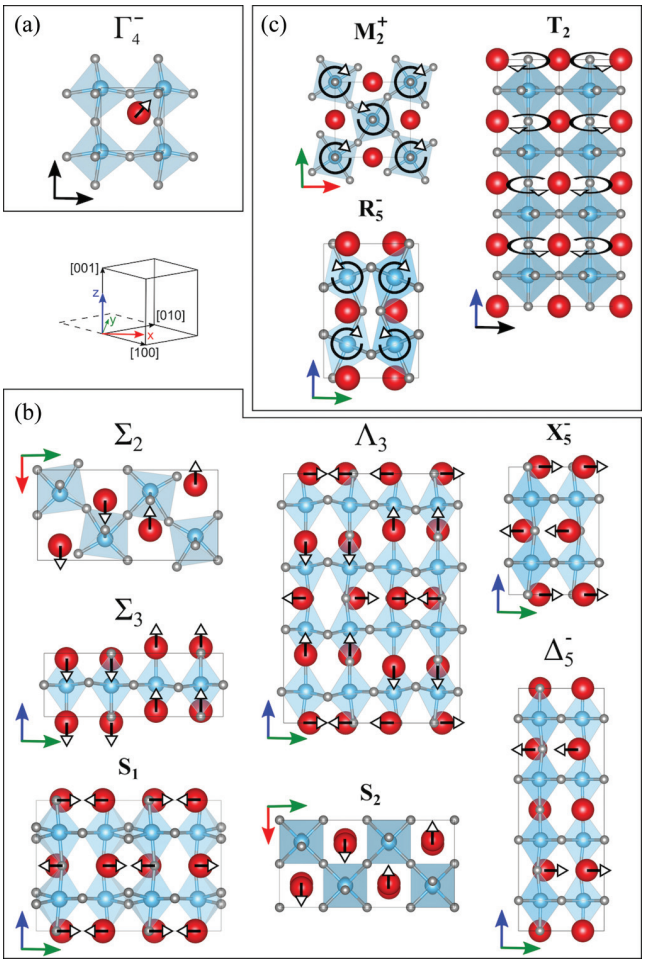

FIG. 2. Main distortion modes. (a) Polar mode dominated by off-centering of the Bi atom relative to the other atoms in the unit cell. Here we show the displacement along the $[011]_{pc}$ direction; displacements along $[001]_{pc}$ (as in the $P4mm$ supertetragonal phase) and along $[111]_{pc}$ (as in the $R3c$ phase) are also known. (b) Antipolar modes, in which pairs of Bi atoms displace with opposite direction and the same amplitude. (c) Rotational and tilting modes, in which the main distortion is the rotation or tilt of the octahedra. The inset shows the orientation of the axes relative to the pseudo cubic directions and the dominant distortions are highlighted by arrows. The color scheme is consistent with Fig. 1.

Before starting the analysis of the new phases identified in the current study, we summarize briefly the previously identified phases for $BiFeO_3$. The $R3c$ ground state is reached from the ideal cubic perovskite structure via a polar displacement along the $[111]_{pc}$ direction (Γ_4^- mode) and a tilting of the octahedra around the same direction (R_5^- mode) resulting in an $a^-a^-a^-$ tilt pattern. At high temperature, $BiFeO_3$ adopts the $GdFeO_3$-like $Pnma$ phase [32], characterized by antipolar displacements of the Bi atoms accompanied by antiphase in-plane rotations and in-phase out-of-plane tiltings of the octahedra, resulting in a $a^-a^-c^+$ tilt pattern. This phase is generally calculated to be the lowest energy metastable phase for $BiFeO_3$ [12,31,33]), although competing phases can be lower energy depending on the choice of exchange-correlation functional [12].

We begin by searching for instabilities at the zone boundaries of the 20-atom $Pnma$ ($GdFeO_3$ structure) and $Pmc2_1$, and the 40-atom $Pbam$ unit cells, and construct the corresponding supercells by doubling the 20- or 40-atom unit cells in one or two directions. In this section, we present results for unit cells of 40 or 80 atoms; larger unit cells will be presented in the next section. The $Pnma$ starting structure did not yield any new phases in this procedure, suggesting that it is likely a true metastable phase. We describe the structures generated from the $Pmc2_1$ and $Pbam$ starting cells next. When different structures share the same symmetry, we will label them with the symmetry followed by an index.

1. $Pmc2_1$ as starting cell

We start from a 20-atom unit cell with $Pmc2_1$ symmetry and find a zone boundary instability along a long and a short lattice vector. Doubling its unit cell along the long lattice vector and subsequent relaxation of the atomic positions yields the 40-atom unit cell Pc (1) structure (see Fig. 1 lower left), which is only 23 meV/f.u. above the ground state and 2 meV/f.u. above the conventional $Pnma$. It is a polar phase with an out-of-plane ([001]) polarization of around 54 $\mu C/cm^2$ and an in-plane ([110]) polarization of about 39 $\mu C/cm^2$. The polarization is mainly due to the

displacement of the eight Bi atoms, six of which shift along the $[1\bar{1}1]_{pc}$ direction and two along the $[\bar{1}11]_{pc}$ direction resulting in a larger out-of-plane than in-plane polarization.

By doubling the 20-atom $Pmc2_1$ unit cell along $[\bar{1}10]_{pc}$ (its short lattice vector), we identify a 40-atom unit cell polymorph with the same symmetry, $Pmc2_1$ (2), which has a large polarization along the [110] pseudocubic direction. It is the highest energy phase that we identify here, with 76 meV/f.u. above the ground state, and the calculations of its phonon band structure indicate that this phase is unstable with a zone-boundary instability at $[0\ 0\ \frac{\pi}{a}]$.

Further doubling the $Pmc2_1$ (2) unit cell along $[001]_{pc}$, and relaxing the atomic positions, we identify a metastable structure of $Cmc2_1$ symmetry with 80 atoms per unit cell (central right panel of Fig. 1). There exists another large unit cell with 80 atoms, $Pmc2_1$ (1), obtained by doubling the unit cell of the original $Pmc2_1$ simultaneously along $[001]_{pc}$ and $[110]_{pc}$ (lower right of Fig. 1). $Pmc2_1$ (1) has a lower polarization than $Pmc2_1$ (2) (16 μC/cm^2 instead of 76 μC/cm^2, due to a smaller amplitude of the Γ_4^- mode), but lower energy (32 meV/f.u. instead of 76 meV/f.u.). The structural difference between $Cmc2_1$ and $Pmc2_1$ (1) lies in the presence of an extra antipolar displacement along x in the case of $Pmc2_1$ (1) that brings the central layer of Bi atoms (third layer of atoms along the z direction) to be almost aligned (see Fig. 1). This difference is due to the absence of a Σ_2 mode [see Fig. 2(b)] in $Cmc2_1$. Moreover, the amplitude of the polar mode is larger in $Cmc2_1$ resulting in a larger polarization than $Pmc2_1$ (1).

Note that there is no zone boundary instability to motivate doubling the remaining short lattice vector of the 20-atom unit cell alone.

2. Pbam as starting cell

Calculating the phonon band structure of the *Pbam* (ground state for $PbZrO_3$ [34,35]) phase, we first identify an unstable mode at the center of the Brillouin zone. Following this unstable mode, we obtain a nonpolar phase, with $P2_1/c$ symmetry and an energy of 46 meV/f.u. above the ground state (upper left of Fig. 1). In this phase, Σ_2 and Σ_3 distortions are present, resulting in an up/down displacement of the Bi atoms both in-plane and out-of-plane and no net polarization (see Fig. 2).

Doubling the *Pbam* unit cell along $[001]_{pc}$ and subsequently relaxing the atomic positions, we obtain two 80-atom structures. First, the *Pnma* (1) phase, which was previously identified [36] and shown experimentally to be antiferroelectric in Ref. [11]. Second, another variant of the same symmetry, *Pnma* (2), which is metastable, but has much higher energy (70 meV/f.u.).

It was shown that the *Pbam* structure of $PbZrO_3$ can be described in termes of three main distortion modes from the ideal cubic perovskite structure, Σ_2, S_2, and R_5^-, which couple cooperatively to lower the energy [37]. *Pnma* (1) and *Pnma* (2) share the three modes inherited from their *Pbam* parent structure, but also share two additional modes, Λ_3 and T_2. While the amplitudes of the three first modes are comparable in *Pnma* (1) and *Pnma* (2), those of Λ_3 and T_2 differ, representing respectively, 14% and 17% of the entire displacement from the cubic phase for *Pnma* (1) and 2% and 12% for *Pnma* (2).

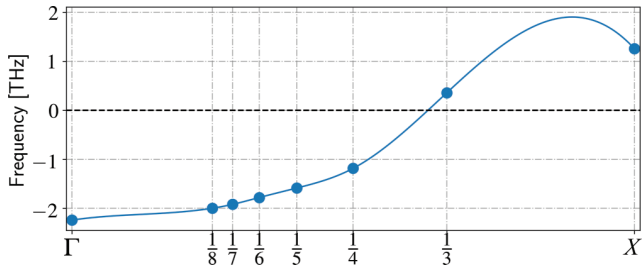

FIG. 3. Phonon band in $Pmc2_1$ phase. We repeat the $Pmc2_1$ unit cell from 2 to 8 times along the $[110]_{pc}$ direction and report the corresponding phonon frequencies. Negative frequencies indicate imaginary (unstable) modes. The dots result from the calculations and we interpolate between them with a cubic interpolation. We observe no unstable phonon modes when doubling (X) or tripling ($\frac{1}{3}$) the unit cell along the $[110]_{pc}$ direction.

B. Long-wavelength structures

Having explored the phase space of 40- and 80-atom unit cells in the previous section, we next extend our systematic search to instabilities at lower q points of the 20-atom $Pmc2_1$ unit cell, and correspondingly larger unit-cell structures.

We built a series of supercells, obtained by repeating the $Pmc2_1$ unit cell from 4 to 8 times along the $[110]_{pc}$ direction. Note that this is the direction for which no instability was found halfway to the Brillouin zone boundary (see Sec. III A 1); we also found no imaginary zone-center phonon modes in supercells built by tripling the $Pmc2_1$ unit cell in that direction (see Fig. 3). For larger supercells, however, we find, that an antipolar distortion mode with Σ_3 symmetry is unstable in the starting supercells across the series, and is associated with a progressively smaller q point in the Brillouin zone of the original $Pmc2_1$ phase as the supercell size is increased [see Figs. 3 and 4(a)]. In addition to this antipolar mode, we observe another wave-vector-dependent mode, responsible for rotations of the octahedra, with S_4 symmetry [see Fig. 4(b)]. To emphasize the wave-vector dependence of these modes we label them Σ_3^q and S_4^q. As previously, we freeze in the distortion eigenvectors corresponding to these and the other unstable modes and fully relax the structures.

We find a series of structures with *Pc* symmetry in unit cells with the long lattice vector ranging from 22.46 to 44.78 Å (corresponding to 80 and 160 atoms per unit cell, respectively). Each structure can be decomposed into four primary distortions: two modes already discussed in the previous section (R_5^- and Γ_4^-) and the two new modes introduced above (Σ_3^q and S_4^q). The R_5^- mode is responsible for the tilts of the octahedra and is present in all the new structures identified in this work, including the *Pc* series we discuss here. The Γ_4^- mode displaces all the Bi atoms in the same direction relative to the other atoms, inducing polarization in all polar structures. In contrast to the $R3c$ phase, the displacement in the new *Pc* phases is not along $[111]_{pc}$ but along $[110]_{pc}$, resulting in purely in-plane polarization. In Figs. 4(a) and 4(b), we show the new Σ_3^q and S_4^q modes for a 33-Å long unit cell. Both modes have distortions with periodicity related to the size of their unit cell. Σ_3^q is an antipolar mode, that moves the Bi atoms along the [001] direction. This mode has a wave

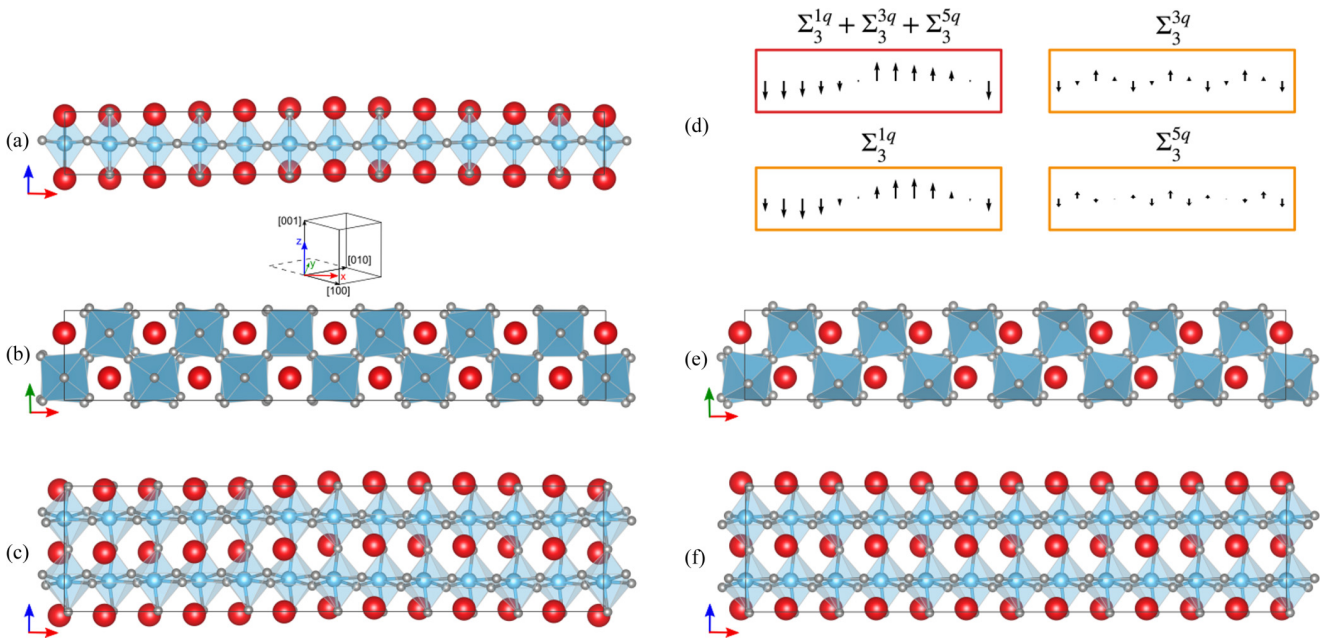

FIG. 4. Long wavelength structural distortions and fully relaxed structure of the 33-Å-long (120-atom) unit cell. (a) Antipolar Σ_3^q mode with sinusoidal displacement of the Bi atoms. (b) Rotational S_4^q mode. (c) Fully relaxed structure with Pc symmetry. (d) Extra Σ_3^{iq} modes with $i = 1, 3, 5$, individually presented (orange boxes) or combined together (red box). (e) $R3c$ symmetry in the unit cell with same lattice vectors as (c) visualized from the top. (f) Structure shown in (e) visualized from the side. The structure in (c) can be decomposed into the modes presented in (a), (b), and (d) combined with a Γ_4^- polar mode and an R_5^- tilting mode. Each unit cell is defined with respect to a common origin, in order to help the comparisons and the orientation relative to the pseudocubic axes is indicated on the bottom left.

vector of $q = [1/2\ 1/2\ 0] \cdot \frac{\pi}{N \cdot a}$, where a is the lattice vector of the parent $Pmc2_1$ structure and N the number of times it was repeated to generate the supercell. It is associated with an "N up - N down" distortion pattern of the Bi atoms, with N Bi atoms moving up and N moving down, with the displacement amplitude modulated by the position along $[110]_{pc}$ by a sinusoid. The last mode, S_4^q, is a rotational mode that creates pairs of clockwise-anticlockwise rotated octahedra along the [001] direction, with an amplitude of rotation modulated by a clipped sine wave (that is a sine wave with a flattened top) along its long lattice vector [Fig. 4(b)].

The structure with 120 atoms is shown in Fig. 4(c) and for comparison, the $R3c$ phase in the same unit cell is displayed in Figs. 4(e) and 4(f). Comparing carefully the antipolar distortions in Figs. 4(a) and 4(c), one can notice that the smooth wavy displacement due to the Σ_3^q mode is not exactly conserved at the center of the unit cell in the latter. We observe that additionally to the Σ_3^q mode with wavevector of $q = [1/2\ 1/2\ 0] \cdot \frac{\pi}{N \cdot a}$ as defined earlier, each structure across the series has additional Σ_3^{iq} modes with $i = 3, 5, 7, \ldots, N$. For instance, in the structure with $q = [1/2\ 1/2\ 0] \cdot \frac{\pi}{6 \cdot a}$, two additional modes with $i = 3$ and $i = 5$ exist. These additional modes have a decreasing amplitude as i increases and they explain the deviation of the displacements of the Bi atoms from a smooth sinusoid as additional modes with shorter periods are superimposed [see Fig. 4(d)].

In order to better understand the distortion trends in this series of structures, we plot in Fig. 5(a) the computed polarization projected on the $[110]_{pc}$ direction and the energy relative to the energy of the $R3c$ phase constrained to the same lattice vectors as a function of the inverse of the long lattice vector. We observe that both values decrease and tend to the $R3c$ values as the unit cell size increases. This suggests that the series could converge to an analog to the $R3c$ phase with in-plane polarization. In Fig. 5(b), we plot the maximum and average displacement of the Bi atoms along $[001]_{pc}$ and of the octahedra as a function of the inverse of the long lattice vector. We see that, as the unit cell size is increased, the average values for both Bi displacements and octahedral rotations, as well as the maximum values for the rotations, approach the $R3c$ values. In striking contrast, the *maximum* displacement of the Bi atoms along $[001]_{pc}$ (antipolar displacements) *increases* from the bulk $R3c$ value (polar displacements) as the cell size is increased. These trends are explained by the increase of both Σ_3^q and S_4^q modes when q decreases. In a simple picture, as the octahedra have larger amplitudes of rotation, more space is left for the Bi atoms to move. These observations further indicate that the series in fact converges to a structure distinct from the $R3c$ ground state, although it is likely to be quite close in energy.

We analyze the distortions further by plotting in Fig. 5(c) the displacements of each Bi atom along $[001]_{pc}$ as well as the rotation of each octahedron around the same direction, in the 160-atom unit cell. The values for the $R3c$ structure are shown with the dashed lines for comparison. In the case of $R3c$, all Bi atoms are displaced in the same direction (whether up or down) and the octahedra rotate clockwise in one (111) layer and anticlockwise in the next (111) layer (below or above the Bi atoms). In the Pc phase, at the center of the unit cell, at around 20 Å, one can see the crossover between up and down

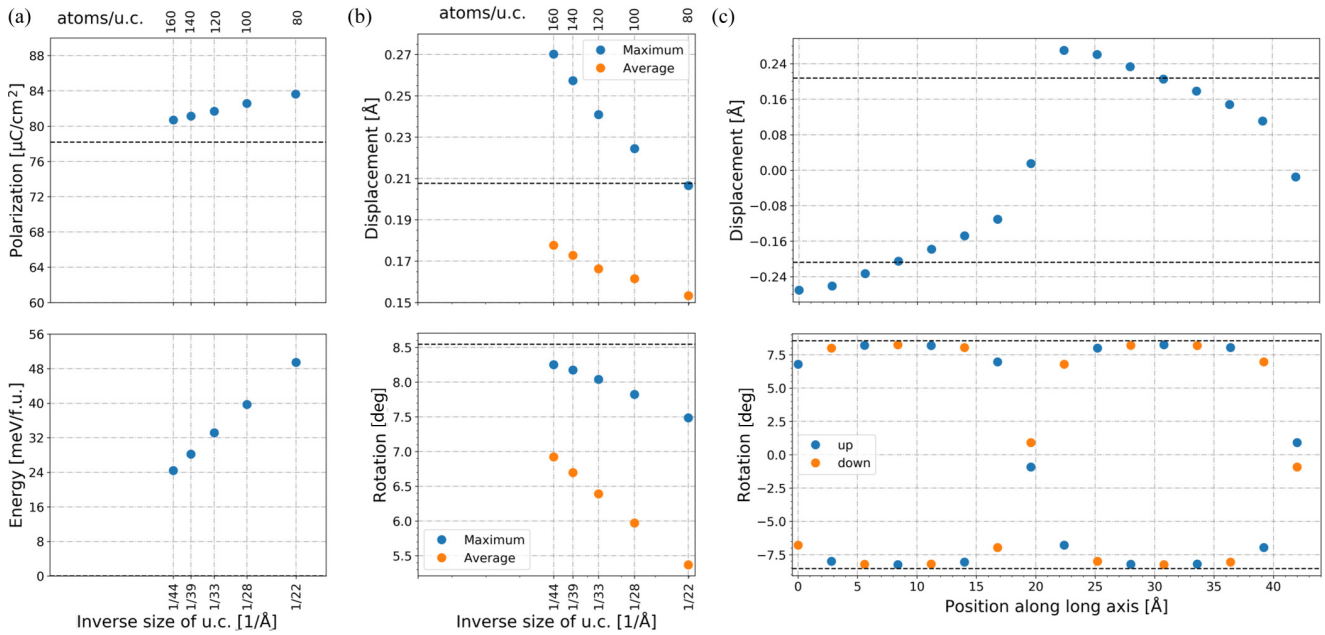

FIG. 5. Energy, polarization, Bi displacements and oxygen octahedral rotations across the *Pc* series, and distortions within the 160-atom u.c. (a) Polarization (top) and energy (bottom) as a function of the inverse of the long lattice vector. (b) Maximum (blue) / average (orange) displacement of the Bi atoms along $[001]_{pc}$(top) and maximum (blue) / average (orange) rotation of the octahedra (bottom) as a function of the long lattice vector. The average values are computed from the arithmetic mean over the absolute value of all displacements of the Bi atoms, or over all rotations of the octahedra. (c) Layer-by-layer displacement of each Bi atom (top) and rotation of each octahedron (bottom) in the 160-atom unit cell. The orange and blue dots represent octahedra above (blue) or below (orange) the Bi atoms of the top panel. The dotted lines indicate the behavior of the *R*3*c* in the same unit cell as the 160-atom unit cell.

displacements of the Bi atoms, whereas at the center of the cell, there is almost no distortion: the Bi atom sits at the center of the cell (vertically) and the octahedra above and below are almost not rotated (a^0-like in Glazer notation). Going away from the center, the octahedra rotate in opposite directions to the left or to the right of the unit cell (with opposite rotations of the top and bottom layers) and the Bi atoms move up in the right and down in the left side of the unit cell. The bulk behavior is recovered, with displacements and rotations close to the *R*3*c* values, midway between the center and the edges of the supercell, with opposite displacements / rotations in each half of the supercell.

As the unit cell size is increased, the amplitudes of the Σ_3^q and S_4^q modes grow. The rotations approach the ground-state *R*3*c* value. The displacements become progressively larger, resulting in displacements larger than the bulk values. We attribute the lowering of the energy with increasing cell size to the smoother transition between consecutive octahedra, confirming previous studies [38,39], and anticipate that the energy would continue decreasing with increasing cell size. Since the amplitude of the antipolar displacements increases with the size of the unit cell, we expect large antipolar distortions in the large unit cell limit. This could be interpreted as opposite domains of polarization along $[001]_{pc}$, while preserving the in-plane components. Each domain keeps the *Pc* symmetry but with displacements along $[001]_{pc}$ averaging to the *R*3*c* value and resulting in a similar polarization value. Note that each half of the unit cell is also different than *R*3*c*.

In summary, we have identified a series of structures that allow rotation of the polarization away from the $[111]_{pc}$ direction and into the (110) plane at minimal energy cost. This behavior is relevant for $BiFeO_3$ thin films and heterostructures in which the electrostatic boundary conditions might favor phases with no out-of-plane polarization. We explore this scenario next.

IV. EXPERIMENTAL STABILITY AND HETEROSTRUCTURES

Finally, in this section we explore two possible routes to stabilizing experimentally the various phases identified above. The first is biaxial strain, which can be imposed by a substrate of different lattice constant through coherent heteroepitaxy. Since the different structures have different unit cell sizes and shapes, we expect that their relative stabilities will be modifiable by careful choice of in-plane lattice parameter lengths and orientations. The second is through exploiting the electrostatic boundary conditions at the interfaces in heterostructures or superlattices with nonpolar III-III perovskite oxides. Since there is an electrostatic energy cost associated with a polar discontinuity, such an arrangement destabilizes phases with an out-of-plane polarization component, including the ground-state *R*3*c* phase in the usual [001] growth orientation [40].

We continue the convention of Figs. 1 and 2 in which we oriented the usual $[001]_{pc}$ growth orientation along the cartesian *z* direction for all the structures. We therefore refer to the axis parallel to the z direction as the out-of-plane axis, and we apply in-plane strain.

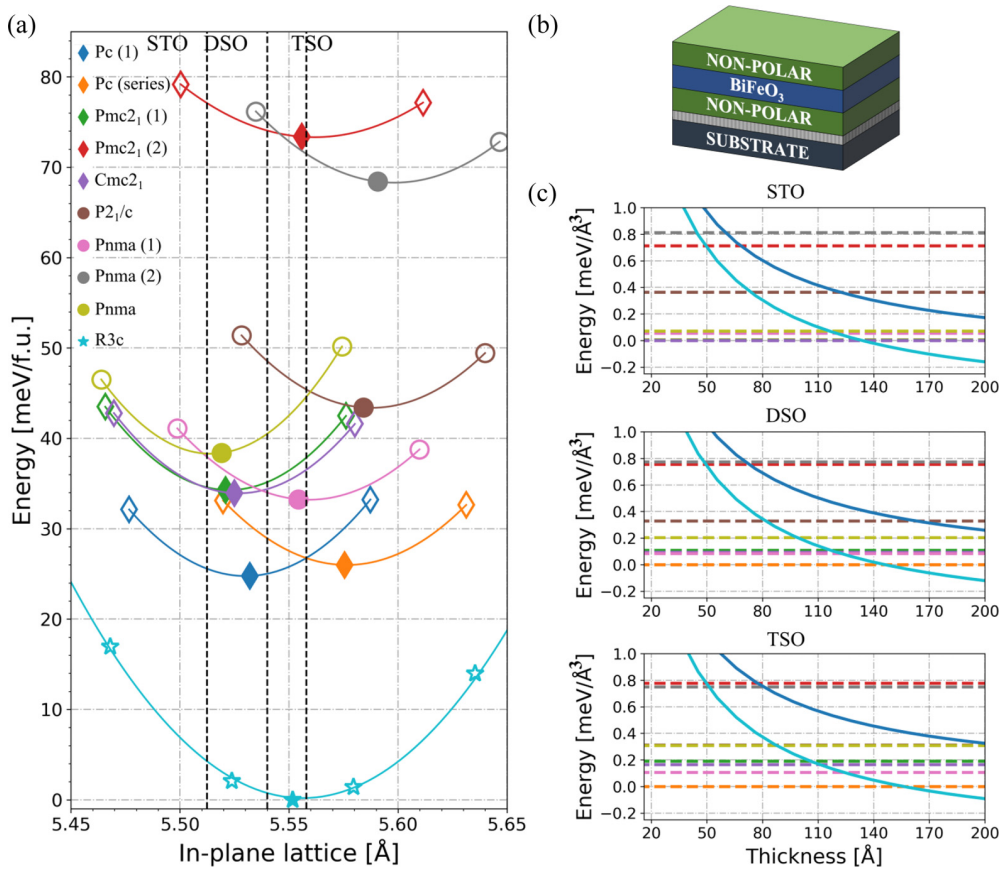

FIG. 6. Strain and electrostatics. (a) Energy as a function of the average in-plane lattice parameter. We consider each phase presented in Table I and the *Pc* phase presented in Fig. 5. For each case, we average the in-plane lattice constants, apply the strain value, then relax the length of the out-of-plane lattice constant as well as the positions of the ions. We indicate the resulting energies and lattice constants with full diamonds, full circles or full stars, for polar, nonpolar, and *R*3*c* phases, respectively. For the *R*3*c* phase, we used a 10-atom unit cell and kept the rhombohedral angle to be 60° as described in Ref. [6]. We then apply a 1% compressive and tensile strain to each structure and fit the data points with a parabola. The vertical dashed lines represent the lattice vectors calculated in this work of common substrates: $SrTiO_3$ (STO), $DyScO_3$ (DSO) and $TbScO_3$ (TSO). (b) Cartoon of the heterostructure considered for (c). We consider a superlattice of BFO surrounded by a nonpolar III-III material (e.g., $LaFeO_3$) separated from the substrate (bottom) by a metallic electrode. (c) Energy as a function of the thickness of the BFO layer. We consider each of the phases presented in (a) and assume that they are surrounded by a III-III nonpolar material with a strain imposed by the substrate (STO, DSO or TSO, respectively from top to bottom panel). We report the energy density relative to the lowest nonpolar phase. The colors are consistent with (a) and we indicate with dashed lines the phases that have zero component of the polarization perpendicular to the interface. The volume and energy for each phase for a given substrate are extracted from (a).

A. Strain

In Fig. 6(a), we show the calculated energies for the phases of Table I as a function of their in-plane averaged lattice parameters (before applying any strain value we first average the two in-plane lattice vectors and redefine the unit cell accordingly). We make the choice to keep the angles between the lattice vectors fixed and average the pseudocubic in-plane lattice constants before applying the compressive or tensile strain, which increases the energy of the unstrained structures (full markers) compared to the values reported in Table I.

We find that, in the range of in-plane lattice parameters that we consider, none of the low-energy phases is stabilized by strain over the *R*3*c* ground state. The energy difference between the low-energy competing phases and the ground state is sometimes substantially reduced on typical substrates however. For instance, the energy difference between *Pc* (1) and *R*3*c* is reduced from 28 meV/f.u. at the lattice constant of $TbScO_3$ (TSO) to 21 meV/f.u. at the lattice constant of $SrTiO_3$ (STO). The results presented in Fig. 6 show that, while moderate strain alone is insufficient to stabilize metastable phases, it makes a difference quantitatively and should not be neglected. Note that we only consider in-plane lattice parameters within 2% (either smaller or larger) of the ground-state *R*3*c* value; such strains are experimentally accessible for film thicknesses up to around 20 nm.

B. Electrostatics and polar discontinuity

According to Gauss's law, an electric charge causes a divergent electric displacement field with divergence equal to the charge density. Therefore the bound charge at an interfacial polar discontinuity between a polar and a nonpolar material will induce an electric field, with divergence proportional to the density of charge at the interface. This scenario is

energetically unfavorable and is well known to be responsible for the critical thickness below which a ferroelectric material loses its net polarization [41]. In order to reduce its electrostatic energy, an unscreened ferroelectric material usually splits into domains of alternating up and down polarization, resulting in a globally zero net polarization. However, if a low-energy nonpolar phase, or a phase with polarization oriented in a plane parallel to the interface exists, a transition to a new phase could be more favorable than domain formation [42]. This behavior was demonstrated for superlattices of $BiFeO_3$/(La, Bi)FeO_3, in which the phase labeled *Pnma* (1) in this work was stabilized in the $BiFeO_3$ layers [11].

Next, we explore whether the other low-energy phases identified in this work can be stabilized relative to the *R*3*c* ground state with experimentally accessible electrostatic boundary conditions.

The bound charges induce a depolarizing field, given by $E_d = \frac{-P}{\epsilon_0 \epsilon_r}$, in the opposite direction to the polarization, where ϵ_0 is the permittivity of the free space and ϵ_r the relative permittivity of the material in which the electric field is created. The depolarizing field then couples with the polarization, giving an electrostatic energy cost of $\frac{1}{2}\frac{P^2}{\epsilon_0 \epsilon_r}$ [43]. Note that this electrostatic energy cost is proportional to the interfacial area, whereas the internal energy, given by the energy difference between the two bulk phases at the appropriately strained in-plane lattice constant, is proportional to the volume. Therefore we expect a crossover in their relative contributions with film thickness, with the electrostatic energy dominating in thin films [40].

We consider a heterostructure of $BiFeO_3$ surrounded by a III-III nonpolar perovskite (e.g., $LaFeO_3$) separated from a substrate (STO, TSO, or DSO) by a metallic electrode [see Fig. 6(b)]. In Fig. 6(c), we show the calculated energies of thin films of the various phases of $BiFeO_3$ as a function of thickness, with the lattice constant fixed to that of the STO, TSO, or DSO substrate, and the electrostatic boundary conditions set by imposing zero electric displacement field outside the $BiFeO_3$ layer. The calculated total energy consists of three contributions: the internal energy relative to the *R*3*c* phase (including the effect of strain from the substrate), the electrostatic energy from the polar discontinuity at the interface, and a screening energy to decrease the amount of bound charge at the interface and reduce the electrostatic energy. As in Ref. [11], we assume that the system is single domain and take generation of electron-hole pairs across the band gap as the screening mechanism; this is likely to provide an upper bound value on the screening energy cost.

Among the polar phases reported in Fig. 6(a), only *Pc* (1) and *R*3*c* have an out-of-plane component of the polarization, 54 and 58 $\mu C/cm^2$, respectively, so their energy density decreases as a function of the thickness, while all other phases have a constant energy density, given by the internal energy. We find that *Pc* (1) is unlikely to be stabilized on the considered substrates, as the smaller polarization is not enough to compensate the internal energy compared to *R*3*c*. On STO, two phases with in-plane polarization, $Pmc2_1$ (1) and $Cmc2_1$, are more stable than *R*3*c* at low thicknesses. On the other hand, the largest structure from the series of *Pc* phases is more stable than *R*3*c* on DSO and TSO. We see that, as expected, the critical thickness at which the phase with zero out-of-plane polarization becomes stable is smaller when the difference in strain energy between the polar ground state and the lowest nonpolar phase is smaller.

We predict that $BiFeO_3$ on the different substrates considered would recover its bulk behavior only for thicknesses larger than 10 nm. As we mentioned, the electrostatic model that we chose is likely an upper bound estimation of the screening cost, which results in a likely overestimation of the electrostatic energy and critical thickness. Note also that due to the prohibitive cost of DFT calculations, we do not consider the competing mechanism of domain formation. This would be a fruitful direction for future second-principles or phase-field calculations. Nevertheless, our predictions suggest a new route to stabilizing new phases in $BiFeO_3$-based oxide heterostructures, through the control of the electrostatics at the interface.

V. SUMMARY AND CONCLUSION

In summary, we used first-principles density functional theory to explore the low-energy phase space of $BiFeO_3$ systematically. We considered well-known polymorphs of $BiFeO_3$ and computed the phonon frequencies at high symmetry *q* points to identify instabilities indicating structures of lower energy. Using this procedure, we showed that the previously discussed *Pbam* and $Pmc2_1$ phases are in fact unstable. We first showed that several new metastable phases exist within an energy range of 50 meV/f.u. above the ground state in a unit cell of 80 atoms. These phases exhibit complex distortions and tilts that are beyond the scope of the traditional Glazer notation. We proposed an extension to the Glazer notation making it suitable for general tilt patterns. We then extended our study to larger unit-cell sizes by increasing the size of the original $Pmc2_1$ unit cell along one lattice vector up to a total cell size of 160 atoms. We discovered the existence of a series of noncentrosymmetric structures that are polar in the pseudocubic *x*-*y* plane, and antipolar in the perpendicular direction. We showed that the antipolar mode is modulated by the size of the unit cell and couples to a rotational mode that is similarly modulated. In the large supercell limit, these phases are reminiscent of opposite domains of polarization along the out-of-plane direction. Finally, we discussed the possibilities for stabilizing these phases experimentally and showed that the lowest energy phases without out-of-plane polarization could in principle be stabilized using a combination of strain and electrostatics at the interface between $BiFeO_3$ and a nonpolar III-III perovskite. Future work could include an analysis of the role of other interfacial features such as matching of the tilt patterns of the oxygen octahedra in determining phase stability.

Our approach of using phonon instabilities in a systematic way to explore the phase space of $BiFeO_3$, is of course broadly applicable to any material. It is limited, however, by the computational cost of the subsequent structural relaxations in the large unit cells. We hope, therefore, that our identification of many large unit cell low-energy phases will motivate further theoretical studies of the phase space of $BiFeO_3$ and related materials with modern tools such as machine learning or second-principles methods. These could reveal additional

polymorphs with desirable properties such as antiferroelectricity. An extension to predict detailed magnetic properties would also be of interest, in particular to search for phases with a large net magnetic moment.

On the experimental front, we identified several new low-energy structures in $BiFeO_3$, as well as routes for stabilizing them, which we hope will be helpful in the design of new heterostructures with targeted properties. In particular, our study of the series of phases with *Pc* symmetry showed that for large unit cells, reorientation of the polarization is possible with minimal energy cost, and the distinction between phase and domains becomes blurred. The *Pc* phases could therefore provide a starting point for engineering polar vortices [44] in $BiFeO_3$-based oxide heterostructures.

ACKNOWLEDGMENTS

We acknowledge financial support from ETH Zürich and the Körber foundation. Computational resources were provided by ETH Zürich and the Swiss National Supercomputing Center (CSCS), Project ID No. s889. The visualizations of the structures were done with VESTA [45] and we used AGATE [46] to compute the rotation angles for the octahedra. We thank Kane Shenton for helpful comments on the manuscript.

[1] J. Wang, J. B. Neaton, H. Zheng, V. Nagarajan, S. B. Ogale, B. Liu, D. Viehland, V. Vaithyanathan, D. G. Schlom, U. V. Waghmare, N. A. Spaldin, K. M. Rabe, M. Wuttig, and R. Ramesh, Science **299**, 1719 (2003).
[2] F. Kubel and H. Schmid, Acta Cryst. **B46**, 698 (1990).
[3] H. Béa, B. Dupé, S. Fusil, R. Mattana, E. Jacquet, B. Warot-Fonrose, F. Wilhelm, A. Rogalev, S. Petit, V. Cros, A. Anane, F. Petroff, K. Bouzehouane, G. Geneste, B. Dkhil, S. Lisenkov, I. Ponomareva, L. Bellaiche, M. Bibes, and A. Barthélémy, Phys. Rev. Lett. **102**, 217603 (2009).
[4] R. J. Zeches, M. D. Rossell, J. X. Zhang, A. J. Hatt, Q. He, C.-H. Yang, A. Kumar, C. H. Wang, A. Melville, C. Adamo, G. Sheng, Y.-H. Chu, J. F. Ihlefeld, R. Erni, C. Ederer, V. Gopalan, L. Q. Chen, D. G. Schlom, N. A. Spaldin, L. W. Martin *et al.*, Science **326**, 977 (2009).
[5] H. M. Christen, J. H. Nam, H. S. Kim, A. J. Hatt, and N. A. Spaldin, Phys. Rev. B **83**, 144107 (2011).
[6] A. J. Hatt, N. A. Spaldin, and C. Ederer, Phys. Rev. B **81**, 054109 (2010).
[7] Y. Yang, W. Ren, M. Stengel, X. H. Yan, and L. Bellaiche, Phys. Rev. Lett. **109**, 057602 (2012).
[8] J. C. Yang, Q. He, S. J. Suresha, C. Y. Kuo, C. Y. Peng, R. C. Haislmaier, M. A. Motyka, G. Sheng, C. Adamo, H. J. Lin, Z. Hu, L. Chang, L. H. Tjeng, E. Arenholz, N. J. Podraza, M. Bernhagen, R. Uecker, D. G. Schlom, V. Gopalan, L. Q. Chen *et al.*, and Phys. Rev. Lett. **109**, 247606 (2012).
[9] D. P. Kozlenko, A. A. Belik, A. V. Belushkin, E. V. Lukin, W. G. Marshall, B. N. Savenko, and E. Takayama-Muromachi, Phys. Rev. B. **84**, 094108 (2011).
[10] W. Dong, J. J. P. Peters, D. Rusu, M. Staniforth, A. E. Brunier, J. Lloyd-Hughes, A. M. Sanchez, and M. Alexe, Nano Lett. **20**, 6045 (2020).
[11] J. A. Mundy, C. A. Heikes, B. F. Grosso, D. F. Segedin, Z. Wang, B. H. Goodge, Q. N. Meier, C. T. Nelson, B. Prasad, L. F. Kourkoutis, W. D. Ratcliff, N. A. Spaldin, R. Ramesh, and D. G. Schlom, arXiv:1812.09615.
[12] O. Diéguez, O. E. González-Vázquez, J. C. Wojdel, and J. Íñiguez, Phys. Rev. B. **83**, 094105 (2011).
[13] A. M. Glazer, Acta. Cryst. **B28**, 3384 (1972).
[14] W. Kohn and L. J. Sham, Phys Rev. **140**, A1133 (1965).
[15] P. E. Blöchl, Phys Rev. B **50**, 17953 (1994).
[16] G. Kresse and J. Furthmüller, Phys Rev. B **54**, 11169 (1996).
[17] J. P. Perdew, K. Burke, and M. Ernzerhof, Phys Rev. Lett. **77**, 3865 (1996).
[18] J. B. Neaton, C. Ederer, U. V. Waghmare, N. A. Spaldin, and K. M. Rabe, Phys. Rev. B **71**, 014113 (2005).
[19] J. K. Shenton, D. R. Bowler, and W. L. Cheah, J. Phys. Condens. Matter **29**, 445501 (2017).
[20] S. L. Dudarev, G. A. Botton, S. Y. Savrasov, C. J. Humphreys, and A. P. Sutton, Phys Rev. B **57**, 1505 (1998).
[21] M. Goffinet, P. Hermet, D. I. Bilc, and P. Ghosez, Phys. Rev. B **79**, 014403 (2009).
[22] A. Jain, S. P. Ong, G. Hautier, W. Chen, W. D. Richards, S. Dacek, S. Cholia, D. Gunter, D. Skinner, G. Ceder, and K. A. Persson, APL Mater. **1**, 011002 (2013).
[23] A. Togo and I. Tanaka, Scr. Mater. **108**, 1 (2015).
[24] T. Stokes, D. M. Hatch, and B. J. Campbell, see https://iso.byu.edu.
[25] B. J. Campbell, H. T. Stokes, D. E. Tanner, and D. M. Hatch, J. Appl. Cryst. **39**, 607 (2006).
[26] D. Orobengoa, C. Capillas, M. I. Aroyo, and J. M. Perez-Mato, J. Appl. Cryst. **42**, 820 (2009).
[27] J. M. Perez-Mato, D. Orobengoa, and M. I. Aroyo, Acta Cryst. **A66**, 558 (2010).
[28] S. P. Ong, W. D. Richards, A. Jain, G. Hautier, M. Kocher, S. Cholia, D. Gunter, V. L. Chevrier, K. A. Persson, and G. Ceder, Comput. Mater. Sci. **68**, 314 (2013).
[29] M. D. Peel, S. P. Thompson, A. Daoud-Aladine, S. E. Ashbrook, and P. Lightfoot, Inorg. Chem. **51**, 6876 (2012).
[30] B. Xu, D. Wang, J. Íñiguez, and L. Bellaiche, Adv. Funct. Mater. **25**, 552 (2014).
[31] O. Diéguez and J. Íñiguez, Phys. Rev. Lett. **107**, 057601 (2011).
[32] S. Geller, J. Chem. Phys. **24**, 1236 (1956).
[33] S. Prosandeev, D. Wang, J. Íñiguez, and L. Bellaiche, Adv. Funct. Mater. **23**, 234 (2012).
[34] E. Sawaguchi, H. Maniwa, and S. Hoshino, Phys. Rev. **83**, 1078 (1951).
[35] E. S. G. Shirane and Y. Takagi, Phys. Rev. **84**, 476 (1951).
[36] D. D. Khalyavin, A. N. Salak, N. M. Olekhnovich, A. V. Pushkarev, Y. V. Radyush, P. Manuel, I. P. Raevski, M. L. Zheludkevich, and M. G. S. Ferreira, Phys. Rev. B **89**, 174414 (2014).
[37] J. Íñiguez, M. Stengel, S. Prosandeev, and L. Bellaiche, Phys. Rev. B **90**, 220103(R) (2014).
[38] A. Lubk, S. Gemming, and N. A. Spaldin, Phys. Rev. B **80**, 104110 (2009).
[39] O. Diéguez, P. Aguado-Puente, J. Junquera, and J. Íñiguez, Phys. Rev. B **87**, 024102 (2013).

[40] M. Stengel and J. Íñiguez, Phys. Rev. B **92**, 235148 (2015).
[41] J. Junquera and P. Ghosez, Nature (London) **422**, 506 (2003).
[42] E. Bousquet, J. Junquera, and P. Ghosez, Phys. Rev. B **82**, 045426 (2010).
[43] M. Marvan and J. Fousek, Phys. Stat. Sol. B **208**, 523 (1999).
[44] A. K. Yadav, C. T. Nelson, S. L. Hsu, Z. Hong, J. D. Clarkson, C. M. Schlepütz, A. R. Damodaran, P. Shafer, E. Arenholz, L. R. Dedon, D. Chen, A. Vishwanath, A. M. Minor, L. Q. Chen, J. F. Scott, L. W. Martin, and R. Ramesh, Nature (London) **530**, 198 (2016).
[45] K. Momma and F. Izumi, J. Appl. Cryst. **44**, 1272 (2011).
[46] https://github.com/piti-diablotin/agate

4.3 OTHER PREVIOUSLY UNREPORTED PHASES

In this section we present different predicted phases that were not reported in Ref. [88]. First, we present three phases that were found by building supercells starting from the smallest possible $Pbam$ unit cell. Second, we show another series of structures with large unit cells and Pc symmetry but with a different orientation with respect to the series presented in the previous section. Finally, we explore phases stabilised in supercells of the $P4mm$ structure that is stable under large compressive strain. Note that the parameters used in the calculations are kept as described in Ref. [88].

4.3.1 STARTING AGAIN WITH $Pbam$

We saw in section 3.3.1 of the previous chapter, as well as in section III.A.2 of Ref. [88] (previous section) that doubling the $Pbam$ unit cell along the $[001]_{pc}$ direction results in metastable structures with Pnma symmetry.

We find that other instabilities exist when doubling $Pbam$ along its b lattice vector (with b defined in Fig. 11a). Following the same procedure as described in the previous section, we identify another phase with Pc symmetry (62 meV/f.u above R3c), as well as a phase with $P2/m$ symmetry (71 meV/f.u above R3c). The former has lattice vectors $a = 5.56$ Å, $b = 22.41$ Å and $c = 7.75$ Å and the latter $a = 5.57$ Å, $b = 22.44$ Å and $c = 7.72$ Å. While the Pc symmetry is non-centrosymmetric, we find a small polarisation along the a direction of about 0.9 $\mu C/cm^2$. Note that no spontaneous polarisation is allowed by symmetry in the $P2/m$ phase.

In terms of modes we find that the structure with Pc symmetry can be approximated by adding to the cubic perovskite the R_5^-, Σ_2, S_4, S_2 and Σ_2 modes (sorted by descending contribution to the total distortion). Note that the Γ_4^- mode related to the polarisation is present but with a very small amplitude, consistent with the small spontaneous polarisation value. The structure of the $P2/m$ phase is simpler in the sense that only three main modes are present: R_5^-, Σ_2 and S_2.

While we do not find any instabilities when the $Pbam$ unit cell is doubled along the a direction (see Fig. 11a), we find another structure with Cm symmetry (63 meV/f.u above R3c) when $Pbam$ is jointly doubled along b and c resulting in a 160-atom unit cell. This phase has lattice vectors $a = 5.55$ Å, $b = 22.39$ Å and $c = 15.54$ Å and has five main distortion modes: R_5^-, Σ_2, C_2, S_2 and C_1. It shares the R_5^-, Σ_2 and S_2 modes with $Pnma(1)$ but Λ_3 is replaced by C_1 and T_2 is replaced by C_2. Indeed the "2up-2down / flat / 2down-2up" displacement pattern (Λ_3) is replaced by a more complex pattern with larger period: "up-down-2up-down-up-2down / flat / down-up-2down-up-down-2up" due to the C_1 mode (see Fig. 19a). Similarly, the T_2 mode present in $Pnma(1)$, responsible for the double rotations along the c axis (pairs of octahedra rotating clockwise or anti-clockwise, see Fig. 12b) is replaced by a mode with larger period, that imposes double rotations along c but with patterns repeated along b (see Fig.

19). These patterns are correlated with the up and down displacement as the double tilts are repeated along b when pairs of Bi cations are displaced along c. While the Cm symmetry allows spontaneous polarisation by symmetry, the Γ_4^- mode is small resulting in a small spontaneous polarisation[2] of 1.8 $\mu C/cm^2$ along a.

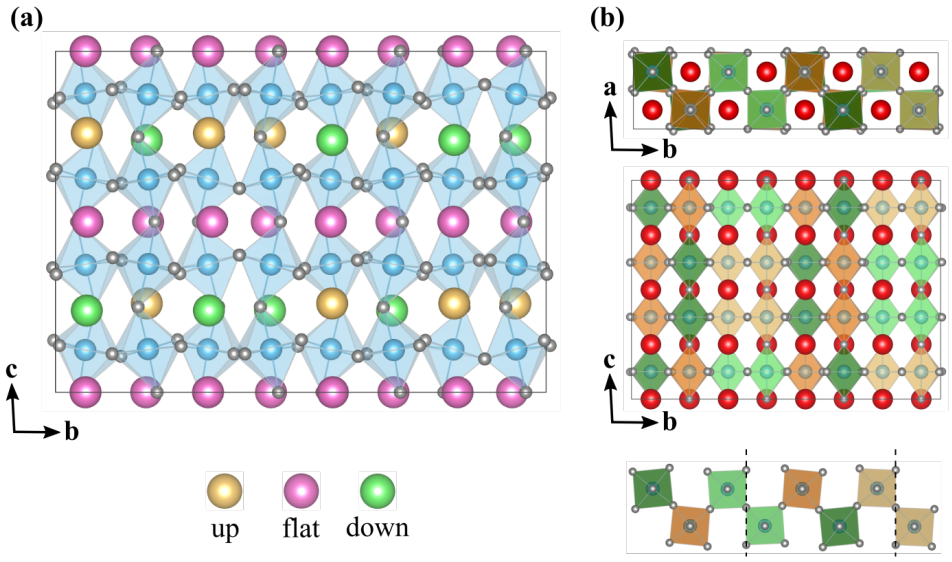

Figure 19: Structure of the Cm phase. (a) Unit cell with the Fe and O atoms respectively in blue and grey. The Bi atoms are coloured in yellow, pink and green if moving along **c**, not moving (flat) and moving along −**c** respectively. The structure displays a "up-down-2up-down-up-2down / flat / down-up-2down-up-down-2up" displacement pattern due to a C_1 symmetry mode. (b) C_2 mode responsible for the octahedral rotations imaged along two directions (top and middle). The bismuth atoms are coloured in red and the octahedra are coloured according to their rotation: dark and light green indicate anti-clockwise rotations, while dark and light orange represent clockwise rotations. The lighter colours represent octahedra whose half distorts rather than rotate (see dashed lines, bottom image).

4.3.2 ANOTHER Pc SERIES

In the publication presented in section 4.2 we show that there exists a series of structures with Pc symmetry and long lattice vector ranging from 22.46 to 44.76 Å. We will refer to this series as $Pc^{(s1)}$. We obtained those phases by repeating the $Pmc2_1$ unit cell from 4 to 8 times along the $[110]_{pc}$ direction. We present here another series of structures with the same symmetry obtained by a similar procedure but repeating the $Pmc2_1$ unit cell along the $[\bar{1}10]_{pc}$ direction. We label this new series $Pc^{(s2)}$. Both series share the same distortion modes (Γ_4^-, R_5^-, Σ_3 and S_4), but with a different orientation of the R_5^- and Γ_4^- modes with

[2]Spontaneous polarisation computed using the averaged born effective charges values computed in Ref. [88]

respect to the long axis. While in the $Pc^{(s1)}$ series, the polar displacements (Γ_4^-) are along the long axis and the tilts (R_5^-) perpendicular to it, in the $Pc^{(s2)}$ series they are the other way around. In both series, the two other modes with long wave vectors (Σ_3 and S_4) are identical, with both lying along the long axis.

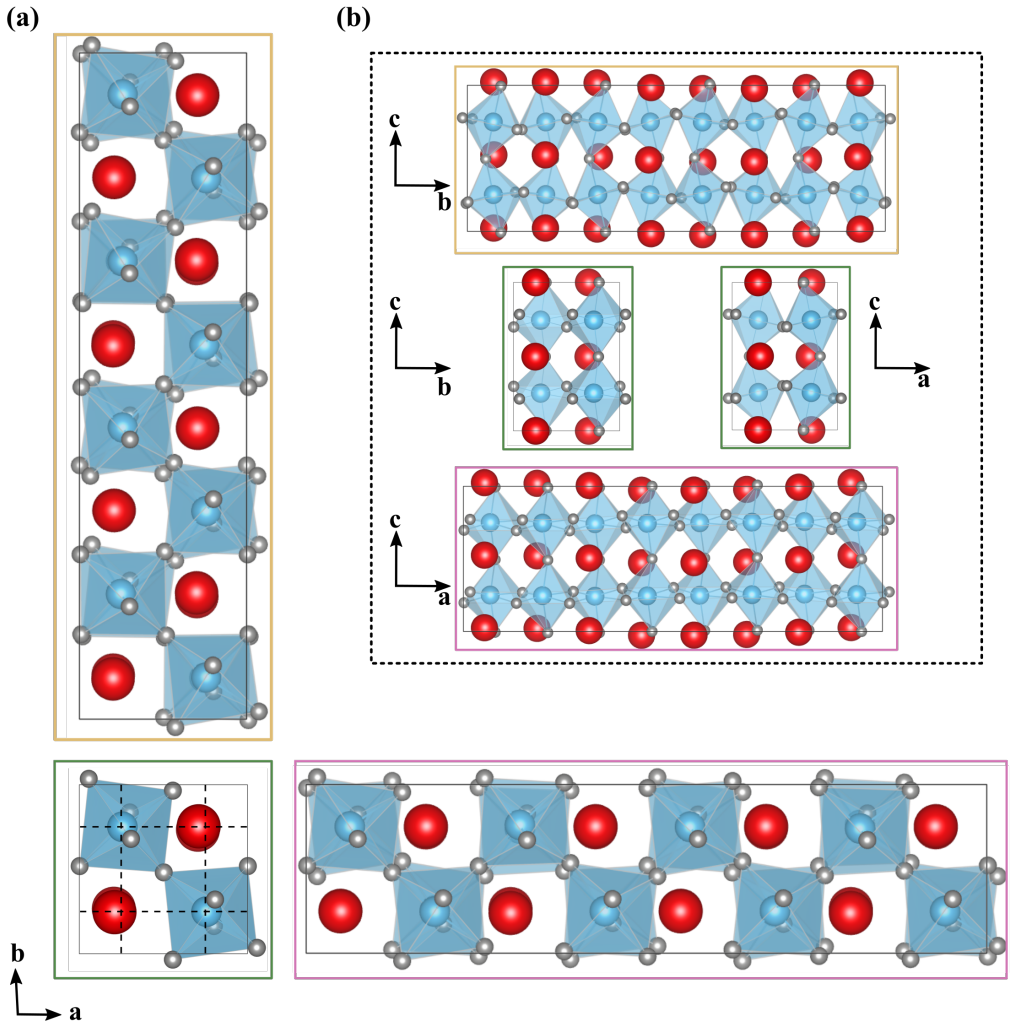

Figure 20: Pc series and $Pmc2_1$ phase. (a) The $Pmc2_1$ parent phase (square structure at bottom left) and the two series of structures with Pc symmetry, with $Pc^{(s1)}$ built along **a** (along the bottom of the figure) and $Pc^{(s2)}$ along **b** (along the left vertical axis of the figure). Each Pc structure is built by repeating the $Pmc2_1$ four times along **a** or **b** respectively. The $Pmc2_1$ phase has the polarisation vector along **a** (the intersection of the dashed lines display the high symmetry positions). (b) Different orientations of each phase presented in (a). One can see that the orientation of the polarisation and tilts is consistent with the parent phase.

The difference of orientations between both series takes its origin in the initial orientation of both modes in the $Pmc2_1$ parent phase. Indeed, in the $Pmc2_1$ phase the polar displacements are along **b**, while the antipolar movements of the O anions, responsible for the tilts, are perpendicular to the **b** direction. These

Phase	a [Å]	b [Å]	c [Å]	Energy [meV/f.u.]
Pc(4)	5.59	22.27	7.79	51
Pc(5)	5.59	27.82	7.80	41
Pc(6)	5.58	33.35	7.81	35
Pc(8)	5.59	44.46	7.81	43

Table 2: Lattice parameters and energies for the structures in the $Pc^{(s2)}$ series. The numbers in parenthesis indicate the number of times that the $Pmc2_1$ phase was repeated along **b**. The energy is given relative to the R3c ground state.

two modes keep then the same relative orientation in both series of structures with new long wave vector modes stabilised along the elongated direction (see Fig. 20).

We find that the spontaneous polarisations in the two series have different orientation relative to the long axis, but are similar in magnitude with values around 80 $\mu C/cm^2$. Also, the energy behaves differently in the two series. While the energy of the $Pc^{(s1)}$ series decreases as unit cell size increases, the $Pc^{(s2)}$ has an energy minimum for the cell with the long vector equal to 33.35 Å before the energy increases again.

4.3.3 HIGHLY-STRAINED POLYMORPHS

We start by fully relaxing a 20-atom cell with symmetry constrained to the P4mm phase and obtain the lattice parameters: $a = 5.23$ Å, $b = 5.23$ Å and $c = 9.41$ Å resulting in a c/a ratio of 1.27. This phase, stable at very large values of compressive strain lies at around 146 meV/f.u above the R3c ground state and has a spontaneous polarisation of about 137.4 $\mu C/cm^2$ along the c direction.

Applying again the same procedure, we build supercells by doubling one of the in-plane lattice vectors (a or b) and/or the out-of-plane lattice vector (c) and identify several phases, reported in Tab. 3. In order to calculate the spontaneous polarisation for the different phases we compute the Born effective charges[3] for the P4mm phase and multiply each BEC matrix obtained by the displacement of the corresponding atom in the supercells[4].

Since in all the structures that we find, the in-plane lattice vectors correspond to highly-strained values of the R3c ones, we compute the energy of the Cc phase, reported to be the lowest energy phase at these lattice vectors [41], for different in-plane lattice values as a reference. We report the energy of the different phases as a function of the average in-plane lattice constant in Fig. 21a and see that most phases are close in energy to the reference structure.

[3]Note that we made this choice, which is different than what we did in Ref. [88], because of the large out-of-plane elongation.

[4]From the calculation in the P4mm phase we obtain one matrix for the Bi cations, one matrix for the Fe cations and two matrices for the O anions due to symmetry.

	Lattice parameters				Energies	Polarisation		
Phase	a [Å]	b [Å]	c [Å]	Angles [deg.]	Energy [meV/f.u.]	P_a [$\mu C/cm^2$]	P_b [$\mu C/cm^2$]	P_c [$\mu C/cm^2$]
Aem2 – (b)	5.26	10.49	9.39		156.23	0.0	0.0	135.4
Pma2 – (b)	5.24	10.48	9.39		147.06	0.0	0.0	135.9
Pma2	5.25	5.24	9.41		142.01	0.0	0.1	136.5
Ima2 – (c)	5.25	5.27	18.73		135.10	0.3	0.0	134.2
C2 – (c)	5.28	5.28	18.61	$\gamma = 90.33$	130.97	2.4	0.0	131.2
P2 – (c)	5.28	5.28	18.59		130.54	0.3	0.1	130.9
Ima2	5.26	5.30	9.31		124.68	0.3	0.0	131.9
Pc – (b,1)	5.26	10.58	9.40	$\alpha = 87.43$	124.48	0.1	32.5	132.3
Pc – (bc,1)	5.28	10.62	18.51	$\alpha = 89.99$	122.29	0.3	0.0	128.2
$Cmc2_1$	5.29	5.26	9.43		121.53	0.0	0.5	133.7
$Cmc2_1$ – (c)	5.29	5.26	18.85		120.32	0.0	0.0	133.1
Cm	5.27	5.29	9.43	$\alpha = 92.65$	119.03	0.1	33.0	133.0
Pc – (b,2)	5.29	10.59	9.38	$\alpha = 92.43$	117.29	0.1	29.6	130.9
Pc – (bc,2)	5.29	10.60	18.77	$\alpha = 87.42$	114.07	0.2	30.3	130.5
$P2_1$ – (c)	5.28	5.28	18.91	$\gamma = 91.58$	113.91	5.2	0.3	133.4

Table 3: Computed lattice parameters, energy compared to the R3c unstrained ground state, unit cell angles (if different than 90°), and polarisation along each lattice vector. Each phase stabilised from the P4mm parent structure is reported. Next to the symmetry of each phase we indicate along which axis the supercell was built using the letter of the unit cell vector (b) and (c) or two letters when doubled along two directions (bc). When phases share the same unit cell size and same symmetry, we distinguish them with an extra index next to the letter. The phases reported only with their symmetry have the same unit cell size as the P4mm parent structure, and were obtained by freezing in zone-centered phonon modes.

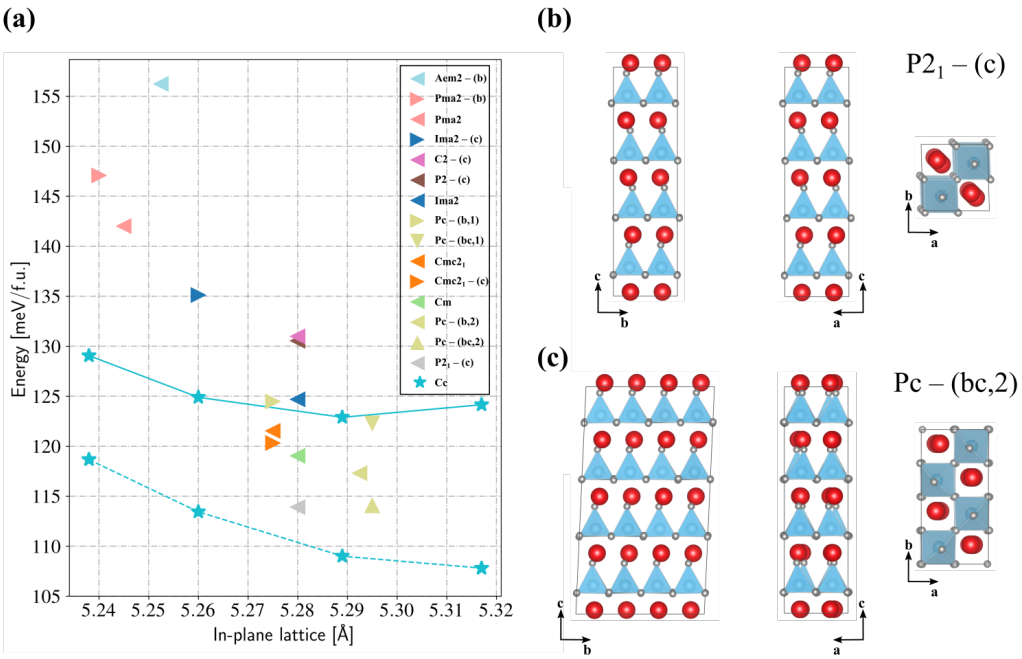

Figure 21: Phases obtained from supercells of P4mm. (a) Energy compared to the R3c ground state as a function of the averaged in-plane lattice constant for the different phases stabilised. The stars joined by continuous lines represent the Cc phase with in-plane lattice constant imposed and out-of-plane relaxed using the mapping from Ref. [41] and unrelaxed monoclinic angle. The angle is relaxed in the lower energy curve with stars joined by dashed lines. Phases with the same symmetry are represented by the same colour but a different marker. (b) Structure of the $P2_1$ – (c) phase projected along each direction. (c) Structure of Pc – (bc,2) phase projected along each direction.

Furthermore, we find that all phases reported in Tab. 3 display a large c/a ratio correlated with the large values of polarisation, found to range between 128 and 137 $\mu C/cm^2$ along the c direction. We also find that some phases have an in-plane component with non-negligible values of around 30 $\mu C/cm^2$.

While relatively high energy compared to the R3c ground state, some phases are actually competing with the Cc phase. In particular, we find that a phase with Pc symmetry (labeled Pc – (bc,2)) and 80 atoms per unit cell, is only 6 meV/f.u. above the reference phase for the same in-plane lattice constant. This phase has in-plane as well as out-of-plane polarisation and a monoclinic structure. Another phase with $P2_1$ symmetry (labeled $P2_1$ – (c)) has almost the same energy, but its smaller in-plane lattice constant makes the energy difference with the reference phase even smaller (see Fig. 21a). We present the structures of these two phases in Fig. 21b-c.

4.4 CONCLUSION

In summary, we demonstrated in this chapter that the phase space of BFO is much richer than was previously thought. Indeed, starting from only a few

known phases, we used phonon modes to look for other phases with larger unit cells and identified many with relatively low energy compared to the ground state. In the attached published manuscript (see Ref. [88]) we further discuss the stability of these phases under strain and electrostatic boundary conditions.

Beyond the published results, we identified other phases with even larger unit cells. Indeed, we found a phase with Cm symmetry and 160 atoms per unit cell exhibiting antipolar displacements of the Bi atoms and double tilts of the octahedra with larger periodicity and more complex patterns than the distortions present in $Pnma(1)$. We also discussed the existence of another series of structures with Pc symmetry and long lattice vector.

Finally, we showed that the phase space of BFO remains rich even for large values of compressive strain, small in-plane lattice vector. Indeed, starting from the $P4mm$ structure, we stabilise several phases with large c/a values and low energy compared to the Cc reference structure (lowest-energy phase for large compressive strain). Probably due to the large c/a ratio in this region of phase space, we only found phases that exhibit very large out-of-plane polarisation. It is then unlikely that at large compressive strain one could use the electrostatic boundary conditions at the interface between BFO and a non-polar III-III perovskite to induce a phase transition between phases with low energy above the Cc phase.

In the next chapter we will explore additional factors to the electrostatic boundary conditions.

Electrostatics and isosymmetric Phase Transition

5

Over the past decades, advances in growth techniques have made it possible to create materials with precise atomistic control. This exactness further enables the use of strain engineering to modify the properties of materials. Bismuth ferrite is an excellent example of the effect of epitaxial strain: Films of BFO grown under highly compressive strain exhibit a phase transition at around -4.5% strain from a monoclinic, nearly rhombohedral, phase (R-like) to a monoclinic, nearly tetragonal, phase (T-like). Under additional compressive strain, the T-like phase becomes truly tetragonal. At around -4.5% strain, the out-of-plane lattice parameter is highly elongated resulting in a large c/a ratio of around 1.25, and a change in Fe coordinations from six to five. Furthermore, the structural transition is accompanied by a large spontaneous polarisation of about 150 $\mu C/cm^2$ along the c axis.

In chapter 3 we showed that one can take advantage of the polar discontinuity at the interface between BFO and a III-III perovskite material (one with cations having formal charges of $+3$) to induce a phase transition from the polar ground state to a non-polar metastable phase. We saw in chapter 4 that for large compressive strain, different phases were found to be stable, with a large out-of-plane polarisation. We expect then that for large compressive strain and in the presence of a polar discontinuity, BFO will likely split into domains in order to avoid the polar discontinuity.

We show in this chapter that the scenario can be different when the (spontaneous) polar discontinuity is accompanied by a charge layer discontinuity. We use the example of BFO with doped Calcium manganite which is a bad metal and II-IV perovskite material (the A-site cation has formal charge $+2$ and the B-site formal charge $+4$) rather than III-III like BFO. This latter difference brings an additional discontinuity. This study is motivated by the experimental observations of our collaborators Nordlander et al. [95]: in heterostructures of $BiFeO_3$ / $Ce_{0.04}Ca_{0.96}MnO_3$ grown on $LaAlO_3$ (LAO) substrates, BFO grows as a single domain without critical thickness for the polarisation to be stable.

The reminder of this chapter is organised as follows. First, we will briefly review previous results on BFO under large compressive strain. Second, we will present the experimental results published by Nordlander et al. [95] and formulate the experimental outcomes that need to be addressed theoretically. We will then present our study, answering those questions and conclude the chapter as well as the second part of this thesis.

5.1 BFO UNDER COMPRESSIVE STRAIN

When BFO is forced to have square in-plane lattice, the rhombohedral structure (R3c) becomes monoclinic. Under tensile or moderate compressive strain, this monoclinic structure is close to R3c and is often referred as R-like phase. As we already mentioned, when the strain exceeds 4.5% of compressive strain, the in-plane and out-of-plane lattice vectors become significantly different resulting in a large c/a ratio of about 1.25. The structure is still monoclinic, but as it is close to a tetragonal structure, it is usually called the T-like phase in the literature.

While the transition from R-like to T-like was first thought to be isosymmetric, Christen et al. demonstrated that the transition path between rhombohedral and tetragonal actually involves a symmetry change from $\mathbf{M_A}$ (Cc symmetry) to $\mathbf{M_C}$ (Pm symmetry) [91]. While both are monoclinic, $\mathbf{M_A}$ is obtained by shearing the cubic perovskite cell along the $[110]_{pc}$ direction, while the $\mathbf{M_C}$ phase is obtained by applying shear along $[001]_{pc}$. Imposing the in-plane lattice constant of $YAlO_3$ (3.69 Å), the Cc phase was found computationally to be the lowest energy phase. It has a monoclinic angle of $\beta = 88.1$ and $a^-b^-c^0$ rotations [91]. The Pm phase was found to be low-energy and metastable with $\beta = 90°$ and $a^-b^0c^0$ rotations. Finally, the same study confirmed that at higher strain values (around 10% of strain), the P4mm tetragonal phase was stable and exhibited a c/a ratio of 1.41 and no octahedral rotations.

Thus we can summarise the phase transitions under strain from no strain to very large compressive strain as successive phase transitions between R3c (no strain and no matching to the substrate), Cc, Pm and finally P4mm (very large strain).

5.2 EXPERIMENTAL MOTIVATION

In order to better understand the behaviour of highly strained BFO in technologically relevant ultra-thin films, Nordlander et al. [95] study heterostructures of $BiFeO_3$ / $Ce_{0.04}Ca_{0.96}MnO_3$ (CCMO) grown on (001) $LaAlO_3$.

Using in-situ optical second harmonic generation (ISHG) [96] they probe the polarisation during growth and find that BFO is polar since the deposition of the first unit-cell. Furthermore, by continuously monitoring the polarisation and symmetry, they observe that until at least 80 unit cells, BFO adopts the tetragonal P4mm phase without monoclinic distortions and remains single domain. They further observe that under sample cooling, BFO goes through two phase transitions with a first transition at higher temperature in which the purely tetragonal phase develops a monoclinic tilt and a second transition at lower temperature where the monoclinic structure develops octahedral rotations to become R-like. Finally, Nordlander et al. investigate the robustness of the polarisation in the mono-domain tetragonal phase, by building a capacitor-like heterostructure, growing a capping layer of CCMO on top of 20 unit cells of BFO (CCMO / BFO / CCMO). They observe that the result of changing the electrostatic boundary conditions by capping the BFO layer is to reduce the

tetragonality of BFO going from a c/a ratio of 1.20 (without top electrode) to 1.17 with one layer of CCMO on top of it. This behaviour contrasts with the usual creation of domains resulting in no net polarisation, even for initially single domain structures.

Explanation of these experimental results requires theoretical inputs. In the rest of this chapter we will therefore address the following questions:

1. Why are the oxygen polyhedral rotations of the monoclinic T-like phase lost at lower temperature on heating than the ferroelectric distortion, resulting in the ideal tetragonal structure at the highest temperature of the growth process?

2. Why is no critical thickness observed for the sample to be polar, considering that there is a very large out-of-plane polarisation that results, if not compensated, in a large polar discontinuity?

3. Why does the c/a ratio decrease when a layer of CCMO is deposited on top of the BFO in the growth chamber?

5.3 ROTATIONAL AND POLAR MODES

The loss of polyhedral rotations at lower temperature than the ferroelectric distortion in the above mentioned experiment is in sharp contrast to that of rhombohedral and monoclinic R-like BFO, in which the Curie temperature for the ferroelectric polarisation is 1098 K, whereas the rotations persist to 1204 K [34].

In Fig. 22a we show our calculated structures and energies for the monoclinic T-like (Cc and Pm), tetragonal T ($P4mm$) and high-symmetry centrosymmetric ($P4/mmm$) phases, all with their in-plane lattice constants fixed to that of LAO found from DFT (3.77 Å). Consistent with earlier calculations [91], we find that the Cc phase is lower in energy than the Pm phase and therefore choose the Cc structure for the monoclinic T-like phase in our analysis. We find that the equilibrium monoclinic angle is $\beta = 87.32$ and the equilibrium c/a ratio is equal to 1.228 on LAO. Note that we use the same parameters as presented in section 3.2 for all the DFT calculations.

It is clear that the energy required to remove the rotations of the oxygen polyhedra from the T-like structure (65 meV/.f.u) is considerably lower than that to remove the ferroelectric distortion ($843 - 65 = 778$ meV/f.u.), consistent with the experimental observation of the relative stability of the phases.

To understand this behaviour, we use the ISODISTORT software [73, 74] to analyse the structural distortions that transform the high-symmetry $P4/mmm$ phase into the Cc phase. We find that the distortions can be decomposed into primarily four normal modes (see Fig. 22b), two polar modes – Γ_3^- which yields the $P4mm$ structure, and Γ_5^- which causes the in-plane polarisation of the Cc structure – and two rotational modes, A_5^- and A_4^-, that are responsible for the $a^-b^-c^0$ and $a^0b^0c^-$ rotations in Glazer notation respectively. In Fig. 22c we show the energy as a function of the mode amplitude, starting from the high-symmetry centrosymmetric $P4/mmm$ structure which is set to 0 eV, for each of

these modes in turn. We find that the Γ_3^- polar mode, which causes the polarisation along the vertical direction, lowers the energy substantially more than both rotation modes and the Γ_5^- polar mode. The persistence of the rotation-free polar tetragonal phase at high temperature is therefore consistent with the large energy scale associated with the polar mode.

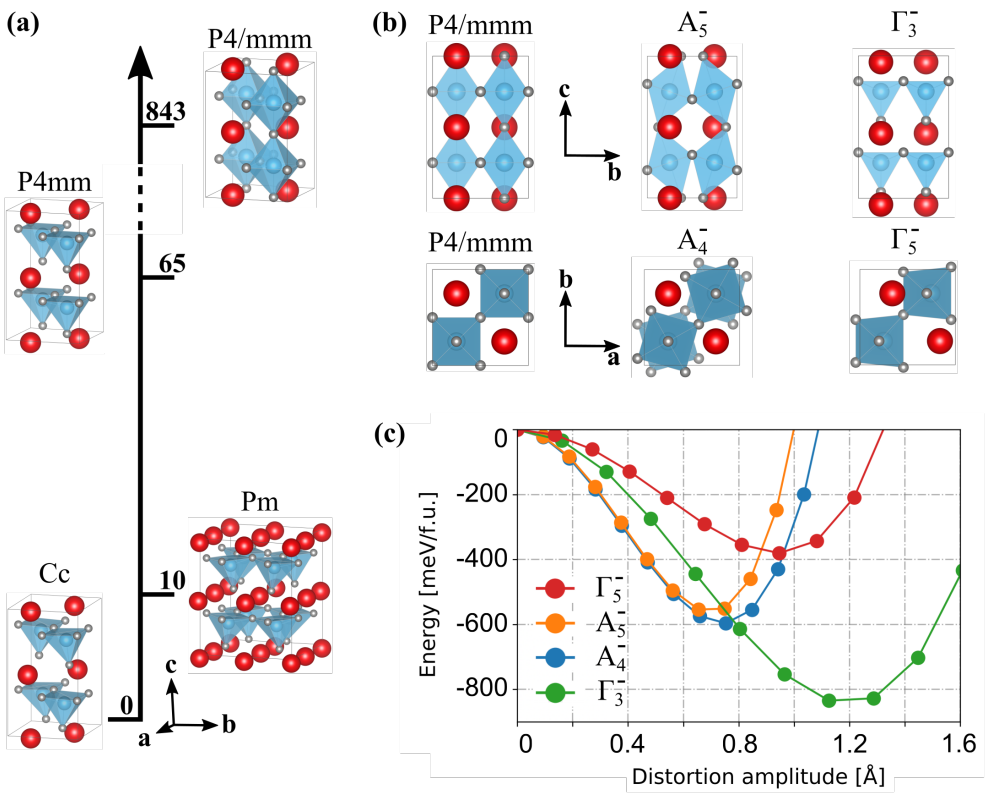

Figure 22: (a) Calculated DFT structures and relative energies of the P4/mmm, P4mm, Pm and Cc phases with in-plane lattice constants set to be equal to those of LAO substrate. (b) Distortions of the two rotation modes (A_4^- and A_5^-) and of the two polar modes (Γ_3^- and Γ_5^-) away from the tetragonal P4/mmm structure to the Cc one. All modes are individually frozen into the P4/mmm phase at the volume of the Cc phase to compute the energy. Each mode corresponds to an irreducible representation of the high-symmetry P4/mmm space group and is characterised by an amplitude normalised by the ratio between its volume and that of the high-symmetry phase.

5.4 ELECTROSTATICS AT THE INTERFACE WITH II-IV PEROVSKITE

Previously, we saw that the polar discontinuity at the interface between two materials is responsible for the creation of the depolarising field. In a material adopting the ABO_3 perovskite-oxide structure, the layers along the growth direction can be negatively or positively charged or neutral depending on the

chemical composition. For example, considering the usual $[001]_{pc}$ growth direction, BFO has alternative layers of BiO/FeO_2 resulting in $+1/-1$ charged layers respectively. While, the layer contribution does not need to be addressed in superlattices where the layers in both materials have the same formal charges, when the layer charges are different, they provide an additional contribution to the polar discontinuity. Thus, while the contribution from the charged layers was not relevant in chapter 3 and in chapter 4, it has to be considered in the BFO/CCMO superlattice.

Indeed, CCMO grown along the $[001]_{pc}$ direction has neutrally charged layers, resulting in a discontinuity at the interface with BFO. We have then to add to the bound charges coming from the spontaneous polarisation, those resulting from the discontinuity between the layer with $+|e|$ (BiO termination) or $-|e|$ (FeO_2 termination) per unit cell and the neutral MnO_2 or CeCaO layer, respectively. It is clear that depending on the orientation of the spontaneous polarisation and the terminations of the BFO layers the net bound charges resulting from both contribution can be larger or smaller at the interface.

As discussed by Efe et al. [97] the case of rhombohedral BFO is unusual because the polarisation coming from its uncompensated charged layer and its spontaneous polarisation projected along the direction perpendicular to the interface have accidentally the same magnitude. Indeed, on one hand, BFO has a spontaneous polarisation of around ~ 90 $\mu C/cm^2$ along the $[111]_{pc}$ direction, resulting in bound charges of about $\sim \pm 50$ $\mu C/cm^2$ on the $(001)_{pc}$ surface. On the other hand, the ionic charged layer results in a polarisation of $\pm\frac{1}{2}\frac{|e|}{a_0^2}$, with plus sign on the BiO surface and minus sign on the FeO_2 surface[1]. Taking a cubic lattice constant $a_0 = 4$ Å, we obtain the polarisation induced by the ionic charged layer to be ± 50 $\mu C/cm^2$ [42]. We can then combine both contributions and see that the bound charges are either $\sigma_{surf} = 0$ $\mu C/cm^2$ or $\sigma_{surf} = 100$ $\mu C/cm^2$ depending on the choice of surface and ferroelectric polarisation orientation, resulting in what Efe et al. call a happy or unhappy surface respectively [97]. The consequence of this is that in BFO, when the spontaneous polarisation and the termination are in the happy configuration, no external screening is necessary to make the surface or interface electrostatically stable.

We can qualitatively justify the absence of critical thickness (no depolarising field) during the growth of BFO on top of CCMO. Using the Born effective charges computed in the previous chapter (section 4.3.3) we obtain an out-of-plane component of the polarisation of 120 $\mu C/cm^2$ for the T-like phase. The ionic charged layer discontinuity can screen about half of the bound charges coming from the spontaneous polarisation. The rest of the screening likely comes from the bottom CCMO metallic electrode and the free ions in the chamber during growth [98].

[1] This result is obtain by simply considering a cubic unit cell and computing the net formal charge of each layer multiplied by its position along the vertical axis, setting the origin on the bottom of the unit cell.

5.5 REDUCTION OF THE c/a RATIO AND ISOSYMMETRIC PHASE TRANSITION

Assuming that the top surface of BFO is stabilised in the growth chamber due to the different screening contributions mentioned above, the deposition of the CCMO top electrode represents a change in electrostatic boundary conditions resulting in a reduction of the c/a ratio in BFO.

In order to understand this behavior, we consider the $P4mm$ and Cc phases at different c/a ratios. In Fig. 23 we show the energy of both phases as a function of the c/a ratio. Note that for the Cc phase we keep the monoclinic angle fixed to the equilibrium value reported above. We see that, while experimentally the tetragonal symmetry without monoclinic angle deviating from 90° is reported, in our calculations the Cc phase remains lower in energy at all c/a ratios. Furthermore, we find that the Cc curve displays an abrupt change at $c/a = 1.18$, where there is an isosymmetric phase transition between two phases with Cc symmetry. The experimental ratios of 1.17 and 1.20 are represented by vertical dashed lines in Fig. 23 and the structures corresponding to each ratio are displayed on each side of the figure. While sharing the same symmetry, at ratios lower than 1.18, the structures display $a^-b^-c^-$ rotations, and at ratios higher than 1.18 the rotations follow the $a^-b^-c^0$ pattern, as reported earlier [91]. This difference in rotations takes its origin in the amplitude of the $A4^-$ mode, which is large for smaller ratios and very low for larger ratios. Furthermore, this transition is accompanied by a drop in out-of-plane polarisation (see Fig. 23).

For a better comparison between the structures at the experimentally observed c/a ratios, we relax the monoclinic angle fixing the c/a ratio to 1.17 and find that the equilibrium angle at $c/a = 1.17$ is $\beta = 88.78$. The internal energy at a ratio of 1.20 is 5.5 meV/f.u. lower than it is at 1.17. The out-of-plane polarisation at 1.17 is equal to 93 $\mu C/cm^2$ and that at 1.20 is 118 $\mu C/cm^2$. Note that at the former ratio the polarisation has an in-plane component along the a axis equal to 55 $\mu C/cm^2$ and at the latter ratio the component along a is lower and equal to 32 $\mu C/cm^2$.

In the absence of electrodes, we estimate the planar electrostatic energy density, $E_{es} = \frac{1}{2}\frac{P^2}{\epsilon_r \epsilon_0}$, to be around 577 meV/f.u. at $c/a = 1.20$ and around 354 meV/f.u. at $c/a = 1.17$, taking the dielectric constant ϵ_r to be 55 and P the out-of-plane component of the polarisation. Considering the partial screening coming from the ionic charged layer, the electrostatic energy density lowers to 192 meV/f.u. and 77 meV/f.u. for $c/a = 1.20$ and $c/a = 1.17$ respectively. Note that at both ratios the $P4mm$ phase has higher energy and higher out-of-plane component of the polarisation.

We expect this electrostatic cost to be lower due the capping of the metallic CCMO on top and possibly defects at the interface, but it is clear that the difference of internal energy between the structures at both ratios is negligible compared to the difference of electrostatic energy. We conclude then that the reduction of c/a ratio in the experiment is due to the existence of an isosymmetric phase at lower ratio, relatively low energy and with a reduced out-of-plane

component of the polarisation resulting in a lower electrostatic energy cost and more favourable configuration in the absence of perfect screening at the top surface.

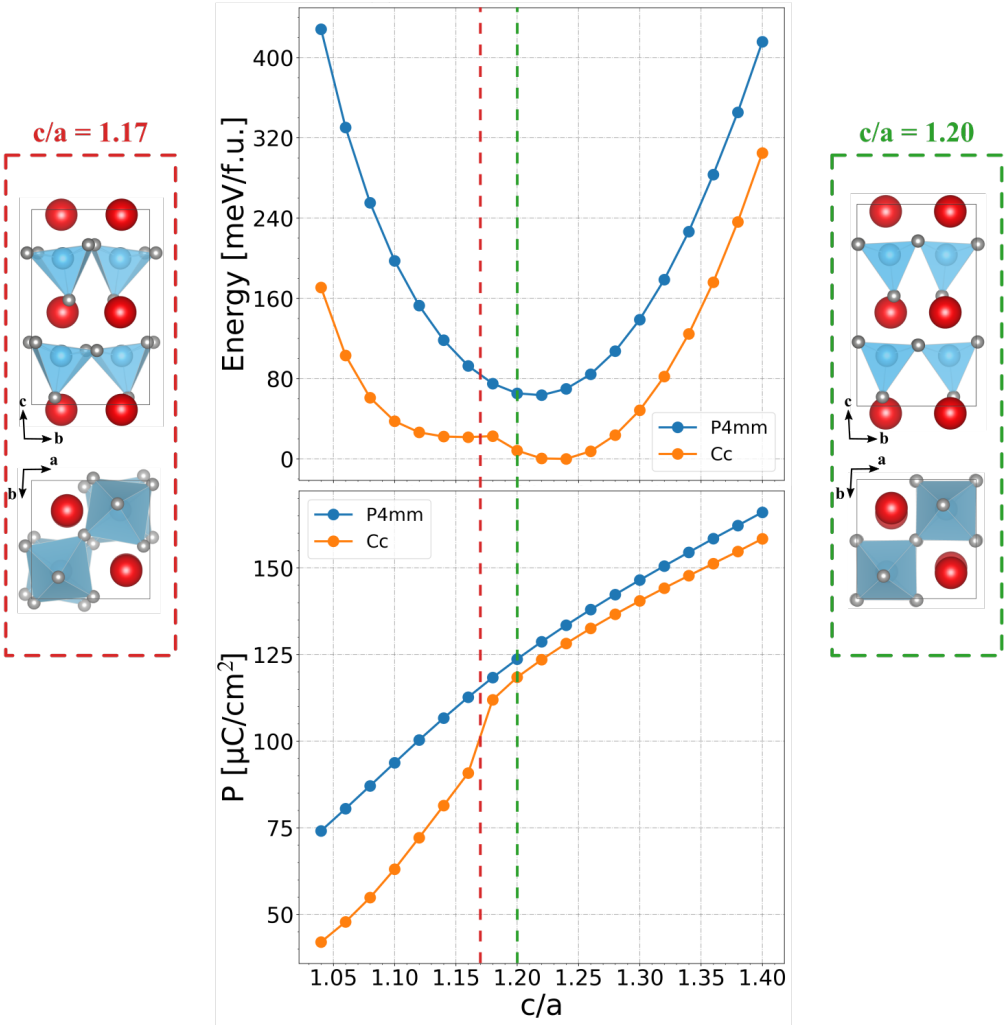

Figure 23: Calculated DFT energies and out-of-plane polarisation as a function of c/a ratio in the $P4mm$ (blue) and Cc (orange) phases. The vertical dashed lines represent the two c/a ratios observed experimentally and the corresponding structures are displayed on each side of the plots. For the Cc structures, we fix the monoclinic angle to $\beta = 87.32$ and vary the c/a ratio. The polarisation is calculated using the Born effective charges computed in the $P4mm$ phase.

5.6 SWITCHING PATH

We can approximate the energy cost to form domains by computing the energy barrier for the phase with polarisation in one orientation to switch to the opposite orientation. Our calculated energy barrier, along the minimum energy path,

computed using the NEB method as implemented in VASP [85–87], is shown in Fig. 24a. The NEB calculations were run until forces were below 0.05 eV/Å. We find that the energy barrier to switch the polarisation in the Cc phase at a ratio of 1.17 is about 300 meV/f.u., which is significantly larger than the energy barrier to switch traditional ferroelectric materials like $BaTiO_3$ (12 meV/f.u.) or $PbTiO_3$ (143 meV/f.u.) [99].

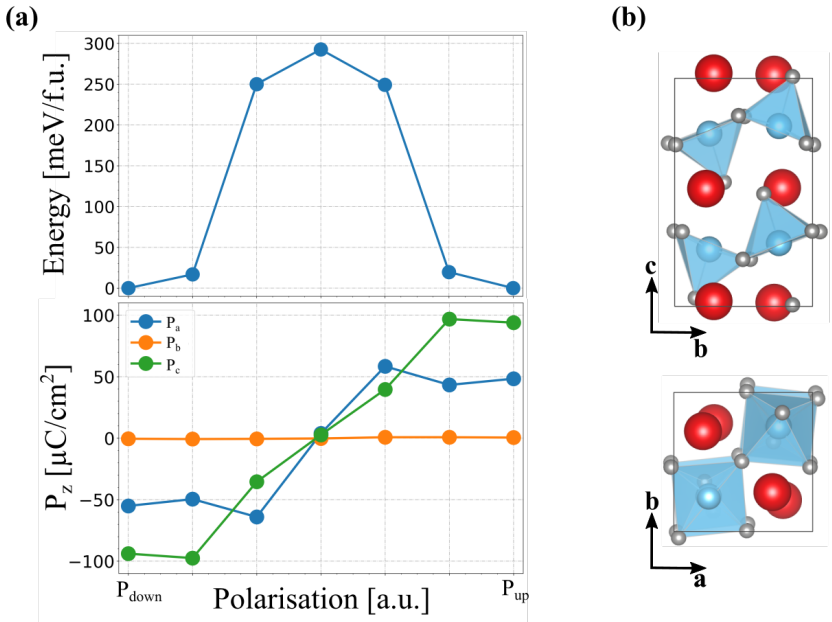

Figure 24: (a) Calculated energy barrier between two Cc structures at $c/a = 1.17$ with opposite ferroelectric polarisation obtained from a NEB calculation (top panel). The volumes of the structures along the distortion path are kept to the volume of the Cc phase at $c/a = 1.17$ with in-plane lattice parameters set to those of LAO. The corresponding evolution of the three components of the polarisation computed with the Born effective charges from the P4mm phase as shown in the bottom panel. (b) Structure at the top of the barrier in the minimum energy path.

The out-of-plane polarisation (along the c axis) evolves from -93 μC/cm^2 to 93 μC/cm^2 and is almost zero (2.7 μC/cm^2) at the center of the switching path. Note that this small deviation from a zero value can be attributed to the precision of the NEB calculation. While the polarisation along the b axis is null, its component along the a-axis also switches with the out-of-plane one (see Fig. 24a). The intermediate structure is displayed in Fig. 24b. Interestingly, while all the cations are displaced vertically along the positive direction of the c axis, the octahedra are elongated differently in each half of the unit cell, such that the Fe cations are five coordinated with the O anions upward or downward in each half of the cell.

Finally, we see that the energy to switch the polarisation (300 meV/f.u.) is larger than the electrostatic cost related to the polarisation in the absence of metallic screening (77 meV/f.u.). We conclude then that even if the bound

charges resulting from the large polarisation partially compensated by the ionic charged layers, are not screened by an external mechanism such as defects or mixed interface for example, the associated electrostatic energy cost remains lower than the cost for forming domains.

5.7 CONCLUSIONS

In this chapter we studied BFO under large compressive strain and surrounded by a metallic II-IV perovskite. We showed that, while in the rhombohedral phase the polarisation is lost before the octahedral rotations on heating, under large compressive strain, it is the other way around. We explain this behaviour by the large energy scale associated with the polar mode, lowering the energy substantially more than the rotational modes.

Furthermore, we addressed the stability of the polarisation in heterostructures against the depolarising field. It was shown experimentally that BFO in its T-like phase remains stable to domain formation during growth and under capping with a top metallic electrode. The absence of critical thickness during growth is attributed to the lowering of the density of bound charges at the interface due to the ionic charge layer discontinuity and possibly due to a combination between the screening provided by the metallic CCMO, the floating ions in the growth chamber and other mechanisms such as defects or mixed interface.

While stable during growth, when the electrostatic boundary conditions are modified by growing CCMO on top of BFO, a drop in polarisation and c/a ratio is observed. We discover in our calculations an isosymmetric phase transition between two structures with Cc symmetry, with a larger in-plane and smaller out-of-plane component of the polarisation at lower c/a ratio and a smaller in-plane and larger out-of-plane component at higher c/a ratio. The reduction of the electrostatic energy cost overcomes the small increase of the internal energy of the Cc phase between $c/a = 1.17$ and $c/a = 1.20$. We conclude then that the drop of c/a ratio observed experimentally is likely due to the minimisation of the electrostatic cost at the expense of the internal energy. Furthermore, we showed that the energy to switch the polarisation is larger than the electrostatic energy cost, which might contribute to the robustness of the polarisation in BFO to domain formation under large compressive strain.

In summary, we showed in chapters 3, 4 and 5 that the phase space of BFO is very rich, even richer than previously thought. Furthermore, while strain engineering has long been used to stabilise new phases, electrostatic engineering can also be important. Indeed, in chapter 3 we showed that the polar discontinuity disfavours the polar ground state over a non-polar polymorph with relatively low energy inducing a phase transition. In the current chapter we showed that, while the electrostatic cost related to the polar discontinuity coming from the spontaneous polarisation can be partially compensated by ionic charged layers and free charges coming from the metallic buffer, BFO likely undergoes an isosymmetric phase transition in order to decrease the electrostatic cost.

While we explored the influence of strain and electrostatics, we did not treat the influence of the octahedral mismatch at the interface between different materials. This contribution to the energy can be important if the octahedral distortions are significantly different between phases, in which case the imposition of a given tilt pattern in a few layers can destabilise one phase over another one. As octahedral tiltings are difficult to measure experimentally, computations could be particularly helpful. We could for instance address the influence of the octahedral mismatch by selecting a range of different substrates and impose their octahedral distortions on various low-energy phases of BFO. With the octahedra kept fixed, one could then relax the positions of the Bi cations and in that way estimate the mismatch cost.

Finally, we demonstrated in this part that in order to understand experimental results or to engineer new functionalities, it is necessary to have an accurate description of the phase space of BFO. This is particularly important for modern techniques such as second-principles methods, in which an effective potential based on first-principles data is created. Indeed, in order for the potential to be accurate, extra care should be taken at the DFT level to describe precisely the competition between low-energy phases. The several phases that we found suggest that many others still remain to be identified. We will come back to this question in the last part of the thesis.

Part III

RESULTS II: Bi,Fe AND O - BEYOND THE 1-1-3 CHEMISTRY

After having explored the phase space of $BiFeO_3$ and showed its richness, in this part we investigate new materials built from Bi_2O_3 - Fe_2O_3 heterostructures beyond the perovskite structure and chemistry. This study is motivated by experimental findings of a new multiferroic material at room temperature exhibiting net magnetisation and ferroelectricity.

Bismuth Hexaferrite

6

A long-sought goal in magnetoelectric multiferroic materials research is to control the magnetic properties using an electric field, energetically more efficient than using a magnetic field. While many multiferroic materials have been engineered through different mechanisms (see section 1.4), no material up to now displays large magnetisation and large ferroelectricity at room temperature.

Among all multiferroic materials, BFO remains arguably the most promising one, with large ferroelectricity and antiferromagnetic (G-type) ordering well above room temperature. While the DMI induces a canted magnetic moment resulting in weak ferromagnetism, the latter is too small for real applications. We showed in the previous part of this thesis that a large amount of low-energy polymorphs exist in $BiFeO_3$ and while the latter represents only a particular ratio (50%, 50%) of the parent BiO_2 and FeO_2 oxides, several other compositions (mainly at low FeO_2 ratio) were reported [100]. It is then likely that other phases with composition different than $BiFeO_3$ exist, while not yet discovered [101].

We present in this chapter the discovery of a novel room temperature multiferroic, bismuth hexaferrite, $Bi_6Fe_{32}O_{57}$, whose structure is composed of layers of Bi_2O_3 separated by slabs of γ-Fe_2O_3. This new material has a structure close to that of barium hexaferrite, $BaFe_{12}O_{19}$ and displays ferroelectric properties as well as a net magnetisation.

The remainder of this chapter is organised as follows. In the first part, we will present the experimental results obtained by our collaborators, by introducing the structure, discussing the stoichiometry and reporting the measured properties of $Bi_6Fe_{32}O_{57}$. In the second part we will investigate numerically the origin of the net magnetisation measured by discussing possible magnetic orders. We will then address the question of ferroelectricity by studying the possibility of switching the spontaneous polarisation in the structure and conclude the study by comparing the theoretical and experimental results.

This study is motivated by the experimental work of our collaborators Chen, Yang, Nelson et al. and part of the included results are currently under review [102]. The experimental results presented are the work of Chen, Yang, Nelson et al. who discovered and characterised the new material. The theoretical aspects of the project were first addressed by Martin Dahlqvist, who provided me with basic input files for the calculations as well as an initial guess for the structures. I further developed the theoretical side of the project by finding new stable structures and investigating the possible polarisation switching. I present here the results of my own work carried out under the supervision of Nicola A. Spaldin.

6.1 EXPERIMENTAL FINDINGS

While the Fe ions in $BiFeO_3$ are antiferromagnetically coupled due to the superexchange interaction, in spinel-structure maghemite (γ-Fe_2O_3) the ferrimagnetic ground state is composed of two opposing magnetic lattices that do not fully compensate each other due to the presence of Fe vacancies, resulting in a net magnetisation of about 2.5 Bohr magnetons per formula unit [103]. Motivated by this comparison, our experimental collaborators investigated the possibility of integrating Bi ions, with their $6s^2$ lone pairs, and γ-Fe_2O_3 into a single compound. Following this idea, they were able to stabilise a new multiferroic material grown as an epitaxial thin-film on a Al_2O_3 (0001) substrate. This structure exhibits a similar structure to the well-known barium hexaferrite ($BaFe_{12}O_{19}$) [104], with the $BaFeO_3$ layers replaced by Bi_2O_3 layers (see Fig. 25).

By comparing X-ray absorbtion spectra of the sample to those of reference samples of hematite (α-Fe_2O_3), magnetite (Fe_3O_4) and manghemite (γ-Fe_2O_3), a match with the latter was found, suggesting that the Fe ions have primarily the Fe^{3+} valence state. From the similarity with the barium hexaferrite structure, the determination of the valence state of the Fe ions and the observed periodicity of the structure, they deduced the stoichiometry to be $Bi_6Fe_{32}O_{57}$.

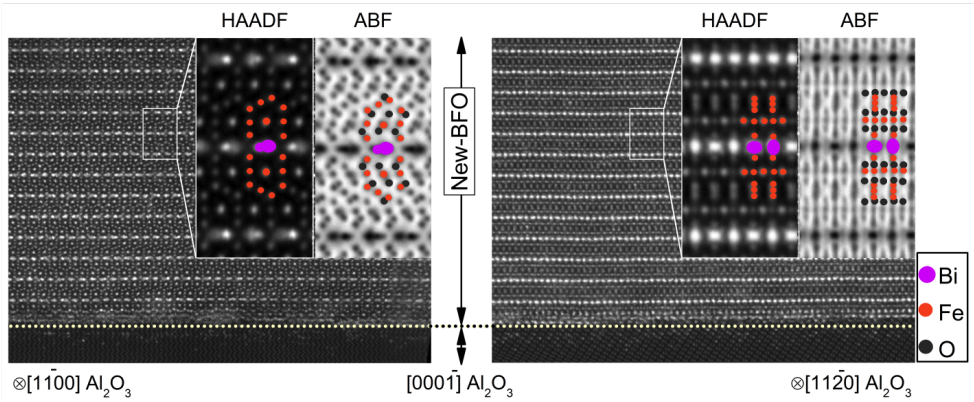

Figure 25: Z-contrast high-resolution scanning transmission electron microscopy (HR-STEM) imaged along perpendicular [1$\bar{1}$00] (left) and [11$\bar{2}$0] (right) directions designated by Al_2O_3 substrate axis. The insets present high-angle annular dark field (HAADF) and annular bright-field (ABF) images, respectively on the left and right hand-side of each inset. Schematics are shown in the insets with bismuth, iron and oxygen. Images adapted from [102]. Courtesy of Chris Nelson and Pu Yu.

While the design strategy to construct this new multiferroic material is based on the ferroelectric properties coming from the Bi ions and the ferrimagnetic character of the manghemite, both functionalities need to be measured to confirm that the $Bi_6Fe_{32}O_{57}$ structure inherited the properties of its parent compounds. Under the application of an external voltage through an AFM tip, our

collaborators were able to switch the polarisation. Furthermore, they measured the magnetisation to be around 0.3 μ_B/Fe, significantly larger than the canted moment in BFO, at room temperature.

The aim of our study is twofold. First, we want to provide more insight into the possibility that this new material is not only polar but also ferroelectric. Second, we want to investigate the possible origin of the net magnetisation, in particular to determine wether it is due to a larger canted moment than that in regular BFO, or if Fe vacancies resulting in an uncompensated AFM order can be the cause.

6.2 COMPUTATIONAL DETAILS

The calculations are performed using VASP [64–67]. The projector augmented wave (PAW) method is used [68, 69] with explicit treatment of the following valence electron configurations: $5d^{10}6s^2 6p^3$ for Bi, $3p^6 3d^7 4s^1$ for Fe and $2s^2 2p^4$ for O. A $3 \times 3 \times 1$ k-point Γ-centered Monkhorst-Pack mesh [70] is used to sample the Brillouin-zone of all unit cells considered and an energy cutoff of 700 eV for the plane wave basis is chosen. For the xc functional we use LDA and the Dudarev approach to DFT+U [71] is used to approximate electronic correlation in the Fe d orbitals. Note that within this formalism the on-site Coulomb (U) and the exchange (J) parameters are spherically averaged into a single effective interaction parameter $U_{eff} = U - J$. Reported results are obtained using $U_{eff} =$ 5 eV.

In Fig. 26a we show the starting structures that we used and in Fig. 26b we present the different magnetic orders considered in our calculations. Note that while usually the term ferrimagnetic is used to design two sub-lattices of magnetic moments with different magnitudes, here we use it to refer to two sub-lattices in which the individual magnetic moments have the same size, but the number of up and down spins is not equal. We start from the structure of $Ba_2Fe_{24}O_{38}$, substitute the Ba and Fe ions in the same layer by Bi ions to obtain $Bi_4Fe_{22}O_{38}$ and create supercells of $(Bi_4Fe_{22}O_{38})_3$ (192 atoms) and $(Bi_4Fe_{22}O_{38})_4$ (256 atoms) with $P6_3/mmc$ symmetry. In order to preserve the charge balance with Fe^{3+} ions, we remove 6 and 8 electrons from the former and latter supercell respectively. This is done by creating two Fe vacancies in the former supercell resulting in 190 atoms (see Fig. 26c) and by imposing a background charge of 8 electrons in the latter supercell (256 atoms). We then displace the Bi atoms in different directions to start from several initial configurations and relax the ions keeping the volume fixed to the experimental one.

The polarisation is estimated by multiplying the formal charge of each atom type (+3 for Bi, +3 for Fe and −2 for O) by its displacement vector with respect to the centrosymmetric (undistorted) structure. In order to keep charge neutrality, in the 256-atom cells we use a formal charge of 2.909 instead of 3 for the Fe atoms. That correction is not necessary for the structures with 190 atoms, as they are charge neutral.

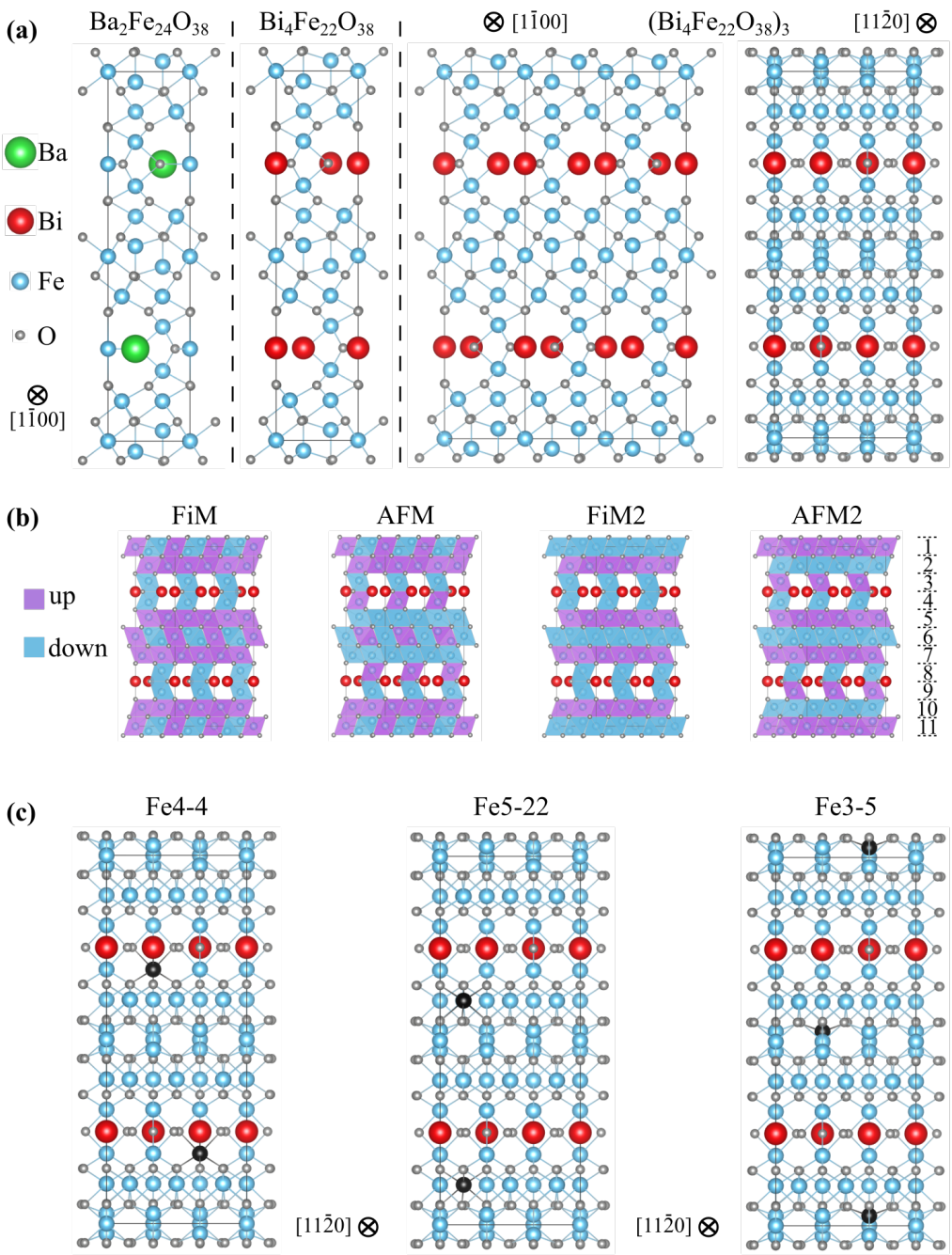

Figure 26: (a) Structure of Ba-hexaferrite and Bi-hexaferrite. From left to right, we show the $Ba_2Fe_{24}O_{38}$ structure, the analogous $Bi_4Fe_{22}O_{38}$ starting structure and finally a 192-atom supercell generated from three times $Bi_4Fe_{22}O_{38}$ with $P6_3/mmc$ symmetry (non-polar). (b) Different magnetic configurations used in the calculations. FiM stands for ferrimagnetic, where the numbers of up and down magnetic moments are not equal; AFM indicated that the numbers of up and down spins are the same. The numbers on the right label each layer of the structure for further reference. (c) Three structures each with two Fe vacancies. We start from the extreme right figure in (a) and remove two Fe ions at different sites. The atoms removed are indicated in black. Note that in the case of Fe3-5 the top and bottom vacancy are the same atom by periodicity.

6.3 STRUCTURES AND MAGNETIC ORDERS

As presented in the methods section, we consider two types of supercells: 190-atom cells from which two Fe ions have been removed, and 256-atom cells in which we set a background charge to guarantee the neutrality. We will refer to the former type of cells as the "vacancy case" (labeled according to Fig. 26c) or 190-atom cells, and to the latter type of cells as the "charged background case" or 256-atom cells.

We start our study by looking at the stability of polar distortions in the material. We impose the FiM order on the three vacancy cases and observe that vertical displacement of the Bi atoms is stable in each of the considered cases resulting in a net vertical displacement of the Fe after relaxation. As the symmetry was initially broken by construction due to the vacancies, we consider the charged background system in order to separate the effect of the polarisation introduced by vacancies from that introduced by the polar deformations. In the latter system, we also observe a polarisation coming from the vertical displacement of the Bi and Fe cations. We present the structures and polarisations in the following section.

Next we investigate the stability of the different magnetic orders presented in Fig. 26b and show the results of the energy and magnetic moment for different supercells in Table 4. In all cases, we find that the energy difference between FiM and AFM is very small whereas the two other orders are significantly higher in energy. The difference between FiM and AFM (FiM2 and AFM2) is that in layers $3, 4$ ($8, 9$) have opposite orientation of the magnetic moments in the AFM case and the same orientation of the magnetic moments in the FiM case. Furthemore, while the magnetic moments are oriented in the same direction within each layer in the FiM2 and AFM2 cases, the orientations are alternating within layers $1, 6$ and 11 in the FiM and AFM cases. From the energy comparison in all cases, we can deduce that it is energetically more favourable to have antiferromagnetic coupling within layers $1, 6$ and 11 and between these layers and the neighboring layers.

In the charged background case, while the AFM order is lower in energy, the energy difference from the FiM order is so small that they could be arguably equally favourable. We further investigate the AFM order, to determine if the AFM configuration displays any canted moment. Including spin-orbit coupling in our calculation we find that the easy axis is along the vertical direction with all moments perfectly aligned along that direction. From the vacancy cases, we see that the FiM or AFM can be stabilised depending on the position of the vacancy but the energy difference between them remains relatively small.

We can then conclude that the origin of the net magnetic moment observed experimentally is likely related to uncompensated magnetic moments due to the presence of vacancies as it is the case in γ-Fe_2O_3.

	FiM	AFM	FiM2	AFM2
Charged background				
Energy [meV/Fe]	0.43	0	41.91	41.44
Magnetic moment [μ_B/Fe]	1.16	0	0.38	0
Fe vacancy (Fe4-4)				
Energy [meV/Fe]	0	1.38	43.87	45.26
Magnetic moment [μ_B/Fe]	1.32	0	0.52	0
Fe vacancy (Fe5-22)				
Energy [meV/Fe]	0.29	0	42.33	41.95
Magnetic moment [μ_B/Fe]	1.06	0	0.26	0
Fe vacancy (Fe3-5)				
Energy [meV/Fe]	0	0.14	20.32	20.42
Magnetic moment [μ_B/Fe]	1.33	0	0.53	0

Table 4: Energy and magnetic moment for four different magnetic orderings for the lowest-energy structure with charged background (256 atoms) and the three vacancy cases (190 atoms) presented in Fig. 26. For each structure, the lowest-energy magnetic configuration is taken as the energy reference.

6.4 POLARISATION AND SWITCHING ENERGY BARRIER

As we saw that the FiM order is either the ground state magnetic configuration (Fe4-4 and Fe3-5) or very close in energy to the AFM ground state (charged background case and Fe5-22) we fix the FiM ordering in all the following calculations and present here the polar distortion in the different systems under study.

In Fig. 27a we present the structures of different candidates in the charged background case. We identify three stable structures, all very close in energy with less than 2 meV/Fe energy difference between them. These structures are reached from the $P6_3/mmc$ by adding polar distortions along the vertical axis that result in a lowering of the energy and a net polarisation along the z direction. We note that in all cases, even in the absence of Fe vacancies, the stable structures are polar with Cc symmetry and a spontaneous polarisation along the vertical direction of the order of $2-3$ $\mu C/cm^2$. Note that the in-plane polarisation is zero or very small (smaller than 0.1 $\mu C/cm^2$) in all cases. By decomposing the contribution to the polarisation coming from the different layers we see that, in the charged background case, the Bi layers and the Fe blocks contribute equally to the polarisation.

In Fig. 27b we present the structures of the three candidates with Fe vacancies considered earlier. While we see that the Bi layer contributes to the polarisation in all vacancy cases considered, we notice that the contribution of the Fe blocks depends strongly on the position of the vacancies. For instance, while the Fe blocks contribute almost nothing to the polarisation in the Fe4-4 case, they

dominate in the Fe5-22 case. Furthermore, the amplitude of the spontaneous polarisation along the vertical axis is also influenced by the position of the Fe vacancies and displays a larger range of values (from 1.26 to 3.40 $\mu C/cm^2$) compared to the more homogeneous charged background case. Note that in experiments any Fe vacancies would likely be disordered, unless there are prefered sites, and thus not contribute to the net polarisation. If we remove the effect of the vacancies we obtain net polarisation values between 1.11 $\mu C/cm^2$ and 3.36 $\mu C/cm^2$.

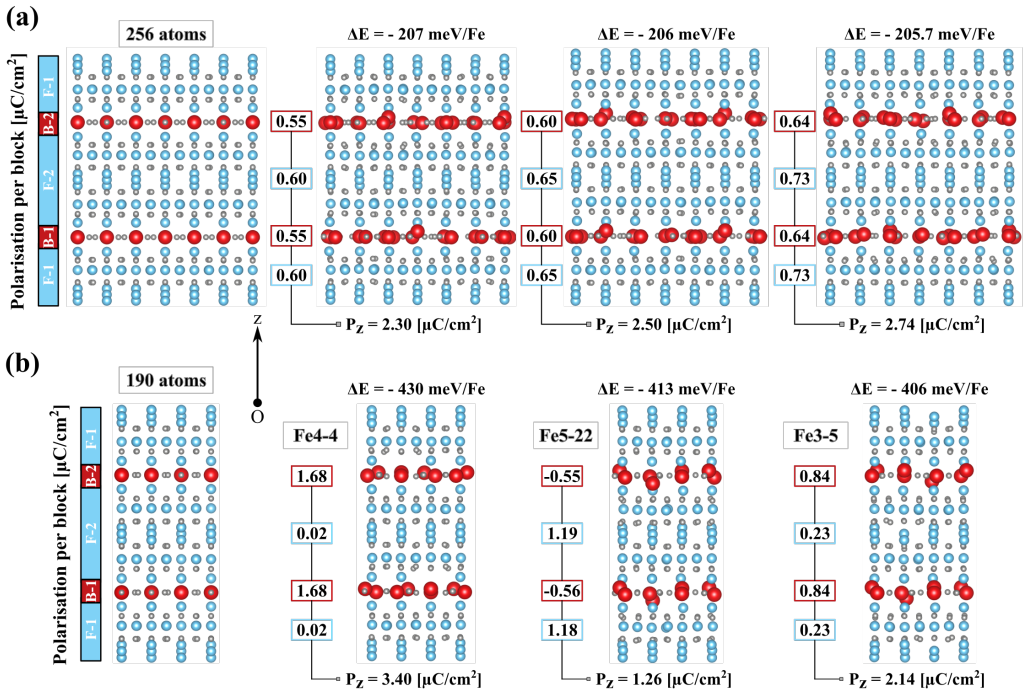

Figure 27: Structures and polarisations for different Bi-hexaferrite candidates. (a) Low energy structures computed using a charged background (256 atoms). The energies are reported relative to the non-polar high-symmetry reference structure (left). We report the polarisation per block (in [$\mu C/cm^2$]) as indicated on the left of each row. (b) Low energy computed structures with two Fe cations removed (190 atoms). For each structure, the energy is reported relative to the reference undistorted structure with the corresponding defects. All structures are viewed along [11$\bar{2}$0]. The polarisation is computed along the vertical axis, by taking the sum over the product of the formal charges and distortions with respect to the undistorted reference.

Having showed that the structure favours polar displacements, we next address the question of ferroelectricity. As a reminder, a polar material is ferroelectric if it is switchable by applying an electric field. As the intensity of the electric field required to switch the polarisation is directly related to the energy barrier, we will compute the latter.

The calculated energy barriers along the switching paths are computed using the nudged elastic band (NEB) method as implemented in VASP. Due to the

very large size of the systems, we run only coarse NEB calculations with a low convergence threshold of 0.2 eV/Å for the forces, resulting in an overestimation of the energy barrier. We initialise the switching path by interpolating between a starting structure with polarisation up and a structure with polarisation down obtained as follows: For the charged background cases, the down-polarisation structure is simply obtained by inverting each coordinate of the original structure. For the structures with Fe vacancies, in order to keep the vacancies in the same position in the lattice, we construct the down-polarisation structures by inverting the distortion vector with respect to a high-symmetry undistorted reference structure (with Fe vacancies at the same sites) and the structure with up-polarisation. The coordinates in all the down-polarisation structures are constrained to remain in P_{down} and optimised before starting the NEB calculation.

In Fig. 28 we present the switching barrier for one structure with charged background and one structure with Fe vacancies. In the charged background case, the double well is symmetric because the non-distorted reference structure has an inversion center and also because the structures at both minima are symmetry equivalent. We find an energy barrier of about 18 meV/Fe to switch the polarisation from 2.3 $\mu C/cm^2$ to -2.3 $\mu C/cm^2$ along the vertical direction (Fig. 28a). In the vacancy case, the double well is asymmetric because the reference structure does not have an inversion center due to the vacancies and because the two structures are different. We obtain in that case an energy barrier of around 42 meV/Fe to switch the polarisation from 2.14 $\mu C/cm^2$ to -10.3 $\mu C/cm^2$.

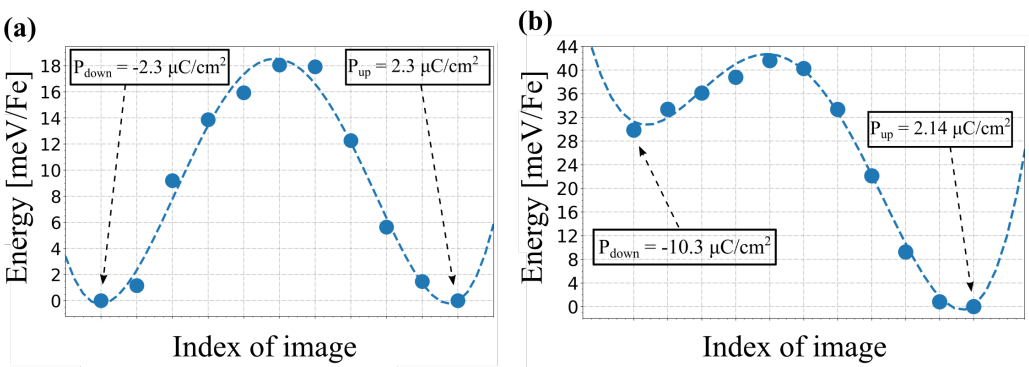

Figure 28: (a) Switching energy barrier for the lowest energy structure obtained with a charged background. (b) Switching energy barrier for the Fe3-5 vacancy case. The dots are the results of a NEB calculation and the dashed lines are an interpolation of the data with a polynomial of degree 4.

6.5 CONCLUSION

In summary we studied numerically $Bi_6Fe_{32}O_{57}$, which has been identified experimentally to be ferroelectric and to display a net magnetisation. In or-

der to decouple from the polarisation the effects of the choice of Fe site for vacancies, we considered supercells with the right stoichiometry and Fe vacancies, and supercells without vacancies. We conclude that the net magnetisation likely comes from uncompensated magnetic moments between two magnetic sub-lattices, due to the presence of Fe vacancies. Furthermore, we observe that in all the supercells considered (with and without Fe vacancies), polar distortions are driven by the out-of-plane movement of the Bi cations and the energy barrier to switch the polarisation is reasonably low suggesting that this material could be a good ferroelectric candidate.

While our simulations are consistent with the experimental findings, we believe that we capture the characteristics of this new material qualitatively but likely not quantitatively. Indeed, we expect that the vacancies are disordered in the experiments, while we consider only certain ordered configurations. This difference is certainly noticable in the absence of contribution of the Fe cations to the polarisation.

Furthermore, we identify several structures with very similar internal energy and observed that in the case of structures with Fe vacancies, different orientation of the polarisation can lead to structures with different internal energy. This let us believe that when an electric field is applied to switch the polarisation, a different structure with different properties can be stabilised.

Finally, this study suggests that the Bi-Fe-O oxides phase space should be further explored in order to discover new materials, possibly as interesting as $BiFeO_3$ while overcoming certain of its limitations such as the absence of net magnetisation. We hope that the discovery of $Bi_6Fe_{32}O_{57}$, will motivate further theoretical and experimental studies in this direction.

Part IV

RESULTS III: BEYOND DFT

In this last results Part we come back to the phase space of $BiFeO_3$. In Part II, we identified several phases in larger unit cells than the usually considered 20- to 40-atom unit cells. While the approach presented in chapter 4 was successful, it became computationally expensive for large unit cells. In this last Part we demonstrate a combination of DFT and machine learning that accelerates the discovery of new phases.

7 Revisiting the phase space with Machine Learning

In chapter 4, we explored the phase space of BFO iteratively. Starting from metastable phases, we increased their unit cell size and looked for unstable phonon modes related to structural distortions that lower the internal energy. This was made possible using the frozen phonons method, which is computationally very expensive and becomes particularly inefficient for large unit cells and low symmetry space groups. Indeed, this procedure requires us to carry out several single-point calculations (three per inequivalent site) for each starting supercell. While this thorough investigation led to the identification of several low-energy phases, it resulted in a large amount of unfruitful calculations when the initial structure was already stable.

On the other hand, we saw that it is convenient to describe the different phases that we identified in term of their structural distortions that transform a high-symmetry phase into the considered one. Furthermore, the distortions can be decomposed into normal modes and in general only a few modes are required to describe the phases accurately.

In this chapter, we propose a method to accelerate the discovery of phases using machine learning to predict the potential energy surface of BFO as a function of distortion modes. We take the opposite approach to that of chapter 4, in the sense that instead of starting from phases we start from distortion modes. Indeed, we create around $10,000$ structures by combining together different distortions with randomly chosen within an allowed range of amplitudes, compute the corresponding energy through a single-point DFT calculation, and use these data as training set to fit a machine learning (ML) model. Once our ML model is well trained, we use it to predict the energy of around $460,000$ structures and select the 290 lowest-energy phases to be fully relaxed.

The remainder of this chapter is organised as follows. First, we present the technical details of the DFT calculations and ML regression. Second, we explain how the distortion modes that will be used as building blocks are prepared. We then present the general workflow of our method and show the accuracy of our ML model. Finally, we present different phases obtained with this method and discuss possible improvements of the current approach before concluding.

This project was done in collaboration with Aria Mansouri Tehrani. I conceived the project, built the workflow and created the training set and Aria Mansouri Tehrani created the machine learning model.

7.1 COMPUTATIONAL DETAILS

The DFT calculations are performed using VASP [64–67] with the PAW method [68, 69] and explicit treatment of the following valence electron configuration: $6s^2 6p^3$ for Bi, $3d^7 4s^1$ for Fe and $2s^2 2p^4$ for O. A $8 \times 8 \times 6$ k-point Γ-centered Monkhorst-Pack mesh [70] is used to sample the Brillouin-zone of a 20-atom unit cell and an energy cutoff of 700 eV for the plane wave basis is chosen. For the xc functional we use PBEsol [53] with an effective Hubbard-like correction, $U_{eff} = 4$ eV, for the Fe d orbitals according to Dudarev's approach [71]. G-type antiferromagnetism is adopted for all the calculations.

The machine learning model is created based on a Support Vector Machine Regression (SVR) method [105, 106] as implemented in the Scikit-learn [107] library. We use a SVR model with a radial basis function (RBF) as kernel function with the parameters[1] C and γ. We generate $9,569$ data points with DFT and split the data into training set (80%, $7,655$ data points) and test set (20%, $1,914$ data points). We further perform a 5-fold cross-validation scheme which consists of choosing a set of parameters (C and γ), fitting the model on 80% of training set ($6,124$ data points) and evaluating its score on the remaining 20% of the training set (validation set, with $1,531$ data points). This procedure is repeated five times by changing the data going to the training set and validation set and making sure that each data point goes once to each set. The score obtained for the model with the set of C and γ parameters is then averaged over the 5 repetitions and different parameters are tested to find the optimal ones. We finally select the best parameters and evaluate the model on the test set ($1,914$ data points). We found best performance of the model with $C = 10$ and $\gamma = 1$.

7.2 DISTORTION MODES AS BUILDING BLOCKS

A convenient way to characterise and describe phases is to use the concept of irreducible representations (irrep) in which the distortions are decomposed into a set of normal modes that transform a reference structure into the considered phase. Usually, for perovskites the irreps are given as a decomposition of the $Pm\bar{3}m$ high-symmetry structure. Indeed, as it is the common parent structure to all phases, it allows direct comparison between the structures. Moreover, different phases can share the same distortion modes but not necessarily with the same amplitudes. For instance, we saw in chapter 4, that modes such as R_5^-, M_2^+ or X_5^- are common to several phases of BFO, nevertheless due to their different amplitudes and combined with the rest of the distortions the resulting structures differ.

[1] From Scikit learn: *"Intuitively, the gamma parameter defines how far the influence of a single training example reaches, with low values meaning 'far' and high values meaning 'close'. The C parameter trades off correct classification of training examples against maximisation of the decision function's margin. For larger values of C, a smaller margin will be accepted if the decision function is better at classifying all training points correctly. A lower C will encourage a larger margin, therefore a simpler decision function, at the cost of training accuracy."*

Irrep	Wave vector $[\pi/a]$	Unit cell size	Remark
Γ_4^-	$[0,0,0]$	111	Polar, three orientations
X_5^-	$[0,0,1/2]$	112	Antipolar, two orientations
$\Delta_5^-(24)$	$[0,0,1/4]$	114	Antipolar, two orientations
$\Delta_5^-(48)$	$[0,0,1/4]$	114	Antipolar+Rotational, two orientations
M_2^+	$[1/2,1/2,0]$	111	Rotational
$R_5^-(12)$	$[1/2,1/2,1/2]$	112	Tilted, two orientations
$R_5^-(24)$	$[1/2,1/2,1/2]$	112	Tilted+Rotational
$T_2(12)$	$[1/2,1/2,1/4]$	114	Rotational
$T_2(24)$	$[1/2,1/2,1/4]$	114	Rotational
S_1	$[1/2,1/4,1/4]$	122	Antipolar
S_2	$[1/2,1/4,1/4]$	122	Antipolar
Σ_2	$[1/4,1/4,0]$	121	Antipolar
$\Sigma_3(24)$	$[1/4,1/4,0]$	121	Antipolar
$\Sigma_3(48)$	$[1/4,1/4,0]$	121	Antipolar
Λ_3	$[1/4,1/4,1/4]$	124	Antipolar

Table 5: List of the distortion modes used as building blocks, given as a decomposition of the $Pm\bar{3}m$ phase. For each distortion mode we give its irrep, its wave vector relative to the Brillouin zone of the $Pm\bar{3}m$ phase of volume a^3 and the minimal unit cell size of the corresponding structure, where 111 corresponds to a unit cell of size $\sqrt{2}a \times \sqrt{2}a \times a$ and 112 to one of size $\sqrt{2}a \times \sqrt{2}a \times a$. Note that we make the distinction between irreps with the same symmetry by indicating in parenthesis the corresponding symmetry index. Furthermore, for each mode we give the type of distortion present and indicate if the distortion is considered along different directions. The distortions can be linked to the displacements of the Bi or Fe cations that can be either polar when resulting in a net polarisation or antipolar when they have opposite and compensated polar displacements. They can also be related to the distortions of the oxygen octahedra and are labeled as rotational if they consist of a displacement of the O anions around the vertical axis, or tilted when the axis of the octahedra along the vertical direction changes its orientation. Note that $\Delta_5^-(24)$, $R_5^-(12)$, $T_2(12)$ and $\Sigma_3(24)$ correspond to the modes with same symmetry presented in Ref. [88], with symmetry index here.

As each mode consists of a distortion pattern of the different atoms, the combination of different modes can result on one hand in a lowering of the energy if the relative positions of the different cations and anions are electrostatically favourable and on the other hand to unstable structures, if for example the distance between anion and cation becomes too small. In principle, new phases could be guessed if one selected a compatible set of modes with appropriate amplitudes. While the number of possibilities is prohibitively large to make a good guess, we can construct a machine learning model able to predict the energy of a given combination of modes with certain amplitudes. We need then to first select the modes that we want to include and prepare their corresponding structures.

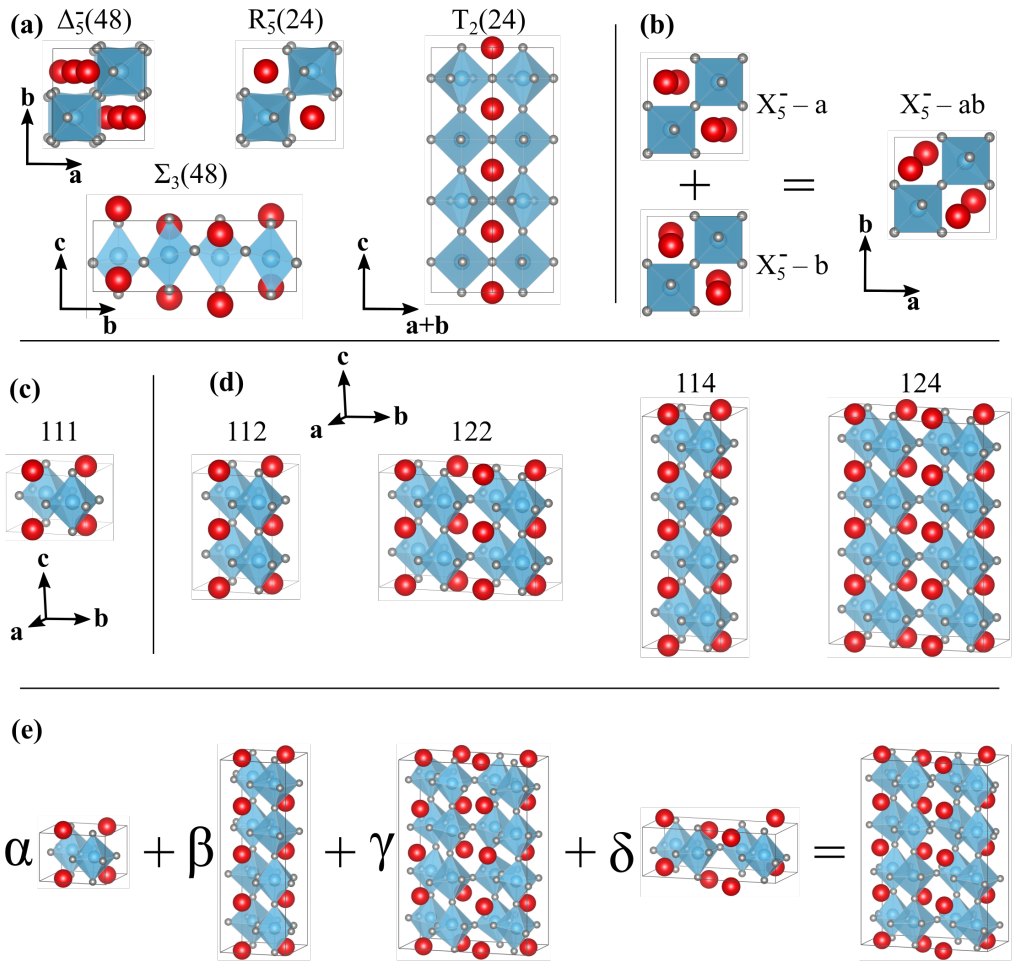

Figure 29: (a) Structures of different modes. $\Delta_5^-(48)$ and $R_5^-(24)$ display rotations along c additionally to the antipolar displacements along a and tilt respectively. $\Sigma_3(48)$ displays antipolar polar displacements. $T_2(24)$ has four different rotation angles, with two large angles and two very small ones. (b) Structures with the X_5^- mode along different orientation. (c) Basic cubic unit cell labeled 111. (d) Possible supercells. Each cubic supercell is constructed from (c) multiplied along different directions and labeled accordingly. (e) Example of a combination of four modes to build a structure. All structures of the modes are scaled to the size of the structure of the third mode and for each mode we create a distortion vector capturing the displacement from the 114 structure from (d) and the considered mode. Each vector is then multiplied by the corresponding amplitude factor (α, β, γ or δ) and the vectors are summed to give the final structure.

In order to be exhaustive, we extract all the different modes present in the phases identified in Ref. [88]. In Table 5 we present the list of the different modes used as building blocks. We consider in total 21 possible distortions: the 11 modes presented in Fig. 2 from Ref. [88], 4 new modes presented in Fig. 29a and different orientations of certain modes as illustrated in Fig. 29b (6 additional distortion modes). We show an example in Fig. 29b of the X_5^- mode reported to have different orientations in Table 5. We take the linear combination of the structure of the mode with two different orientations (along a and along b) and

obtained a structure where the distortions are along ab. While the structures with the distortion along a and b have the same energy, the new structure with the distortions along the diagonal of the unit cell has a different energy and can then be consider as a building block, keeping the uniqueness of the different starting structures. Using symmetry considerations we reduce the unit cell size of each distortion mode to its minimal size and fix the volume to that of the basic unit cell containing 10 atoms (displayed in Fig. 29c) scaled to the size of the considered mode's structure. Furthermore, we normalise all the modes such that the sum of the displacements multiplied by $\sqrt{V_p/V_s} = 1$ Å, equivalent to a mode amplitude of 1, where V_p and V_s are the primitive and supercell volumes respectively.

Structures of different modes. $\Delta_5^-(48)$ and $R_5^-(24)$ display rotations along c additionally to the antipolar displacements along a and tilt respectively. While $\Sigma_3(24)$ displays pairs of antipolar displacements along c, $\Sigma_3(48)$ is antipolar but without pairs. While $T_2(12)$ displays double rotations, $T_2(12)$ has four different rotation angles, with two large angles and two very small ones. (b) Distortions along different orientations. We show examples of the modes reported to have different orientations in Table 5, where we take linear combinations of displacement along the lattice vector. For example we build the antipolar $\Delta_5^-(48)$ by taking the superposition of the antipolar displacement along a and b, or similarly, the polar mode can be expressed along a or b equally. As we want each mode to be unique in term of energy, we add to our set of mode the polar mode along a and along ab. (c) Basic cubic unit cell labeled 111. (d) Possible supercells. Each cubic supercell is constructed from (c) multiplied along different directions and labeled accordingly. (e) Example of a combination of four modes to build a structure. All modes are scaled to the size of the third mode (multiplied by γ) and the distortions of each mode are multiplied by the amplitude factor $(\alpha, \beta, \gamma, \delta)$ and added to the cubic supercell 124.

We fix the maximum size of unit cell to contain at most 80 atoms and constrain the structures to four possible unit cell sizes displayed in Fig. 29d, all that accommodate G-type magnetic order.

Finally, to generate structures we consider a sub-set of modes, create supercells of each mode with the volume of the largest unit cell present in the sub-set, and multiply the displacement vector resulting from each mode with respect to the primitive supercell by a scalar amplitude as represented in Fig. 29e.

7.3 DESCRIPTION OF THE PROCEDURE

Our approach combines DFT and ML in two different rounds as shown in Fig. 30. The first round consists of building a training set based on distortion modes and computing the energy through single-point calculations with DFT, which consists in only relaxing the electrons while keeping the ions fixed, in order to fit the energies as a function of the modes' amplitudes. In the second round we generate a large number of structures and predict their energies using the model trained in the previous step. We then filter the structures with the lowest

energies and use them as initial configurations for full DFT relaxations. The second step accelerates the search of (meta)stable phases as we start from diverse but favourable initial structures.

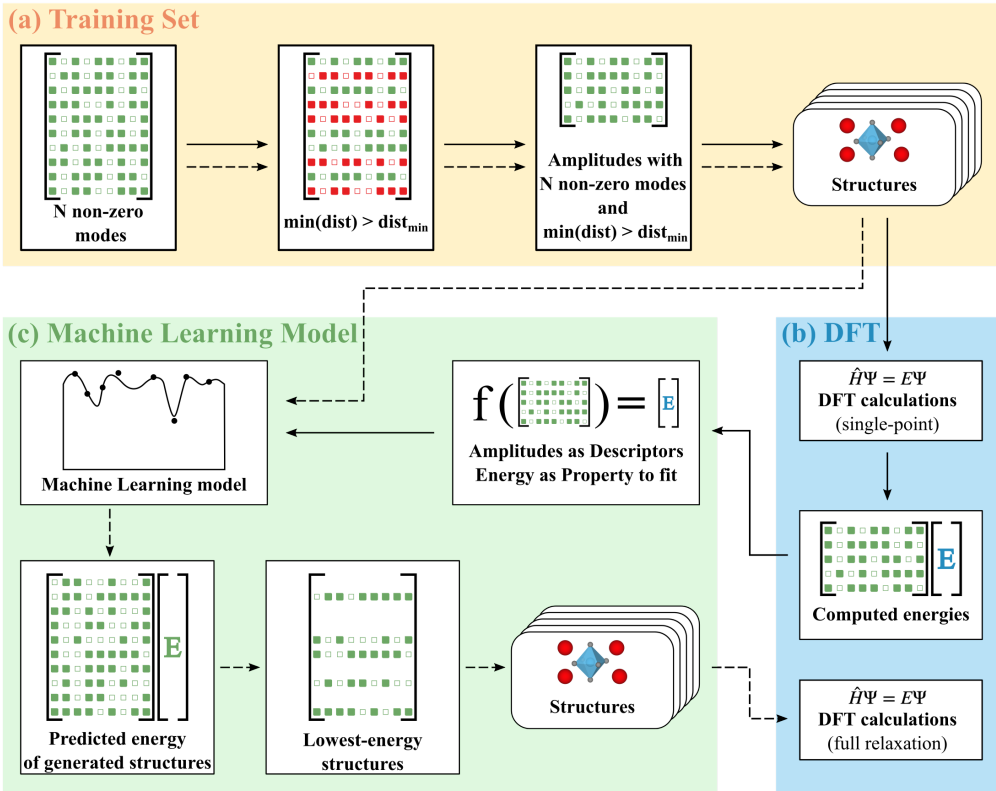

Figure 30: Overview of the procedure. The first round is indicated by solid arrows and the second by dashed ones. (a) We start from a list of N non-zero random amplitudes chosen within the range $[-1.2; 1.2]$, where each line of the list corresponds to a structure and each column to an amplitude. Non-zero amplitudes are represented by full squares and zero amplitudes by empty squares. From the list we discard (red) the structures in which two atoms are closer than the minimal distance allowed ($\mathtt{dist}_{\mathtt{min}}$). Finally we generate the input files corresponding to the structures for the DFT part. Note that all structures' volumes are fixed to that of the cubic undistorted cell. (b - top) We compute the energy with a single-point DFT calculation and associate an energy to each line of the list. The steps described for the training set and DFT part are repeated for different values of N. (c) We use the list of amplitudes gathered in the previous step and use them as descriptors and fit the corresponding energies using Machine Learning. We then obtain a model that can predict the energy of a given sequence of amplitudes. The second workflow is represented by dashed arrows. (a) Following the same steps as described in the first workflow we generate structures with different values of N. (c) Finally, we use the Machine Learning model created to predict the energy of those structures, select the lowest energy ones and create the corresponding structures. (b) We then use these structures as starting configurations and fully relax them (ions and lattice).

7.3.1 FIRST ROUND: MACHINE LEARNING MODEL

The first round starts with the generation of the training set. We consider the potential energy surface of BFO in a 21-dimensional space where each dimension is given by a distortion mode and each coordinate in the space is given by the amplitude of the modes (dimensions). As we want to span evenly the energy surface, we generate randomly the amplitudes of the modes in the interval $[-1.2; 1.2]$. We recall that for example an amplitude of 1.2 means that the sum of the displacement in the parent structure is equal to 1.2 Å. This choice is arbitrary but is made such that we can capture for each mode the double well of energy. Furthermore, in order to account for the physics of each mode individually as well as the favourable or unfavourable couplings between different modes, we consider couplings until 7th order by including structures generated by up to 7 modes with amplitudes different than zero.

Our procedure starts (Fig. 30a) by choosing an order of coupling N, equal to the number of non-zero amplitudes, and generating a matrix of L lines and 21 random numbers in the interval $[-1.2; 1.2]$ for each line. We then obtain a matrix of dimension $L \times 21$, where L is the number of potential structures. Secondly, we set randomly to zero (21-N) amplitudes per line and discard unphysical structures by computing the minimum distance between pairs of atoms in each structure and removing the structures whose minimum distance is too small. Based on the distribution of the Fe-O bond length in all structures containing these ions in the ICSD database [108, 109], we keep only structures with atomic spacings larger than 1.8 Å. This procedure is repeated for each value of N considered and results in a set of structures ready for the following step.

We then take all the structures created and compute their energies with a single-point calculation in which only one electronic loop is computed. We obtain for each structure – line of amplitudes in the matrix – a corresponding energy (Fig. 30b, top).

We present in Fig. 31 the energies of the different structures included in the training set, and can see that the majority of the structures included in the training set has an energy lying between that of the R3c phase constrained to the cubic parent structure volume and angles and that of the cubic parent structure. Furthermore, we can see that when the number of modes present in the structure increases, the energy tends to increase also. This can easily be understood by the fact that we use random amplitudes and the more distortions we add, the more likely it is that the distance between ions decreases and the energy consequently increases.

Finally, the last step of the first round (see Fig. 30c) consists of using the training set to fit the energies as a function of the amplitudes of the modes. We proceed as detailed in section 7.1 and obtain a model with an accuracy of almost 80% (average coefficient of determination (r^2) of 0.77) and a root-mean-square error of 0.2 eV (on the prediction on the energy value). We present in Fig. 32a the comparison between the energy predicted by the model and the actual DFT energy. The more the points are spread away from the diagonal line, the less accurate is the model. We see in particular that the model performs

better at low energy, which is more important for the purpose of our study. For instance within the range of energy contained by the constrained R3c and cubic structures, the points are less spread around the diagonal line than further on the upper right of the plot. This can principally be attributed to the lower representation of high energy structures in the training set.

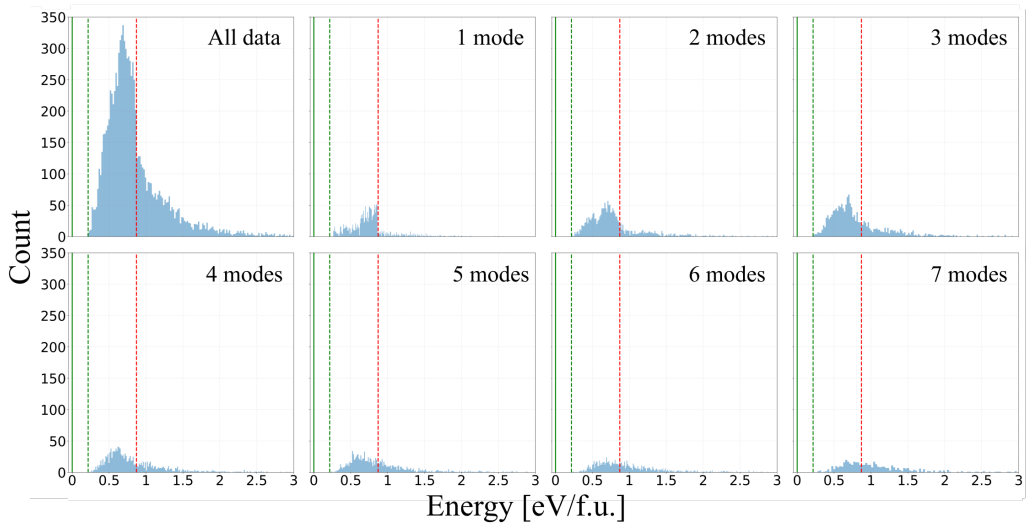

Figure 31: Histograms of the training set. The whole training set generated combines 9569 structures (top-left) distributed in structures combining 1 mode (1922 structures), 2 modes (1768 structures), 3 modes (1574 structures), 4 modes (1424 structures), 5 modes (1266 structures), 6 modes (1139 structures) and 7 modes (476 structures). The continuous green vertical line represents the reference energy of the R3c ground state. The dashed green vertical line shows the energy of the constrained R3c structure where the R3c coordinates have been constrained to the cubic parent structure (volume and angles) and the dashed red vertical line displays the energy of the cubic parent structure (amplitudes of all the modes set to zero). The bins have a size of 10 meV in all plots except the 7 modes one, where the bin size is 30 meV for better visualisation.

We can further evaluate the accuracy of the model by removing all structures containing only one mode (1922 points) from the training set and fitting the model again. We can evaluate the coefficient of determination of the model again and we obtain a lower precision of about 74% (r^2 is 0.74). We see in Fig. 32b, a behaviour consistent with Fig. 32a, in which the model performs better at low energy. This can further be observed in Fig. 32c, where we use the second model to predict the energy of the structures removed from the training set. We observe that, while the predicted value of the energy deviates from the real value, the model is able to capture quite accurately the shape of the energies as a function of the amplitudes of a single mode. This further proves that, for the purpose of our study, the model is accurate enough.

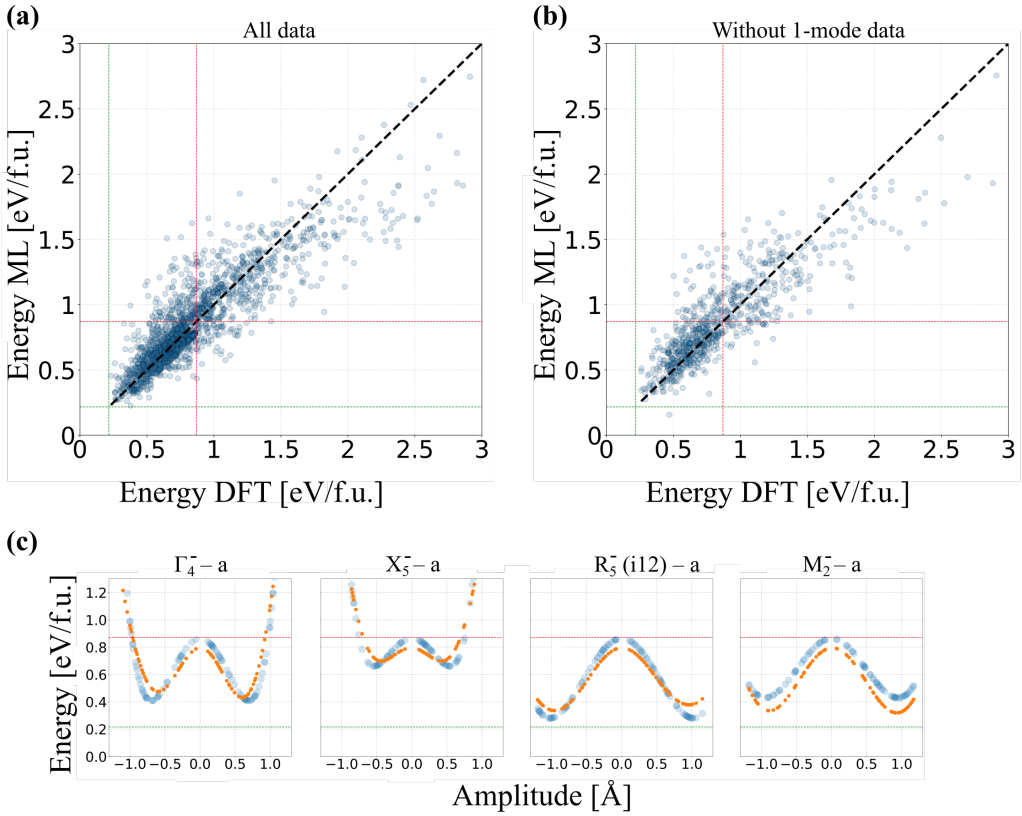

Figure 32: Evaluation of the coefficient of determination (r^2) of the ML models. (a) Predicted (ML) energy versus computed (DFT) energy for the complete training set. (b) Predicted energy versus computed energy when all the structures containing only one mode were removed. (c) Computed energies (blue) compared to the energies predicted with the model fitted on the data without the 1-mode structures (orange) for different common modes. In all plots the red and green lines are respectively the energy of the cubic and R3c-like structures.

7.3.2 SECOND ROUND: LOW ENERGY PHASES

In the second round we use the constructed model to predict the energies of a large amount of structures built with random combinations of 1 to 7 modes combined together. We construct 457,081 structures in the same way as described in Fig. 30a and predict their energies. We then select the structures that have an energy difference relative to the ground state of less than 250 meV/f.u., classify them into subsets according to the modes that they contain and select the lowest energy structure of each subset. We end up with 290 structures, all with different combinations of modes, that we fully relax with DFT.

Focusing only on the structures displaying an energy of 100 meV/f.u. or less above the R3c ground state after full relaxation, we obtain 29 different structures among which 4 phases are the common R3c, $Pnma$, $Pbam$ and $Pmc2_1$ and 4 were already identified in Ref. [88] ($Pc(1)$, $Pnma(1)$, $Cmc2_1(2)$ and $P2_1/c$ – see chapter 4). We then obtain 21 new phases that we report in Tab. 6. We observe

	Lattice parameters				Energies
Symmetry	a [Å]	b [Å]	c [Å]	Angles [deg.]	Energy [meV/f.u.]
P1	5.54	11.14	15.55	$\alpha = 90.020, \beta = 90.087, \gamma = 90.023$	48
	5.55	11.17	7.76	$\alpha = 90.175, \beta = 90.012$	54
	5.52	5.54	15.84	$\alpha = 90.492, \beta = 90.233, \gamma = 90.061$	57
P2$_1$	5.52	11.04	15.68	$\beta = 90.272$	44
	5.55	11.02	15.62	$\beta = 90.085$	54
Pm	5.52	15.67	11.10	$\beta = 90.128$	45
	5.53	11.09	7.78	$\beta = 90.006$	56
Cc	7.79	7.81	15.92	$\beta = 90.623$	68
P2$_1$/m	5.52	11.11	15.66	$\beta = 90.269$	46
P2$_1$/c	5.54	11.15	7.76	$\beta = 90.301$	64
	5.49	11.15	15.67	$\beta = 90.707$	68
Pmc2$_1$	5.55	11.00	7.79		41
	5.53	11.10	15.65		42
	5.52	11.15	7.77		69
	5.50	5.56	15.53		96
Pca2$_1$	5.48	5.57	15.75		23
Pmn2$_1$	5.53	5.59	7.85		88
Cmc2$_1$	5.62	11.15	7.81		96
Ima2	5.58	5.59	7.75		77
	5.58	5.59	15.49		82
Pbca	5.57	11.04	15.53		55

Table 6: Low-energy phases identified. We give the symmetry (space group), lattice vectors, angle (indicated if different than 90°) and energy relative to the R3c ground state. The symmetries are determined using Pymatgen [110] with a tolerance of 10^{-3} Å.

that the majority of the phases found have 80 atoms/unit cell and have an energy around 40-50 meV/f.u. above the ground state.

While a deep analysis of the different phases is out of the scope of this chapter, here we analyse the lowest-energy phase found with $Pca2_1$ symmetry and present its crystal structure in Fig. 33. Its unit cell as shown in Fig. 33a is similar to the $Pc(1)$ phase presented in chapter 4 and it has the same energy difference with respect to the ground state (23 meV/f.u.). As a reminder, in the $Pc(1)$ structure, the Bi cations are displaced perpendicular to the long axis with three cations moving in one direction and one in the opposite direction. The $Pca2_1$ has a different pattern with two Bi cations moving in one direction and the next two in the opposite direction (see Fig. 33b). $Pca2_1$ also displays a different rotation pattern with $a^{\bar{\alpha}\beta}a^{\bar{\alpha}\beta}c^{\bar{\alpha}\beta\bar{\gamma}\bar{\delta}}$ rotations, as opposed to the $a^{\bar{\alpha}\beta}a^{\bar{\alpha}\beta}c^{\bar{\alpha}\beta\bar{\gamma}\delta}$

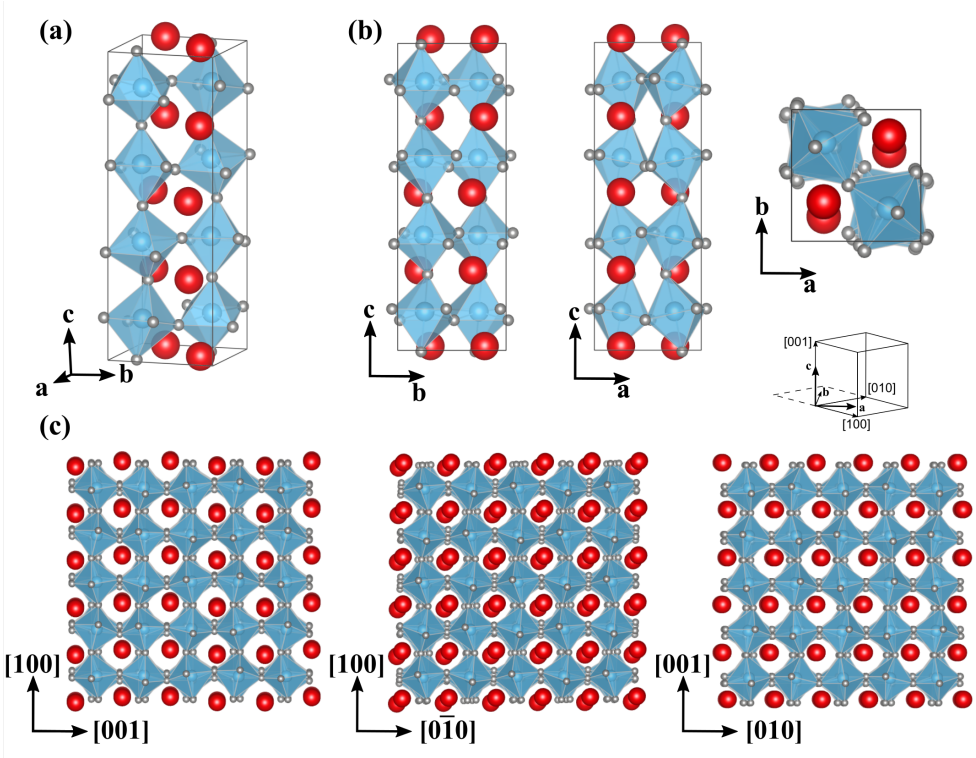

Figure 33: Crystal structure of the $Pca2_1$ phase. (a) Full unit-cell. (b) Different projections of the unit-cell. (c) $Pca2_1$ supercells imaged along different pseudo-cubic directions.

rotations in $Pc(1)$. Using the same method as described in Ref. [88], we evaluate the spontaneous polarisation to be around 54 $\mu C/cm^2$ along the c axis (long axis). This result is interesting in light of chapter 4 as this structure would be electrostatically favourable if the c-axis were to lie parallel to the interface in a heterostructure with a non-polar III-III material. We present in Fig. 33c the different pseudo-cubic orientations and the structures that could be observed in STEM images. In particular, we see that for the c axis in-plane, a "2up-2down" displacement pattern of the Bi cations appears along the [100] direction. Note that it is different from the $Pnma(1)$ structure presented in chapter 3 as in the latter case the displacements between consecutive layers were diagonally shifted (see Fig. 11).

7.4 CONCLUSION AND PERSPECTIVE

In summary, in this chapter we revisited the phase space of BFO already explored in chapter 4. While in the previous chapter our approach was to start from identified phases and look for instabilities in large supercells, in this chapter we took a more general approach. Indeed, we decomposed the different phases identified in chapter 4 into distortion modes and used them as building blocks (21 modes) that we combined together with random amplitudes in order to create new structures. As the amount of possibilities to combine 21 modes is

almost infinite, we trained a machine learning model able to predict the energy of a structure based on the amplitudes of the different modes that it contains. We further generated a large number of structures containing between 1 and 7 distortion modes and predicted their energies with our model. By selecting and relaxing the lowest-energy structures we could identify 29 low-energy phases, 21 of which were previously unidentified.

Despite the fact that the phases identified were found by initialising the relaxation from different low-energy structures, many different starting structures relaxed into the same final phase. A more efficient approach would be to look directly for local minima of the energy surface. In general, given a set of coordinates (usually positions of atoms) and a potential describing their interactions, one can look for local minima by exploring the energy landscape, in which each point on the energy surface corresponds to a configuration (set of positions). This can be automatised using Monte-Carlo algorithms and existing software such as PELE[2]. In our problem we can transpose the coordinates to be the amplitudes of the modes, then each point on the energy surface corresponds to a combination of modes with certain amplitudes. Our machine learning model then derives the potential describing the "interactions" between the modes.

While in the current chapter we restricted our search to structures containing from 1 to 7 modes, the latter approach is general in the sense that any combination of modes could be identified as a local minimum. Nevertheless, as structures containing more modes are likely to be higher energy, more such structures should be included in the training set in order for the model to perform well everywhere in the mode space and not only in restricted sub-spaces with fewer modes.

[2]https://github.com/pele-python/pele

Part V

CONCLUSION

"There is no real ending. It is just the place where you stop the story."

— Frank Herbert

Summary and Outlook

8

In this thesis we presented a theoretical investigation of the well-studied and prototypical multiferroic material, $BiFeO_3$, with the general objective of identifying and controlling new functionalities going beyond ferroelectricity and antiferromagnetism. Driven by the strong coupling existing between structure and properties in oxide perovskites, a large portion of the current work was devoted to structure prediction through existing techniques (Parts II – chapters 3-5) or new approaches (Part IV).

In Part II, we investigated new structures of BFO and explained or anticipated their stability in heterostructures, with a particular emphasis on the importance of the boundary conditions provided by the heterostructure.

We started our study showing in chapter 3 that the polar discontinuity at the interface between $BiFeO_3$ and $(La,Bi)FeO_3$ can induce a phase transition from the polar ground state to a non-polar phase in BFO. We identified a new phase of BFO containing 80 atoms/u.c. and demonstrated through a simple electrostatic model that it is energetically more favourable to stabilise this phase over the ground state due to the large electrostatic cost of screening bound charges at the interfaces of BFO. We further confirmed that this result is not limited to the particular heterostructure considered, showing that appropriate choices of thickness, dielectric constant of the surrounding material and strain can favour a non-polar phase over a polar one. Furthermore, we anticipated that a similar scenario could possibly happen in other materials than BFO under certain requirements: The chosen material should be polar in its ground state and there should exist a low energy non-polar phase. The heterostructure should be such that there is a large polar discontinuity at the interfaces and the material surrounding the polar one should have a relatively low dielectric constant in order to disfavour the possible screening of the bound charges.

In the follow-up study presented in chapter 4, we showed that the phase identified in the previous chapter is not the only structure with a large unit cell and a low internal energy existing in the BFO phase space. Starting from experimentally stabilised or computationally predicted phases such as $Pnma$, $Pbam$, $Pmc2_1$ or $P4mm$, we explored phonon instabilities along different directions. We found that larger period structural distortions can further lower the energy of some of these phases.We identified several low-energy phases containing up to 160 atoms per unit cell. As some of them present complex tilts, we proposed an extension to the convenient and widely used Glazer notation. In particular, we identified two series of non-centrosymmetric structures with Pc symmetry that are reminiscent of ferroelectric domains along a particular direction. We finally discussed their possible experimental stability in the light of the findings of chapter 3 and predicted that under proper strain and electrostatic boundary

conditions some of these phases are likely to be stabilised over the R3c ground state.

We concluded Part II, by considering the experimentally motivated case of BFO grown on LAO in chapter 5. It was observed that despite the large out-of-plane polarisation under highly compressive strain, BFO remains stable to domain formation during growth as well as under capping with a metallic $II-IV$ perovskite electrode, with a lowering of the c/a ratio in the latter case. We demonstrated that this behaviour can be attributed to an isometric phase transition between two structures with different out-of-plane polarisation and is driven by the electrostatic cost at the interface that is only partially compensated by the ionic charged layer discontinuity and only partially screened by the metallic electrodes.

In Part III (chapter 6) we extended our study to another composition in the (Bi,Fe,O) phase space beyond perovskite structure and chemistry of $BiFeO_3$. Motivated by the experimental finding of a possibly new multiferroic at room temperature, bismuth hexaferrite, $Bi_6Fe_{32}O_{57}$, which has been characterised to be polar and exhibiting a net magnetic moment, we addressed the origin of the magnetisation and found that the net moment is likely to come from uncompensated magnetic moments between two magnetic sub-lattices due to the presence of Fe vacancies. Furthermore, we found a low energy barrier to switch the polarisation, suggesting that the material is a good ferroelectric candidate.

Finally, in Part IV (chapter 7) we returned to the traditional $BiFeO_3$ and proposed another approach to explore the phase space, by combining DFT and machine learning. We extracted the normal modes from the phases identified in chapter 4 and used them as building blocks to create new structures. We considered 21 modes and computed with single-point calculations the energy of around $10,000$ structures that we use as training set for a machine-learning model. We fitted the energy surface in a 21-dimensional space generated by the modes and then predicted the energy of a larger number of structures. Finally, we selected the lowest energy ones to be fully relaxed with DFT and identified 21 additional modes, not discovered in part II.

The main findings of this thesis are two-fold. First, we demonstrated that the control of the electrostatic boundary conditions can be a driving force to engineer new properties in ferroelectric materials which we hope can motivate similar studies for other ferroelectric materials. For instance, antiferroelectricity could be investigated in $LiNbO_3$ since this material has the same R3c ground state as BFO and could hypothetically experience, similarly to BFO, a phase transition under certain electrostatic boundary conditions. Second, while this thesis represents only a small contribution to the widely studied material that is BFO[1], we demonstrated that this material keeps revealing secrets and likely has many more to be discovered.

Further studies could take advantage of the great flexibility of BFO and look for large scale structures such as domains or more exotic topological structures such as polar vortices. While planar topological defects also known as do-

[1]More than 3000 papers containing $BiFeO_3$ in the title have been published in the last five years according to Web of Science.

main walls emerge naturally in ferroelectric materials, as a consequence of the bound charges, the stabilisation of exotic polar topologies analogous to magnetic skyrmions is challenging. Indeed, as the polarisation is strongly coupled to the lattice, rotating it continuously away from its symmetrically allowed orientation results in a large energy cost. The stabilisation of polar vortices results from a competition between the elastic energy (strain imposed by the substrate), the electrostatic energy (bound charges) and the gradient energy (change in magnitude and direction of the polarisation). Polar vortices have been observed experimentally in ferroelectric materials within superlattices but never in multiferroic materials. While phase-fields simulations have been widely used for describing the evolution of these polar structures, the non-atomistic nature of such techniques does not allow the description of local structures and becomes then unlikely to guide further experimental work in materials where no experimental structural data can be provided. The challenge remains then in having accurate and effective (large scale) simulations. In this matter, second-principles methods propose a route to building effective potentials with DFT accuracy. This approach consists of combining a harmonic part extracted from density functional perturbation theory and an anharmonic part fitted on forces and stresses computed for various structures obtained from DFT and forming the training set. Similar to all fitting problems, the quality and flexibility of the model depends on the training set, as it is in general difficult for a fitted model to perform well far from the data it fits. In the context of interatomic potentials, this is equivalent to finding a good description of the whole potential energy surface. Our approach to explore the energy surface combining DFT and machine learning as well as the various already identified minima on the energy surface already provide an extensive description of the energy surface and could then be a good starting point for building a second-principles model and extend the study of BFO and its properties to larger scale.

Publications

published / submitted

- **Prediction of low-energy phases of $BiFeO_3$ with large unit cells and complex tilts beyond Glazer notation**
  Bastien F. Grosso and Nicola A. Spaldin, *Phys. Rev. Materials* 5 (5), 054403 (2021)

- **Graphene gets bent**
  Bastien F. Grosso and Eugene J. Mele, *Physics Today* 73 (9), 46-52 (2020)

- **A high-energy density antiferroelectric made by interfacial electrostatic engineering**
  Julia A. Mundy*, Colin A. Heikes*, Bastien F. Grosso*, Dan F. Segedin, Zhe Wang, Berit H. Goodge, Quintin N. Meier, Christopher T. Nelson, Bhagwati Prasad, Lena F. Kourkoutis, William D. Ratcliff, Nicola A. Spaldin, Ramamoorthy Ramesh, and Darrell G. Schlom, *arXiv:1812.09615*

- **Bending Rules in Graphene Kirigami**
  Bastien F. Grosso and Eugene J. Mele, *Phys. Rev. Lett.* 115, 195501 (2015)

- **Mini-review of electron density visualization**
  J. Adler, O. Adler, M. Kreif, O. Cohen, B. Grosso, A. Hashibon, and V. R. Cooper, *Phys. Procedia* 68, 2-6 (2015)

- **Visualization of electronic density**
  B. Grosso, V. R. Cooper, P. Pine, A. Hashibon, Y. Yaish and J. Adler, *Comput. Phys. Commun.* 195, 1 (2015)

in preparation

- **Emergence of ferroelectricity at the morphotropic phase boundary of ultrathin $BiFeO_3$**
  Johanna Nordlander, Bastien F. Grosso, Marta D. Rossell, Aline Maillard, Elzbieta Gradauskaite, Nicola A. Spaldin, Manfred Fiebig, and Morgan Trassin

- **A new room temperature multiferroic bismuth hexaferrite**
  Tianzhe Chen*, Shuzhen Yang*, Christopher T. Nelson*, Bastien F. Grosso*, Guopeng Wang, Vishal Thakare, Martin Dahlqvist, Meng Wang, Qing He, Naoki Ogawa, Jingwen Guo, Yujia Wang, Zhuolo Li, Nianpeng Lu, Haobo Li, Ke Deng, Mingzhe Yan, Shanglin Hsu, Shyam Dwaraknath, James D. Clarkson, Julia A. Mundy, Alan Farhan, Alpha T. N'Diaye, Andreas Scholl,

Elke Arenholz, Masao Nakamura, Masashi Kawasaki, Shuyun Zhou, Cewen Nan, Yoshi Tokura, Nicola A. Spaldin, Ramamoorthy Ramesh, and Pu Yu

Bastien Francesco Grosso
PhD candidate in Materials Theory
Materials Theory [D-MATL] | ETH Zürich | Wolfgang-Pauli-Strasse 27, HIT G 43.2
bastien.grosso@mat.ethz.ch | (+41)44 633 94 10

EDUCATION

Swiss Federal Institute of Technology Zurich (ETHZ) 2016 - 2021
- PhD in Materials Theory, Research Advisor : Prof. Nicola Spaldin

Swiss Federal Institute of Technology Lausanne (EPFL) 2010 - 2015
- Master in Physics and Minor in Computational Science and Engineering
- Bachelor in Physics

Collège de l'Abbaye de Saint-Maurice 2006-2010
- High School diploma in Sciences (Physics, Applied Mathematics and Computer Science)

Ecole Supérieur de Commerce de Monthey 2002-2006
- Vocational High School Diploma in Business (3 years of courses and 1 year internship)

PROFESSIONAL EXPERIENCE

ETHZ, Zurich – Research Assistant Oct.. 2016 – present

EAWAG Aquatic Research Center, Urban Water Management, Zurich – Co-worker Nov. 2015 – Jun. 2016

Loughborough University, Loughborough, United Kingdom – *Academic Visitor* Feb. 2015 – Aug. 2015
- *Master Thesis under supervision of Prof. Eugene Mele*

EU-FP7, Technion Israel Institute of Technology, Haifa – *Research Student* Jul. 2014 – Sept. 2014

EPFL, Lausanne – *Student-Assistant* 2012 - 2014

State of Valais' Canton, Sion – *Substitute teacher* 2013 - 2014

Student Forum, Sierre – *Representative for the Physics Faculty of the EPFL* 7 Fev. 2012 and 5 Fev. 2013

CONFERENCE AND WORKSHOP PRESENTATIONS

6) Can strongly polar $BiFeO_3$ become antipolar?, Condensed Matter Seminar, Universidad de Los Andes, Bogotá, Colombia, February **2020**, *Invited Talk*

5) Multiferroics: bulk, thin films and the prototypical case of $BiFeO_3$, Physics Colloquium series, Universidad de Los Andes, Bogotá, Colombia, February **2020**, *Invited Talk*

4) Stabilisation of a new antiferroelectric phase of $BiFeO_3$ through electrostatic engineering in oxide heterostructure, MRS Fall Meeting, Boston, Massachusetts, December **2019**, *Talk*

3) Stabilisation of a new antiferroelectric phase of $BiFeO_3$ through electrostatic engineering in oxide heterostructure, Joint Conference of the International Symposium on Applications of Ferroelectrics and European meeting on Ferroelectricity, Lausanne, Switzerland, July **2019**, *Talk*

2) Stabilisation of a new antiferroelectric phase in oxide heterostructure with $(La,Bi)FeO_3$, International School on Fundamental Crystallography Sixth MaThCryst school in Latin America, Bogotá, Colombia, November **2018**, *Poster*

1) Stabilisation of a new antiferroelectric phase in oxide heterostructure with $(La,Bi)FeO_3$, Gordon Research Conference on Multiferoic and Magnetoelectric, Bates College, Lewiston (ME), United States, August **2018**, *Poster*

HONORS AND AWARDS

Best poster presentation at International School on Fundamental Crystallography Sixth MaThCryst school in Latin America, Bogotá, Colombia, November **2018**

First prize for the best presentation of Physics Lab report among the Bachelor students in Physics, EPFL Lausanne, December **2013**

REVIEWER FOR INTERNATIONAL JOURNALS

Physical Review B

Nature Communications

TEACHING EXPERIENCE

Simulations Techniques for Materials Science, ETH Zürich, Fall **2018**, Fall **2019** and Fall **2020**
(Section of Materials 5th semester)

Programming Techniques for Materials Science, ETH Zürich, Fall **2017**
(Section of Materials 3rd semester)

Computational Physics III, EPFL Lausanne, Spring **2014**
(Section of Physics 5th semester and Section of Computational Sciences 7th semester)

General Physics I, EPFL Lausanne, Fall **2012**
(Section of Mathematics, 1st semester)

RESEARCH STUDENTS MENTORED

Ramon Frey, Master Project, Development of a Machine Learning and High Throughput DFT Framework to Predict Crystal Structures of New Ferroelectrics, ETH Zürich, Spring **2020**

Joanna Stoycheva, Master Thesis, (MARVEL Master's Fellowship), Polarization in the heterostructure of super tetragonal $BiFeO_3$ and $LaFeO_3$, ETH Zürich, Fall **2019**

Fabian Haake, Bachelor Thesis, First-principles study of multiferroic Bi_2O_3-Fe_2O_3 heterostructures beyond the perovskite structure, ETH Zürich, Spring **2019**

LANGUAGES

Native or bilingual proficiency: French, Italian, English, Spanish

Limited working proficiency: German

Elementary proficiency: Hebrew

Bibliography

[1] Hans Schmid. "Multi-ferroic magnetoelectrics." In: *Ferroelectrics* 162.1 (1994), pp. 317–338. DOI: 10.1080/00150199408245120.

[2] Nicola A. Hill. "Why Are There so Few Magnetic Ferroelectrics?" In: *J. Phys. Chem. B* 104.29 (2000), pp. 6694–6709. DOI: 10.1021/jp000114x.

[3] J. Valasek. "Piezo-Electric and Allied Phenomena in Rochelle Salt." In: *Phys. Rev.* 17.4 (1921), pp. 475–481. DOI: 10.1103/physrev.17.475.

[4] K. Rabe, C. H. Ahn, and J-M. Triscone, eds. *Physics of Ferroelectrics*. Springer Berlin Heidelberg, 2007. DOI: 10.1007/978-3-540-34591-6.

[5] E. Ascher, Schmid H., and D. Tar. "Dielectric properties of boracites and evidence for ferroelectricity." In: *Solid State Commun.* 2.2 (1964), pp. 45–49. DOI: 10.1016/0038-1098(64)90571-x.

[6] R.R. Neurgaonkar, J.G. Nelson, and J.R. Oliver. "Ferroelectric properties of the tungsten bronze $M_6^{2+}M^{4+}{}_2Nb_8O_{30}$ solid solution systems." In: *Mat. Res. Bull.* 27.6 (1992), pp. 677–684. DOI: 10.1016/0025-5408(92)90074-a.

[7] V. M. Goldschmidt. "Die Gesetze der Krystallochemie." In: *Die Naturwissenschaften* 14.21 (1926), pp. 477–485. DOI: 10.1007/bf01507527.

[8] Ronald E. Cohen. "Origin of ferroelectricity in perovskite oxides." In: *Nature* 358.6382 (1992), pp. 136–138. DOI: 10.1038/358136a0.

[9] Jeremy K. Burdett. "Use of the Jahn-Teller theorem in inorganic chemistry." In: *Inorg. Chem.* 20.7 (1981), pp. 1959–1962. DOI: 10.1021/ic50221a003.

[10] H. D. Megaw. "Origin of ferroelectricity in barium titanate and other perovskite-type crystals." In: *Acta Crystallogr.* 5.6 (1952), pp. 739–749. DOI: 10.1107/s0365110x52002069.

[11] J. B. Neaton, C. Ederer, U. V. Waghmare, N. A. Spaldin, and K. M. Rabe. "First-principles study of spontaneous polarization in multiferroicBiFeO3." In: *Phys. Rev. B* 71.1 (2005), p. 014113. DOI: 10.1103/physrevb.71.014113.

[12] A. M. Glazer. "The classification of tilted octahedra in perovskites." In: *Acta. Cryst.* B20 (1972), pp. 3384–3392. DOI: 10.1107/S0567740872007976. URL: https://doi.org/10.1107/S0567740872007976.

[13] R. Clausius. *Die Mechanische Behandlung der Electricität*. Vieweg+Teubner Verlag, Jan. 1879. 368 pp. ISBN: 366319891X. URL: https://www.ebook.de/de/product/23156106/r_clausius_die_mechanische_behandlung_der_electricitaet.html.

[14] O. F. Mossotti. "Azioni e deformazioni nei dielettrici." In: *Memorie di Matematic e di Fisica della Società Italiana delle Scienze Residente in Modena* **24**, *49* (1850).

[15] R. Resta. "Theory of the electric polarization in crystals." In: *Ferroelectrics* 136.1 (1992), pp. 51–55. DOI: 10.1080/00150199208016065.

[16] Raffaele Resta. "Macroscopic polarization in crystalline dielectrics: the geometric phase approach." In: *Rev. Mod. Phys.* 66.3 (1994), pp. 899–915. DOI: 10.1103/revmodphys.66.899.

[17] R. D. King-Smith and David Vanderbilt. "Theory of polarization of crystalline solids." In: *Phys. Rev. B* 47.3 (1993), pp. 1651–1654. DOI: 10.1103/physrevb.47.1651.

[18] Nicola A. Spaldin. "A beginner's guide to the modern theory of polarization." In: *J. Solid State Chem.* 195 (2012), pp. 2–10. DOI: 10.1016/j.jssc.2012.05.010.

[19] M. V. Berry. "Quantal phase factors accompanying adiabatic changes." In: *Proceedings of the Royal Society of London. A. Mathematical and Physical Sciences* 392.1802 (1984), pp. 45–57. DOI: 10.1098/rspa.1984.0023.

[20] E. Ascher, H. Rieder, H. Schmid, and H. Stössel. "Some Properties of Ferromagnetoelectric Nickel-Iodine Boracite, Ni3B7O13I." In: *J. Appl. Phys.* 37.3 (1966), pp. 1404–1405. DOI: 10.1063/1.1708493.

[21] G A Smolenskiĭ and I E Chupis. "Ferroelectromagnets." In: *Soviet Physics Uspekhi* 25.7 (1982), pp. 475–493. DOI: 10.1070/pu1982v025n07abeh004570.

[22] Daniel Khomskii. "Classifying multiferroics: Mechanisms and effects." In: *Physics* 2 (2009), p. 20. DOI: 10.1103/physics.2.20.

[23] Jeroen van den Brink and Daniel I Khomskii. "Multiferroicity due to charge ordering." In: *J. Phys.: Condens. Matter* 20.43 (2008), p. 434217. DOI: 10.1088/0953-8984/20/43/434217.

[24] Claude Ederer and Nicola A. Spaldin. "Origin of ferroelectricity in the multiferroic barium fluoridesBaMF4: A first principles study." In: *Physical Review B* 74.2 (2006), p. 024102. DOI: 10.1103/physrevb.74.024102.

[25] Bas B. Van Aken, Thomas T.M. Palstra, Alessio Filippetti, and Nicola A. Spaldin. "The origin of ferroelectricity in magnetoelectric YMnO3." In: *Nat. Mater.* 3.3 (2004), pp. 164–170. DOI: 10.1038/nmat1080.

[26] I. A. Sergienko and E. Dagotto. "Role of the Dzyaloshinskii-Moriya interaction in multiferroic perovskites." In: *Phys. Rev. B* 73.9 (2006), p. 094434. DOI: 10.1103/physrevb.73.094434.

[27] I. Dzyaloshinsky. "A thermodynamic theory of "weak" ferromagnetism of antiferromagnetics." In: *J. Phys. Chem. Solids* 4.4 (1958), pp. 241–255. DOI: 10.1016/0022-3697(58)90076-3.

[28] Tôru Moriya. "Anisotropic Superexchange Interaction and Weak Ferromagnetism." In: *Phys. Rev.* 120.1 (1960), pp. 91–98. DOI: 10.1103/physrev.120.91.

[29] Sang-Wook Cheong and Maxim Mostovoy. "Multiferroics: a magnetic twist for ferroelectricity." In: *Nat. Mater.* 6.1 (2007), pp. 13–20. DOI: 10.1038/nmat1804.

[30] P Fischer, M Polomska, I Sosnowska, and M Szymanski. "Temperature dependence of the crystal and magnetic structures of BiFeO3." In: *J. Phys. C: Solid State Phys.* 13.10 (1980), pp. 1931–1940. DOI: 10.1088/0022-3719/13/10/012.

[31] J.M. Moreau, C. Michel, R. Gerson, and W.J. James. "Ferroelectric BiFeO3 X-ray and neutron diffraction study." In: *J. Phys. Chem. Solids* 32.6 (1971), pp. 1315–1320. DOI: 10.1016/s0022-3697(71)80189-0.

[32] F. Kubel and H. Schmid. "Structure of ferroelectric and ferroelastic monodomain crystal of the perovskite $BiFeO_3$." In: *Acta Cryst.* B46 (1990), pp. 698–702. DOI: 10.1107/S0108768190006887. URL: https://doi.org/10.1107/S0108768190006887.

[33] J. Wang, J. B. Neaton, H. Zheng, V. Nagarajan, S. B. Ogale, B. Liu, D. Viehland, V. Vaithyanathan, D. G. Schlom, U. V. Waghmare, N. A. Spaldin, K. M. Rabe, M. Wuttig, and R. Ramesh. "Epitaxial $BiFeO_3$ multiferroic thin film heterostructures." In: *Science* 299 (2003), pp. 1719–1722. DOI: 10.1126/science.1080615. URL: https://doi.org/10.1126/science.1080615.

[34] Gustau Catalan and James F. Scott. "Physics and Applications of Bismuth Ferrite." In: *Adv. Mater.* 21.24 (2009), pp. 2463–2485. DOI: 10.1002/adma.200802849.

[35] Claude Ederer and Nicola A. Spaldin. "Weak ferromagnetism and magnetoelectric coupling in bismuth ferrite." In: *Phys. Rev. B* 71.6 (2005), p. 060401. DOI: 10.1103/physrevb.71.060401.

[36] J. T. Zhang, X. M. Lu, J. Zhou, H. Sun, J. Su, C. C. Ju, F. Z. Huang, and J. S. Zhu. "Origin of magnetic anisotropy and spiral spin order in multiferroic BiFeO3." In: *Appl. Phys. Lett.* 100.24 (2012), p. 242413. DOI: 10.1063/1.4729555.

[37] I Sosnowska, T P Neumaier, and E Steichele. "Spiral magnetic ordering in bismuth ferrite." In: *J. Phys. C: Solid State Phys.* 15.23 (1982), pp. 4835–4846. DOI: 10.1088/0022-3719/15/23/020.

[38] James M. Rondinelli and Nicola A. Spaldin. "Structure and Properties of Functional Oxide Thin Films: Insights From Electronic-Structure Calculations." In: *Adv. Mater.* 23.30 (2011), pp. 3363–3381. DOI: 10.1002/adma.201101152.

[39] J. H. Haeni, P. Irvin, W. Chang, R. Uecker, P. Reiche, Y. L. Li, S. Choudhury, W. Tian, M. E. Hawley, B. Craigo, A. K. Tagantsev, X. Q. Pan, S. K. Streiffer, L. Q. Chen, S. W. Kirchoefer, J. Levy, and D. G. Schlom. "Room-temperature ferroelectricity in strained SrTiO3." In: *Nature* 430.7001 (2004), pp. 758–761. DOI: 10.1038/nature02773.

[40] R. J. Zeches, M. D. Rossell, J. X. Zhang, A. J. Hatt, Q. He, C.-H. Yang, A. Kumar, C. H. Wang, A. Melville, C. Adamo, G. Sheng, Y.-H. Chu, J. F. Ihlefeld, R. Erni, C. Ederer, V. Gopalan, L. Q. Chen, D. G. Schlom, N. A. Spaldin, L. W. Martin, and R. Ramesh. "A Strain-Driven Morphotropic

Phase Boundary in BiFeO3." In: *Science* 326.5955 (2009), pp. 977–980. DOI: 10.1126/science.1177046.

[41] A. J. Hatt, N. A. Spaldin, and C. Ederer. "Strain-induced isosymmetric phase transition in $BiFeO_3$." In: *Phys. Rev. B* 81 (2010), p. 054109. DOI: 10.1103/PhysRevB.81.054109. URL: https://doi.org/10.1103/PhysRevB.81.054109.

[42] Nicola A. Spaldin, Ipek Efe, Marta D. Rossell, and Chiara Gattinoni. "Layer and spontaneous polarizations in perovskite oxides and their interplay in multiferroic bismuth ferrite." In: *J. Chem. Phys.* 154.15 (2021), p. 154702. DOI: 10.1063/5.0046061.

[43] Naoyuki Nakagawa, Harold Y. Hwang, and David A. Muller. "Why some interfaces cannot be sharp." In: *Nat. Mater.* 5.3 (2006), pp. 204–209. DOI: 10.1038/nmat1569.

[44] J. Junquera and P. Ghosez. "Critical thickness for ferroelectricity in perovskite ultrathin films." In: *Nature* 422 (2003), pp. 506–509. DOI: 10.1038/nature01501. URL: https://doi.org/10.1038/nature01501.

[45] Massimiliano Stengel. "Electrostatic stability of insulating surfaces: Theory and applications." In: *Phys. Rev. B* 84.20 (2011), p. 205432. DOI: 10.1103/physrevb.84.205432.

[46] M. Born and R. Oppenheimer. "Zur Quantentheorie der Molekeln." In: *Ann. Phys.* 389.20 (1927), pp. 457–484. DOI: 10.1002/andp.19273892002.

[47] P. Hohenberg and W. Kohn. "Inhomogeneous Electron Gas." In: *Phys. Rev.* 136.3B (1964), B864–B871. DOI: 10.1103/physrev.136.b864.

[48] W. Kohn and L. J. Sham. "Self-Consistent Equations including Exchange and Correlation Effects." In: *Phys Rev.* 140 (1965), A1133. DOI: 10.1103/PhysRev.140.A1133. URL: https://doi.org/10.1103/PhysRev.140.A1133.

[49] Reiner M. Dreizler and Eberhard K. U. Gross. *Density Functional Theory*. Springer Berlin Heidelberg, 1990. DOI: 10.1007/978-3-642-86105-5.

[50] J. P. Perdew and Alex Zunger. "Self-interaction correction to density-functional approximations for many-electron systems." In: *Phys. Rev. B* 23.10 (1981), pp. 5048–5079. DOI: 10.1103/physrevb.23.5048.

[51] D. M. Ceperley and B. J. Alder. "Ground State of the Electron Gas by a Stochastic Method." In: *Phys. Rev. Lett.* 45.7 (1980), pp. 566–569. DOI: 10.1103/physrevlett.45.566.

[52] J. P. Perdew, K. Burke, and M. Ernzerhof. "Generalized Gradient Approximation Made Simple." In: *Phys Rev. Lett.* 77 (1996), p. 3865. DOI: 10.1103/PhysRevLett.77.3865. URL: https://doi.org/10.1103/PhysRevLett.77.3865.

[53] John P. Perdew, Adrienn Ruzsinszky, Gábor I. Csonka, Oleg A. Vydrov, Gustavo E. Scuseria, Lucian A. Constantin, Xiaolan Zhou, and Kieron Burke. "Restoring the Density-Gradient Expansion for Exchange in Solids and Surfaces." In: *Phys. Rev. Lett.* 100.13 (2008), p. 136406. DOI: 10.1103/physrevlett.100.136406.

[54] Vladimir I. Anisimov, Jan Zaanen, and Ole K. Andersen. "Band theory and Mott insulators: HubbardUinstead of StonerI." In: *Phys. Rev. B* 44.3 (1991), pp. 943–954. DOI: 10.1103/physrevb.44.943.

[55] Julia A. Mundy, Colin A. Heikes, Bastien F. Grosso, Dan Ferenc Segedin, Zhe Wang, Berit H. Goodge, Quintin N. Meier, Christopher T. Nelson, Bhagwati Prasad, Lena F. Kourkoutis, William D. Ratcliff, Nicola A. Spaldin, Ramamoorthy Ramesh, and Darrell G. Schlom. "A high-energy density antiferroelectric made by interfacial electrostatic engineering." In: (Dec. 2018). arXiv: 1812.09615 [cond-mat.mtrl-sci].

[56] J. A. Mundy, B. F. Grosso, C. A Heikes, D. FerencSegedin, Z. Wang, Y.-T. Shao, C. Dai, B. H. Goodge, Q. N. Meier, C. T. Nelson, B. Prasad, F. Xue, D. A. Muller, L. F. Kourkoutis, L.-Q. Chen, W. D. Ratcliff, N. A. Spaldin, R. Ramesh, and D. G. Schlom. "Liberating a hidden antiferroelectric phase with interfacial electrostatic engineering." In: *private communication, manuscript in preparation* (2021).

[57] R. D. Shannon. "Revised effective ionic radii and systematic studies of interatomic distances in halides and chalcogenides." In: *Acta Crystallogr A* 32.5 (1976), pp. 751–767. DOI: 10.1107/s0567739476001551.

[58] O. Diéguez, O. E. González-Vázquez, J. C. Wojdel, and J. Íñiguez. "First-principles predictions of low-energy phases of multiferroic $BiFeO_3$." In: *Phys. Rev. B.* 83 (2011), p. 094105. DOI: 10.1103/PhysRevB.83.094105. URL: https://doi.org/10.1103/PhysRevB.83.094105.

[59] Gijsbert Rispens, Benedikt Ziegler, Zeila Zanolli, Jorge Íñiguez, Philippe Ghosez, and Patrycja Paruch. "Phase diagram ofBiFeO3/LaFeO3superlattices studied by x-ray diffraction experiments and first-principles calculations." In: *Phys. Rev. B* 90.10 (2014), p. 104106. DOI: 10.1103/physrevb.90.104106.

[60] Zeila Zanolli, Jacek C. Wojdeł, Jorge Íñiguez, and Philippe Ghosez. "Electric control of the magnetization in BiFeO3/LaFeO3superlattices." In: *Phys. Rev. B* 88.6 (2013), p. 060102. DOI: 10.1103/physrevb.88.060102.

[61] Benjamin Carcan, Houssny Bouyanfif, Mimoun El Marssi, Françoise Le Marrec, Loic Dupont, Carine Davoisne, Jérôme Wolfman, and Donna C. Arnold. "Phase Diagram of BiFeO3 /LaFeO3 Superlattices: Antiferroelectric-Like State Stability Arising from Strain Effects and Symmetry Mismatch at Heterointerfaces." In: *Adv. Mater. Interfaces* 4.11 (2017), p. 1601036. DOI: 10.1002/admi.201601036.

[62] O. E. González-Vázquez, Jacek C. Wojdeł, Oswaldo Diéguez, and Jorge Íñiguez. "First-principles investigation of the structural phases and enhanced response properties of the BiFeO3-LaFeO3multiferroic solid solution." In: *Phys. Rev. B* 85.6 (2012), p. 064119. DOI: 10.1103/physrevb.85.064119.

[63] Jung-Hoon Lee, Min-Ae Oak, Hyoung Joon Choi, Jong Yeog Son, and Hyun Myung Jang. "Rhombohedral–orthorhombic morphotropic phase boundary in BiFeO3-based multiferroics: first-principles prediction." In: *J. Mater. Chem.* 22.4 (2012), pp. 1667–1672. DOI: 10.1039/c1jm13582a.

[64] G. Kresse and J. Hafner. "Ab initiomolecular dynamics for liquid metals." In: *Phys. Rev. B* 47.1 (1993), pp. 558–561. DOI: 10.1103/physrevb.47.558.

[65] G. Kresse and J. Hafner. "Ab initiomolecular-dynamics simulation of the liquid-metal–amorphous-semiconductor transition in germanium." In: *Phys. Rev. B* 49.20 (1994), pp. 14251–14269. DOI: 10.1103/physrevb.49.14251.

[66] G. Kresse and J. Furthmüller. "Efficiency of ab-initio total energy calculations for metals and semiconductors using a plane-wave basis set." In: *Comput. Mater. Sci.* 6.1 (1996), pp. 15–50. DOI: 10.1016/0927-0256(96)00008-0.

[67] G. Kresse and J. Furthmüller. "Efficient iterative schemes forab initiototal-energy calculations using a plane-wave basis set." In: *Phys. Rev. B* 54.16 (1996), pp. 11169–11186. DOI: 10.1103/physrevb.54.11169.

[68] P. E. Blöchl. "Projector augmented-wave method." In: *Phys Rev. B* 50 (1994), p. 17953. DOI: 10.1103/PhysRevB.50.17953. URL: https://doi.org/10.1103/PhysRevB.50.17953.

[69] G. Kresse and D. Joubert. "From ultrasoft pseudopotentials to the projector augmented-wave method." In: *Phys. Rev. B* 59.3 (1999), pp. 1758–1775. DOI: 10.1103/physrevb.59.1758.

[70] Hendrik J. Monkhorst and James D. Pack. "Special points for Brillouin-zone integrations." In: *Phys. Rev. B* 13.12 (1976), pp. 5188–5192. DOI: 10.1103/physrevb.13.5188.

[71] S. L. Dudarev, G. A. Botton, S. Y. Savrasov, C. J. Humphreys, and A. P. Sutton. "Electron-energy-loss spectra and the structural stability of nickel oxide: An LSDA+U study." In: *Phys Rev. B* 57 (1998), p. 1505. DOI: 10.1103/PhysRevB.57.1505. URL: https://doi.org/10.1103/PhysRevB.57.1505.

[72] A. Togo and I. Tanaka. "First principles phonon calculations in materials science." In: *Scr. Mater.* 108 (2015), pp. 1–5. DOI: 10.1016/j.scriptamat.2015.07.021. URL: http://dx.doi.org/10.1016/j.scriptamat.2015.07.021.

[73] T. Stokes, D. M. Hatch, and B. J. Campbell. "ISODISTORT, ISOTROPY Software Suite." In: *iso.byu.edu* (). URL: https://iso.byu.edu/.

[74] B. J. Campbell, H. T. Stokes, D. E. Tanner, and D. M. Hatch. "ISODISPLACE: a web-based tool for exploring structural distortions." In: *J. Appl. Cryst.* 39 (2006), pp. 607–614. DOI: 10.1107/S0021889806014075. URL: https://doi.org/10.1107/S0021889806014075.

[75] D. D. Khalyavin, A. N. Salak, N. M. Olekhnovich, A. V. Pushkarev, Yu. V. Radyush, P. Manuel, I. P. Raevski, M. L. Zheludkevich, and M. G. S. Ferreira. "Polar and antipolar polymorphs of metastable perovskiteBiFeo.5Sco.5O3." In: *Phys. Rev. B* 89.17 (2014), p. 174414. DOI: 10.1103/physrevb.89.174414.

[76] Boža Veličkov, Volker Kahlenberg, Rainer Bertram, and Reinhard Uecker. "Redetermination of terbium scandate, revealing a defect-type perovskite derivative." In: *Acta Crystallogr., Sect. E: Struct. Rep. Online* 64.11 (2008), pp. i79–i79. DOI: 10.1107/s1600536808033394.

[77] Philippe Ghosez and Javier Junquera. "First-Principles Modeling of Ferroelectric Oxide Nanostructures." In: *arXiv:0605.299* (May 2006). arXiv: cond-mat/0605299 [cond-mat.mtrl-sci].

[78] Jun Lu, M Schmidt, P Lunkenheimer, A Pimenov, A A Mukhin, V D Travkin, and A Loidl. "Magnetic susceptibility, phonons and dielectric constant of single crystalline BiFeO3." In: *J. Phys.: Conf. Ser.* 200.1 (2010), p. 012106. DOI: 10.1088/1742-6596/200/1/012106.

[79] Zhen Fan, John Wang, Michael B. Sullivan, Alfred Huan, David J. Singh, and Khuong P. Ong. "Structural Instability of Epitaxial (001) BiFeO3 Thin Films under Tensile Strain." In: *Sci. Rep.* 4.1 (2014). DOI: 10.1038/srep04631.

[80] C. Kittel. "Theory of Antiferroelectric Crystals." In: *Phys. Rev.* 82.5 (1951), pp. 729–732. DOI: 10.1103/physrev.82.729.

[81] E. Sawaguchi G. Shirane and Y. Takagi. "Dielectric Properties of Lead Zirconate." In: *Phys. Rev.* 84 (1951), p. 476. DOI: 10.1103/PhysRev.84.476. URL: https://doi.org/10.1103/PhysRev.84.476.

[82] E. Sawaguchi, H. Maniwa, and S. Hoshino. "Antiferroelectric Structure of Lead Zirconate." In: *Phys. Rev.* 83 (1951), p. 1078. DOI: 10.1103/PhysRev.83.1078. URL: https://doi.org/10.1103/PhysRev.83.1078.

[83] Karin M. Rabe. "Antiferroelectricity in Oxides: A Reexamination." In: *Functional Metal Oxides*. Wiley-VCH Verlag GmbH & Co. KGaA, 2013, pp. 221–244. DOI: 10.1002/9783527654864.ch7.

[84] I. Burn and D. M. Smyth. "Energy storage in ceramic dielectrics." In: *J Mater Sci* 7.3 (1972), pp. 339–343. DOI: 10.1007/bf00555636.

[85] Gregory Mills, Hannes Jónsson, and Gregory K. Schenter. "Reversible work transition state theory: application to dissociative adsorption of hydrogen." In: *Surf. Sci.* 324.2-3 (1995), pp. 305–337. DOI: 10.1016/0039-6028(94)00731-4.

[86] Graeme Henkelman, Blas P. Uberuaga, and Hannes Jónsson. "A climbing image nudged elastic band method for finding saddle points and minimum energy paths." In: *J. Chem. Phys.* 113.22 (2000), pp. 9901–9904. DOI: 10.1063/1.1329672.

[87] Graeme Henkelman and Hannes Jónsson. "Improved tangent estimate in the nudged elastic band method for finding minimum energy paths and saddle points." In: *J. Chem. Phys.* 113.22 (2000), pp. 9978–9985. DOI: 10.1063/1.1323224.

[88] Bastien F. Grosso and Nicola A. Spaldin. "Prediction of low-energy phases of BiFeO3 with large unit cells and complex tilts beyond Glazer notation." In: *Phys. Rev. Materials* 5.5 (2021), p. 054403. DOI: 10.1103/physrevmaterials.5.054403.

[89] Claude Ederer and Nicola A. Spaldin. "Effect of Epitaxial Strain on the Spontaneous Polarization of Thin Film Ferroelectrics." In: *Phys. Rev. Lett.* 95.25 (2005), p. 257601. DOI: 10.1103/physrevlett.95.257601.

[90] H. Béa, B. Dupé, S. Fusil, R. Mattana, B. Warot-Fonrose, F. Wilhelm, A. Rogalev, S. Petit, V. Cros, A. Anane, F. Petroff, K.Bouzehouane, G. Geneste, B. Dkhil, S. Lisenkov, I. Ponomareva, L. Bellaiche, M. Bibes, and A. Barthélémy. "Evidence for Room-Temperature Multiferroicity in a Compound with a Giant Axial Ratio." In: *Phys. Rev. Lett.* 102 (2009), p. 217603. DOI: 10.1103/PhysRevLett.102.217603. URL: https://doi.org/10.1103/PhysRevLett.102.217603.

[91] H. M. Christen, J. H. Nam, H. S. Kim, A. J. Hatt, and N. A. Spaldin. "Stress-induced R-M_A-M_C-T symmetry changes in $BiFeO_3$ films." In: *Phys. Rev. B* 83 (2011), p. 144107. DOI: 10.1103/PhysRevB.83.144107. URL: https://doi.org/10.1103/PhysRevB.83.144107.

[92] B. Dupé, S. Prosandeev, G. Geneste, B. Dkhil, and L. Bellaiche. "BiFeO3Films under Tensile Epitaxial Strain from First Principles." In: *Phys. Rev. Lett.* 106.23 (2011), p. 237601. DOI: 10.1103/physrevlett.106.237601.

[93] Y. Yang, W. Ren, M. Stengel, X. H. Yan, and L. Bellaiche. "Revisiting Properties of Ferroelectric and Multiferroic Thin Films under Tensile Strain from First Principles." In: *Phys. Rev. Lett.* 109 (2012), p. 057602. DOI: 10.1103/PhysRevLett.109.057602. URL: https://doi.org/10.1103/PhysRevLett.109.057602.

[94] J. C. Yang, Q. He, S. J. Suresha, C. Y. Kuo, C. Y. Peng, R. C. Haislmaier, M. A. Motyka, G. Sheng, C. Adamo, H. J. Lin, Z. Hu, L. Chang, L. H. Tjeng, E. Arenholz, N. J. Podraza, M. Bernhagen, R. Uecker, D. G. Schlom, V. Gopalan, L. Q. Chen, C. T. Chen, R. Ramesh, and Y. H. Chu. "Orthorhombic $BiFeO_3$." In: *Phys. Rev. Lett.* 109 (2012), p. 247606. DOI: 10.1103/PhysRevLett.109.247606. URL: https://doi.org/10.1103/PhysRevLett.109.247606.

[95] Johanna Nordlander, Aline Maillard, Manfred Fiebig, and Morgan Trassin. "Emergence of ferroelectricity at the morphotropic phase boundary of ultrathin $BiFeO_3$." In: (May 2020). arXiv: 2005.09685 [cond-mat.mtrl-sci].

[96] Gabriele De Luca, Nives Strkalj, Sebastian Manz, Corinne Bouillet, Manfred Fiebig, and Morgan Trassin. "Nanoscale design of polarization in ultrathin ferroelectric heterostructures." In: *Nat Commun* 8.1 (2017). DOI: 10.1038/s41467-017-01620-2.

[97] Ipek Efe, Nicola A. Spaldin, and Chiara Gattinoni. "On the happiness of ferroelectric surfaces and its role in water dissociation: The example of bismuth ferrite." In: *J. Chem. Phys.* 154.2 (2021), p. 024702. DOI: 10.1063/5.0033897.

[98] N. Strkalj, G. De Luca, M. Campanini, S. Pal, J. Schaab, C. Gattinoni, N. A. Spaldin, M. D. Rossell, M. Fiebig, and M. Trassin. "Depolarizing-Field Effects in Epitaxial Capacitor Heterostructures." In: *Phys. Rev. Lett.* 123.14 (2019), p. 147601. DOI: 10.1103/physrevlett.123.147601.

[99] X. Y. Li, Q. Yang, J. X. Cao, L. Z. Sun, Q. X. Peng, Y. C. Zhou, and R. X. Zhang. "Domain Wall Motion in Perovskite Ferroelectrics Studied by the Nudged Elastic Band Method." In: *The Journal of Physical Chemistry C* 122.5 (2018), pp. 3091–3100. DOI: 10.1021/acs.jpcc.7b11330.

[100] R. Palai, R. S. Katiyar, H. Schmid, P. Tissot, S. J. Clark, J. Robertson, S. A. T. Redfern, G. Catalan, and J. F. Scott. "βphase andγ-βmetal-insulator transition in multiferroicBiFeO3." In: *Phys. Rev. B* 77.1 (2008), p. 014110. DOI: 10.1103/physrevb.77.014110.

[101] N. A. Spaldin and R. Ramesh. "Advances in magnetoelectric multiferroics." In: *Nat. Mater.* 18.3 (2019), pp. 203–212. DOI: 10.1038/s41563-018-0275-2.

[102] Tianzhe Chen, Shuzhen Yang, Christopher T. Nelson, Bastien F. Grosso, Guopeng Wang, Vishal Thakare, Martin Dahlqvist, Meng Wang, Qing He, Naoki Ogawa, Jingwen Guo, Yujia Wang, Zhuolo Li, Nianpeng Lu, Haobo Li, Ke Deng, Mingzhe Yan, Shanglin Hsu, Shyam Dwaraknath, James D. Clarkson, Julia A. Mundy, Alan Farhan, Alpha T. N'Diaye, Andreas Scholl, Elke Arenholz, Masao Nakamura, Masashi Kawasaki, Shuyun Zhou, Cewen Nan, Yoshi Tokura, Nicola A. Spaldin, Ramamoorthy Ramesh, and Pu Yu. "A new room temperature multiferroic bismuth hexaferrite." In: *private communication, manuscript in preparation* (2021).

[103] R. Dronskowski. "The Little Maghemite Story: A Classic Functional Material." In: *Adv. Funct. Mater.* 11.1 (2001), pp. 27–29. DOI: 10.1002/1616-3028(200102)11:1<27::aid-adfm27>3.0.co;2-x.

[104] W. D. Townes, J. H. Fang, and A. J. Perrotta. "The crystal structure and refinement of ferrimagnetic barium ferrite, BaFe12O19." In: *Zeitschrift für Kristallographie - Crystalline Materials* 125.1-6 (1967). DOI: 10.1524/zkri.1967.125.16.437.

[105] Chih-Chung Chang and Chih-Jen Lin. "LIBSVM." In: *ACM Transactions on Intelligent Systems and Technology* 2.3 (2011), pp. 1–27. DOI: 10.1145/1961189.1961199.

[106] Harris Drucker, Chris JC Burges, Linda Kaufman, Alex Smola, Vladimir Vapnik, et al. "Support vector regression machines." In: *Advances in neural information processing systems* 9 (1997), pp. 155–161.

[107] Fabian Pedregosa, Gaël Varoquaux, Alexandre Gramfort, Vincent Michel, Bertrand Thirion, Olivier Grisel, Mathieu Blondel, Peter Prettenhofer, Ron Weiss, Vincent Dubourg, Jake Vanderplas, Alexandre Passos, David Cournapeau, Matthieu Brucher, Matthieu Perrot, and Édouard Duchesnay. "Scikit-learn: Machine Learning in Python." In: *Journal of Machine Learning Research* 12.85 (2011), pp. 2825–2830. URL: http://jmlr.org/papers/v12/pedregosa11a.html.

[108] "Private communciations with Anton O. Oliynk, unpublished work."

[109] Igor Levin. *NIST Inorganic Crystal Structure Database (ICSD)*. en. 2020. DOI: 10.18434/M32147.

[110] S. Ping Ong, W. Davidson Richards, A. Jain, G. Hautier, M. Kocher, S. Cholia, D. Gunter, V. L. Chevrier, K. A. Persson, and G. Ceder. "Python Materials Genomics (pymatgen): A robust, open-source python library for materials analysis." In: *Comput. Mater. Sci.* 68 (2013), pp. 314–319. DOI: 10.1016/j.commatsci.2012.10.028. URL: https://doi.org/10.1016/j.commatsci.2012.10.028.